Project information	
Project full title	EuroSea: Improving and Integrating European Ocean Observing and Forecasting Systems for Sustainable use of the Oceans
Project acronym	EuroSea
Grant agreement number	862626
Project start date and duration	1 November 2019, 50 months
Project website	https://www.eurosea.eu

Deliverable information	
Deliverable number	D2.3
Deliverable title	**Analysis of the OSSEs with multi-platform in situ data and impact on fine-scale structures**
Description	This report includes recommendations for the design of in situ experiments aimed to reconstruct fine-scale ocean currents (~20 km), such as those that will be conducted to validate SWOT satellite observations.
Work Package number	2
Work Package title	Ocean Observing System Design
Lead beneficiary	CSIC
Lead authors	Bàrbara Barceló-Llull (CSIC)
Contributors	Ananda Pascual (CSIC), Aurélie Albert (Ocean-Next), Maxime Beauchamp (IMT-Atlantique), Ronan Fablet (IMT-Atlantique), Stéphanie Guinehut (CLS), Jaime Hernández-Lasheras (SOCIB), Mario Herrero González (IMT-Atlantique), Solène Jousset (CLS), Stephanie Leroux (Ocean-Next), Baptiste Mourre (SOCIB) and Sandrine Mulet (CLS)
Due date	31.07.2022
Submission date	30.07.2022
Comments	

This project has received funding from the European Union's Horizon 2020 research and innovation programme under grant agreement No. 862626.

https://doi.org/10.3289/eurosea_d2.3

Table of contents

Executive summary

Deliverable 2.3 describes the study developed in Task 2.3 of the EuroSea project. It includes recommendations for the design of in situ experiments aimed to reconstruct fine-scale ocean currents (~20 km), such as those that will be conducted to validate SWOT satellite observations. An advanced version of the spatial optimal interpolation used in field experiments, which also includes the temporal variability of the observations, has been applied to evaluate different sampling strategies. In addition, we have tested two reconstruction methods based on machine-learning and model data assimilation. Finally, we have evaluated the recently developed MIOST technique to map nadir altimetry using current observations derived from drifters.

1. Introduction to EuroSea

Although the Ocean is a fundamental part of the global system providing a wealth of resources, there are fundamental gaps in ocean observing and forecasting systems, limiting our capacity in Europe to sustainably manage the ocean and its resources. Ocean observing is “big science” and cannot be solved by individual nations; it is necessary to ensure high-level integration for coordinated observations of the ocean that can be sustained in the long term. For Europe, EuroSea will point the way for the current and future cooperation between science and industry, politics and the public with the common goal of a sustainable blue economy and the responsible handling of the sensitive marine ecosystems. The project will make a significant contribution to not only generating, processing and linking information about our oceans, but also to make long-term and extensive use of this and the resulting knowledge in a wide variety of areas. As a link between sectors and disciplines, EuroSea faces a very big challenge.

2. Introduction to WP2

The overall objective of WP2 is to apply the systems design processes of the Framework for Ocean Observing (FOO) on the EuroSea observing system in support of connected and integrated European Ocean Observing systems for the broader Atlantic Ocean and Mediterranean Sea. It builds on the H2020 AtlantOS achievements and take on its legacy to further develop them within the Galway and Belém agreements objectives. Specific objectives are:

- To define the high-level requirements of EuroSea based on the societal benefits, providing a direct link to societal challenges related to the larger Atlantic and Mediterranean basins and the European Blue Growth strategy. These requirements will be translated into strategic recommendations about sustained monitoring of EOVs and linked with LR7 and LR8 societal relevant indicators.
- To identify the requirements in existing observing networks in support of specific demonstrators (WP5,6,7).
- To deliver guidance to improve existing elements and/or implement new ocean observing components to EuroSea using various techniques, including OSSEs and data assimilation to optimally merge in-situ and satellite observations with models to provide accurate estimates for indicators.

3. Introduction to T2.3

Space borne and in situ observations provide essential and complementary information on fine-scale ocean structures. Task 2.3 has the objective to improve the design of multi-platform experiments aimed to validate the Surface Water and Ocean Topography (SWOT) satellite observations with the goal to optimize the utility of these observing platforms. Considered the next big breakthrough in Earth observation, the SWOT satellite mission, with a resolution one order of magnitude higher than present altimeters, will be launched in 2022 by the National Aeronautics and Space Administration (NASA) and the Centre National d'Études Spatiales (CNES) with contributions of the UK and Canadian Space Agencies (Morrow et al., 2019). The SWOT mission will provide sea surface height (SSH) measurements in two dimensions along a wide-swath altimeter with an expected effective resolution in wavelength of 15-45 km (Fu and Ferrari, 2008; Fu and Ubelmann, 2014, Wang et al., 2019). After launch, the SWOT satellite will follow a fast-sampling orbit to provide observations of SSH on a daily basis in specific areas of the world ocean for instrumental calibration/validation. The SWOT fast-sampling phase is considered an ideal opportunity to coordinate in situ experiments with the objective to study fine-scale dynamics and their role in the Earth system (d'Ovidio et al., 2019).

To anticipate the daily high-resolution two-dimensional (2D) SSH fields that SWOT will provide, the PRE-SWOT multi-platform experiment was conducted in the southern region of the Balearic Islands (western Mediterranean Sea) in May 2018 (Barceló-Llull et al., 2018, Barceló-Llull et al., 2021). In situ observations from gliders, drifters, a Conductivity Temperature Depth probe (CTD), and a hull-mounted Acoustic Doppler Current Profiler (ADCP), were collected to evaluate the horizontal and vertical velocities associated with the scales that SWOT will resolve (defined as fine scales). This experiment highlighted the need to increase the spatial resolution of altimetric observations comparing present altimetric fields with in situ observations. It also revealed the need to study the impact of including some modification in the design of future experiments aimed to validate SWOT, like the depth of the CTD measurements and the impact of changing rosette CTD casts for an underway CTD. In addition, even if the southern region of the Balearic Islands will be sampled by a SWOT crossover during the fast-sampling phase, this study demonstrates that (i) this region has low variability and is characterized by low hydrographic gradients, and (ii) there are limitations to stay in Spanish or international waters. Because of this, the authors suggest that the next cruise experiments to validate SWOT should be held in the north-western region of the Balearic Islands, a region with more dynamic activity and that will be crossed by a swath of SWOT during the fast-sampling phase.

The objective of Task 2.3 is to optimize the design of multi-platform experiments aimed to validate SWOT observations. Observing System Simulation Experiments (OSSEs) have been conducted to evaluate different configurations of the in situ observing system, including rosette and underway CTD, gliders, conventional satellite nadir altimetry and velocities from drifters. Simulations from high-resolution models have been used to simulate the observations and the "ocean truth" to represent fine-scale sea level and surface ocean velocities. Several methods of reconstructions have been tested. The first method is an advanced version of the classic optimal interpolation used in field experiments, which considers the spatial and the temporal variability of the observations. This technique has been applied to reconstruct different configurations with the objective to evaluate the best sampling strategy to validate SWOT. Secondly, new algorithms of in situ data reconstruction using machine-learning techniques are explored, implemented and benchmarked to be compared with the "ocean truth". Then, the 2-km resolution Western Mediterranean Operational system (WMOP) model and data assimilation (Juza et al., 2016; Mourre et al. 2018) has been used to reconstruct multivariate three-dimensional (3D) fields from these virtual observations. Finally, the Multiscale Inversion for Ocean Surface Topography (MIOST) variational tool has been tested to reconstruct sea surface height and

ocean currents at the ocean surface. The capacity of the reconstructed fields to represent the sea level and surface current variability of the nature run models at the scales and with the expected accuracy of the future SWOT satellite mission are evaluated considering different configurations of in situ observations.

The analysis focuses on two regions of interest for the Climate Demonstrator in WP7: (i) the western Mediterranean Sea and (ii) the Subpolar North West Atlantic. In the western Mediterranean Sea, the target area is located within a swath of SWOT, while in the North West Atlantic the region of study includes a crossover of SWOT during the fast-sampling phase. These OSSEs contribute to the design of the in situ observing systems to support the future calibration and validation of high-resolution SWOT satellite measurements.

3.1. Scientific goals and subtasks

Objective 1: Optimize the design of a multi-platform in-situ experiment to validate SWOT (subtask 2.3.1)

Evaluate the impact of different sampling strategies in the reconstruction of fine-scale features comparing the simulated and reconstructed observations with the "ocean truth" from the model. For this objective, the reconstruction method is an advanced version of the classic optimal interpolation (OI) that considers the spatio-temporal variability of the observations (Escudier et al., 2013). This analysis has been done in both regions of study and using all models to provide robustness to the results.

Objective 2: Compare different methods of reconstruction to validate SWOT (subtask 2.3.2)

Test different methods of reconstruction (optimal interpolation, machine-learning techniques, and WMOP assimilation) to reconstruct the simulated observations in the reference configuration (determined as a good sampling strategy in subtask 2.3.1). Compare the reconstructed fields with the "ocean truth" through the root-mean-square-error (RMSE). This analysis has been done in the Mediterranean and using the eNATL60 simulated observations.

Objective 3: Explore the capability of the existing observing system networks to validate SWOT (subtask 2.3.3)

We aim to use surface drifters in addition to nadir altimetry to improve the accuracy and resolution of SLA maps, usually constructed only from nadir altimetry. We (i) evaluate the performances of the reconstruction and (ii) analyse if this merging can be useful for the validation of SWOT. In this experiment we also evaluate the impact of tripling the number of drifters and quantify the impact in terms of resolution. This study is done in the Mediterranean and for the observations simulated from eNATL60.

4. Regions of study

The analysis focuses on two regions of interest for the Climate Demonstrator in WP7: the subpolar northwest Atlantic and the western Mediterranean Sea. In the subpolar northwest Atlantic, the region of study includes a crossover of SWOT during the fast-sampling phase (Figure 1). In the western Mediterranean Sea, the domain is located within a swath of SWOT at the northern part of the Balearic Sea (Figure 1), a region with high dynamic activity and already studied by several authors using in situ and remote sensing observations (e.g. Pascual et al., 2002; Ruiz et al., 2009; Bouffard et al., 2010; Mason and Pascual, 2013). Within each region of study, a smaller sub-region is defined to simulate the in situ observations in different configurations.

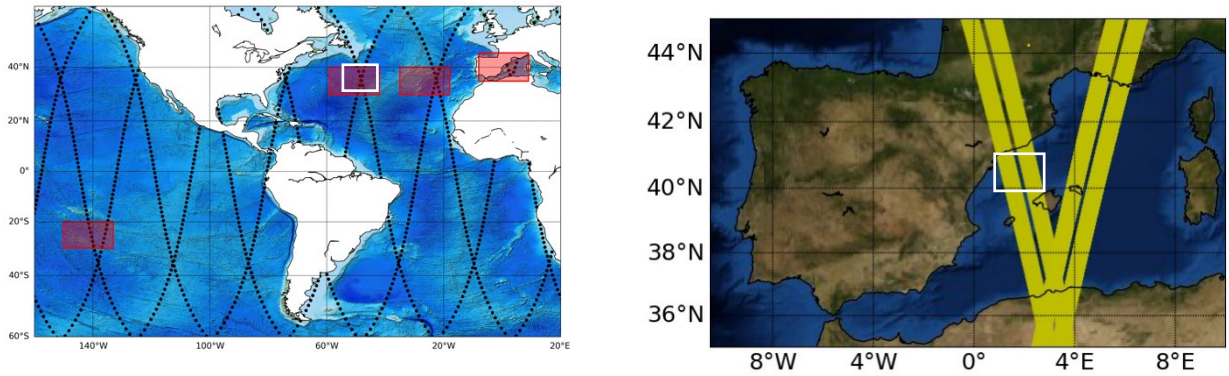

Figure 1: Regions of study: a SWOT crossover in the subpolar northwest Atlantic and a swath of SWOT at the northern part of the Balearic Sea in the western Mediterranean. Figures courtesy of Laura Gómez-Navarro.

The coordinates of these regions are:

- Atlantic: longitude [55ºW, 40ºW] and latitude [30ºN, 40ºN]
  - Sub-region: longitude [49.5ºW, 47.5ºW] and latitude [34.5ºN, 36.5ºN]
- Mediterranean: longitude [5.7ºW, 9.6ºE] and latitude [35.1ºN, 44.4ºN]
  - Sub-region: longitude [1ºE, 3ºE] and latitude [39.5ºN, 41.5ºN]

5. Nature run models

In each region of study different high-resolution models are used as "nature run models" depending on the objective. These models are assumed to represent the "ocean truth" and are used to simulate the observations in different configurations. Model outputs are extracted in a common temporal period between 1-july-2009 and 30-june-2010. However, the simulated observing systems are representative of a recent period (see next section). In the big regions described in the previous section the extracted model outputs are at the ocean surface, while in the sub-regions we extracted three-dimensional (3D) fields from 0 to 1000 m.

The model outputs used for each region and their characteristics are:

- Atlantic: CMEMS global reanalysis and eNATL60
- Mediterranean: CMEMS Mediterranean reanalysis, eNATL60 and WMOP

5.1. Two CMEMS reanalyses

- The CMEMS (Copernicus Marine Environment Monitoring Service) global ocean physics reanalysis model (GLOBAL_MULTIYEAR_PHY_001_030) used in the Atlantic experiments has a spatial resolution of 1/12° and 50 vertical levels. The model component is the Nucleus for European Modelling of the Ocean (NEMO) platform driven at the surface by ECMWF ERA-Interim reanalysis. Along-track Sea Level Anomaly (SLA), satellite Sea Surface Temperature (SST), Sea Ice Concentration and in situ temperature and salinity vertical profiles are assimilated. This product includes daily and monthly mean files of temperature, salinity, currents, sea level, mixed layer depth and ice parameters from the surface to 5500 m, and covers the period between 1993 and 2019. The model outputs are available at https://doi.org/10.48670/moi-00021.

- The CMEMS Mediterranean Sea physics reanalysis model (Escudier et al., 2020) used in the Mediterranean experiments has a spatial resolution of 1/24º and 141 vertical levels. This product is generated by a numerical system consisting of a hydrodynamic model supplied by NEMO and a variational data assimilation scheme (OceanVAR). It assimilates in situ temperature and salinity vertical profiles, satellite along-track SLA and SST. This product includes hourly, daily and monthly mean fields of temperature, salinity, currents, sea level and mixed layer depth from the surface to 5500 m, and covers the period from 1987 to present. For our experiments we use the daily mean fields. The model outputs are available at https://doi.org/10.25423/CMCC/MEDSEA_MULTIYEAR_PHY_006_004_E3R1.

5.2. eNATL60

eNATL60 corresponds to a pair of twin numerical ocean simulations performed in 2019 with the NEMO ocean model over the North Atlantic at 1/60° grid resolution by Ocean-Next and the MEOM group[1] at IGE[2] on MareNostrum supercomputer at BSC[3] within a PRACE project[4].

The model configuration has been defined in order to model as accurately as possible surface signature of oceanic motions of scales down to 15 km in line with the expected effective resolution of SWOT ocean data. The choice of the model horizontal and vertical resolution derives from this objective. A particular emphasis has also been put on the representation of high frequency motions associated with internal tides as several studies suggest that these signals will be prominent in SWOT data at scale <100km.

The eNATL60 simulations span the North Atlantic from about 6°N up to the polar circle and fully include the Gulf of Mexico, the Mediterranean Sea, and the Black Sea (Figure 2):

- Horizontal grid: 1/60°, 8354×4729 points
- 0.8 km < Δx < 1.6 km
- Vertical grid: 300 levels
- Lateral Boundary Conditions for U,V, T, S & sea-ice: daily, GLORYS12 v1 (1/12°, Mercator Ocean)
- Lateral Boundary Conditions for tides (SSH, u, v): FES2014 (F. Lyard)
- Atmospheric forcing: 3-hourly, ERA-interim (ECMWF)

This model configuration has been implemented and run in two different “free” simulations (no data assimilation). The reference experiment eNATL60-BLB002 has been run without explicit tidal forcing from 1-july-2009 to 6-july-2010; the sensitivity experiment eNATL60-BLBT02 was run with explicit tidal forcing from 1-july-2009 to 29-october-2010. In this study we use the simulation without tidal forcing. Hourly outputs with a horizontal resolution of 1/60º are used to simulate observations. Degraded daily outputs with 1/20º of horizontal resolutions are used in subtask 2.3.3 to compare the reconstructed solutions and evaluate them. Using a degraded native run allows to work with lighter files and decreases the computation time. In addition, the spatio-temporal resolution of the degraded model outputs is closer, and thus more consistent, with the MIOST reconstructions (daily maps with a horizontal spacing of 1/20°).

[1] http://meom-group.github.io
[2] http://www.ige-grenoble.fr
[3] https://www.bsc.es
[4] http://prace-ri.eu/

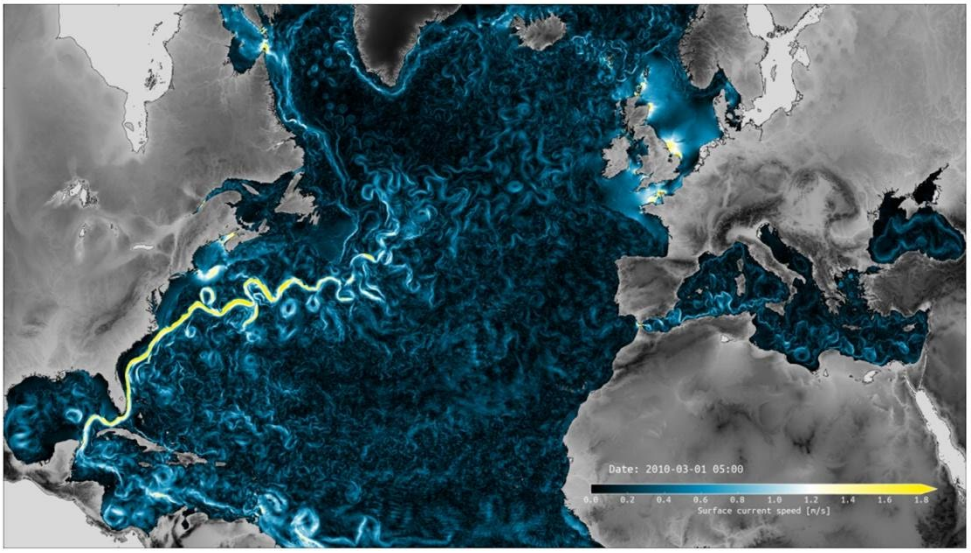

Figure 2: Horizontal extent of the eNATL60 domain illustrated by a snapshot of surface current speed.

5.3. WMOP

The WMOP (Western Mediterranean OPerational system) model (Juza et al., 2016; Mourre et al., 2018) is a regional configuration of the ROMS model in the western Mediterranean Sea, covering from Gibraltar strait to Corsica and Sardinia (Figure 3). It is a downscaling of the CMEMS-MED-MFC (Simoncelli et al., 2014) with a 2 km horizontal resolution and 32 vertical sigma levels. The model is forced with high-resolution atmospheric fields from AEMET (Spanish meteorological agency), with 1-hour and 5-km resolution for the operational model and does not include tides. The operational system assimilates SST, along-track SLA, Argo temperature and salinity profiles, mooring data and surface current observations from HF-radar using a sequential ensemble optimal interpolation (EnOI) method every 3 days (method described in Hernandez-Lasheras and Mourre, 2018). It runs every day, producing a 3-day forecast of ocean temperature, salinity, sea level and currents, which is validated and publicly distributed at www.socib.es and http://thredds.socib.es/. The model represents the ocean variability from the (sub-)meso- to the basin- scale.

The Balearic Islands Coastal Observing and Forecasting System (SOCIB) has also run a series of hindcast simulations spanning from 2009 to 2019, using different parent models, initial and boundary conditions and momentum and diffusion parameters. The hindcast configuration used in this study has been widely validated in different publications (Mourre et al. 2018, Aguiar et al. 2019).

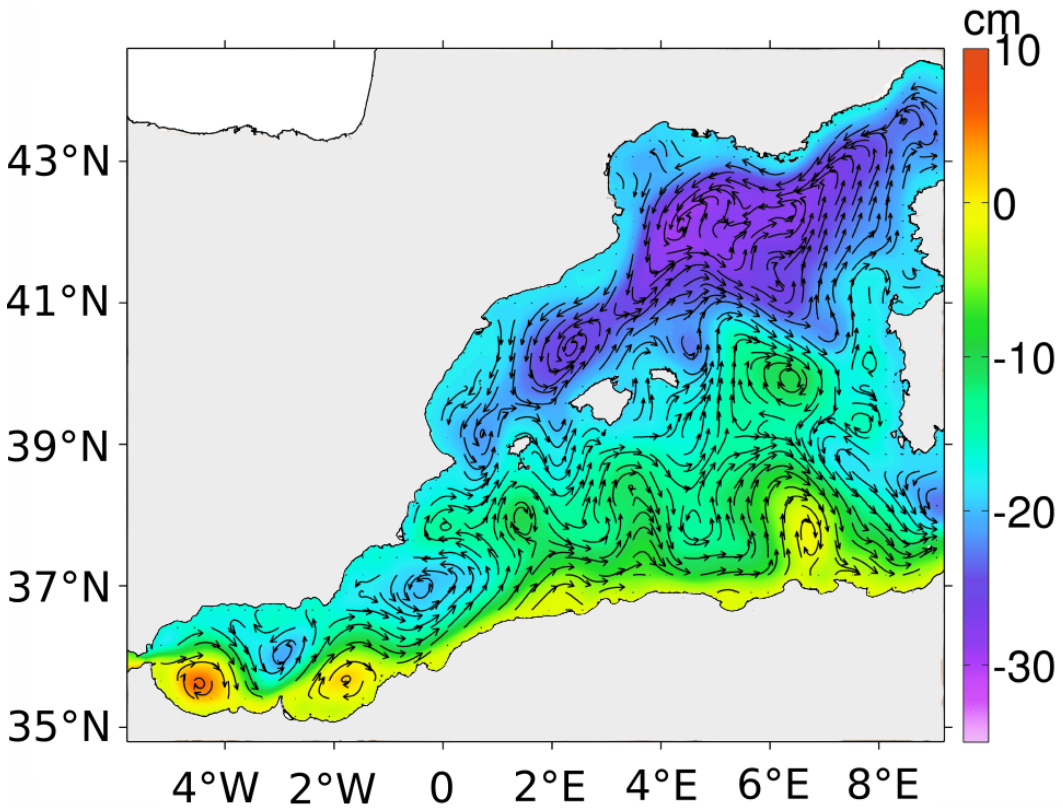

Figure 3: Sea surface height annual mean for 2014 and corresponding surface geostrophic currents from WMOP model.

6. Simulation of the observations

6.1. Overview

Remote sensing and in situ observations have been simulated from the models described in the previous section (also called "pseudo-observations" in this report). The observing platforms and the corresponding variables that have been simulated are presented in Table 1, together with the model(s) used for the simulation, the region in which they have been simulated and the partner that simulated each observation.

Due to the big size of the high-resolution model outputs, two different datasets were shared between partners for each region and model:

- The 3D dataset includes temperature, salinity and horizontal velocity fields from the surface to 1000 m depth in the sub-regions described in Section 4. These fields were used to simulate vertical profiles of temperature and salinity.
- The 2D dataset includes SSH and horizontal currents in the whole domain of the regions of study. These fields were used to simulate SWOT, nadir altimetry and drifter trajectories in the Mediterranean.

Table 1. Observing platforms and the corresponding variables simulated. Models used to simulate each observation, region of simulation and partner responsible for that simulation.

Platform	Variables	Models	Regions	Partner
Rosette CTD	vertical profiles of temperature and salinity	CMEMS eNATL60 WMOP	Mediterranean Atlantic	CSIC
Underway CTD (uCTD)	vertical profiles of temperature and salinity	CMEMS eNATL60 WMOP	Mediterranean Atlantic	CSIC
Glider	vertical profiles of temperature and salinity	CMEMS eNATL60 WMOP	Mediterranean Atlantic	CSIC
ADCP	vertical profiles of total (geostrophic and ageostrophic) horizontal velocity	CMEMS WMOP	Mediterranean Atlantic	CSIC
Drifters	horizontal velocities along the trajectories at 0 and 15 m depth	eNATL60	Mediterranean Atlantic	Ocean Next
Nadir altimetry	along-track SSH and associated errors	eNATL60	Mediterranean	Ocean Next
SWOT	SSH and associated errors	eNATL60	Mediterranean Atlantic	Ocean Next
Gridded L4 SST satellite product	Sea surface temperature and associated errors	eNATL60	Mediterranean	SOCIB
Argo	vertical profiles of temperature and salinity and associated errors	eNATL60	Mediterranean	SOCIB

6.2. CTD

Vertical profiles of temperature and salinity were simulated following the same procedure for the three platforms equipped with CTDs (rosette CTD, uCTD and gliders). For each CTD profile, defined by its spatial coordinates and time, we extracted the corresponding data from the model outputs using a 4D linear interpolation in time, depth, latitude and longitude. The function used to do this 4D interpolation is “RegularGridInterpolator” from the module “scipy.interpolate” in Python. The variables extracted are potential temperature and practical salinity.

Previous step for eNATL60: The original eNATL60 outputs are in a rotated grid. For this model a previous step is needed to linearly interpolate the original fields onto a regular 2D grid for each time step and depth (the original spatial resolution of 1/60º is maintained). The Python function used to do this interpolation is "griddata" from the module “scipy.interpolate”.

In the context of subtask 2.3.1 we have not included instrumental or representative errors to the pseudo-observations of CTD to ensure that the comparisons done between different configurations are not affected by simulated errors and they are only due to the configuration strategy and sampling duration.

For the reconstruction with WMOP data assimilation (subtask 2.3.2) we add instrumental errors to the CTD pseudo-observations of temperature and salinity. These errors are uncorrelated horizontally and vertically and they are generated as a random value following a Gaussian distribution with a standard deviation defined by the error of the instrument (0.01ºC for temperature, 0.01 for salinity; Gasparin et al., 2019). Note that each individual observation has a different (uncorrelated) error.

6.3. ADCP

Vertical profiles of total (geostrophic and ageostrophic) horizontal velocity were simulated following the same procedure as for CTD observations. For each ADCP profile, defined by its spatial coordinates and time, we extracted the corresponding data from the model outputs using a 4D linear interpolation in time, depth, latitude and longitude. The function used to do this 4D interpolation is "RegularGridInterpolator" from the module "scipy.interpolate" in Python. The variables extracted are zonal and meridional velocities. The comparison of ADCP velocity with CTD-derived geostrophic velocity will be conducted as future work. To complete the objective of subtask 2.3.1, we have compared the CTD-derived geostrophic velocity with the ocean truth.

6.4. Drifters

To simulate drifter observations, we have computed Lagrangian trajectories from eNATL60 hourly horizontal currents at 15 m depth through Ocean Parcels[5]. Two different sets of drifter trajectories were simulated depending on the objective.

Set 1: To evaluate the geostrophic velocity calculated from CTD pseudo-observations, we simulated the release of 49 drifters evenly spaced within the small sub-regions described in Section 4 in the Mediterranean (Figure 4) and Atlantic. The Lagrangian trajectories were computed and saved every 15 min during 6 days starting on the 1st of September 2009. The comparison of drifter velocity with CTD-derived geostrophic velocity will be conducted as future work. To complete the objective of subtask 2.3.1 we have compared the CTD-derived geostrophic velocity with the ocean truth.

[5] https://oceanparcels.org/

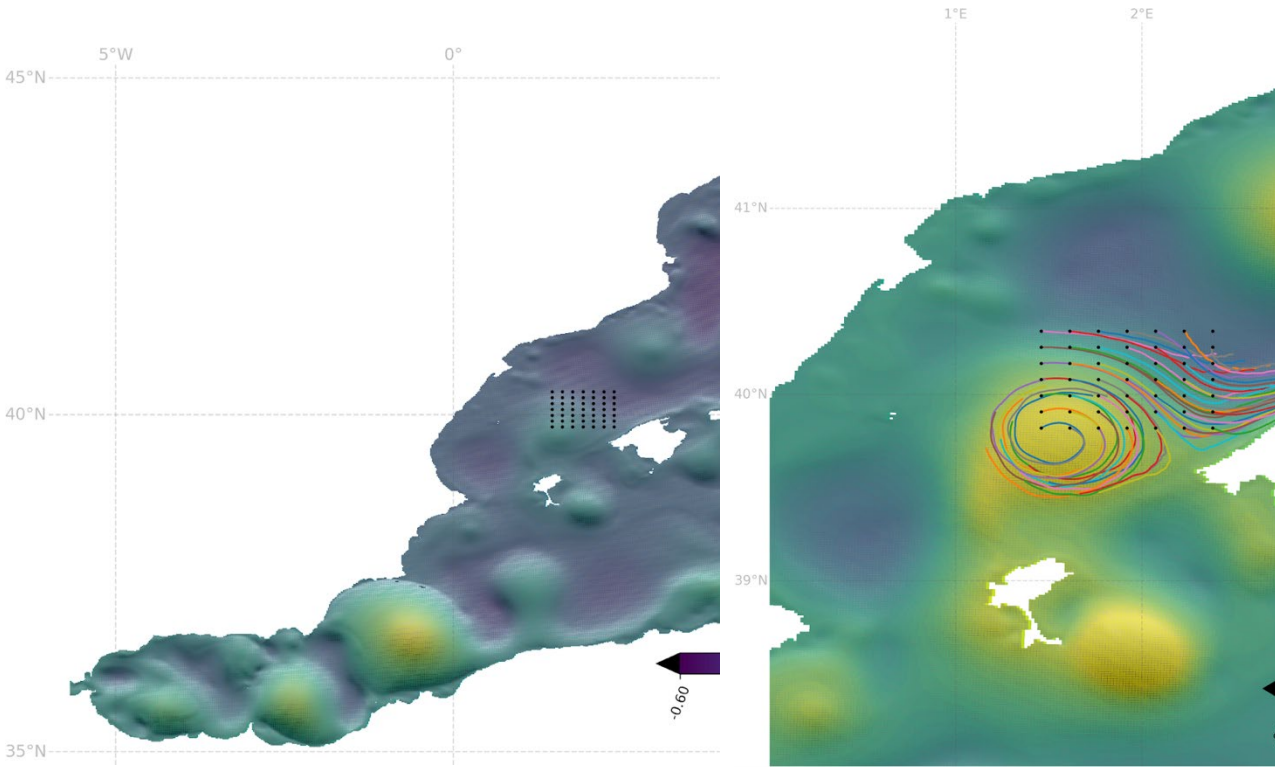

Figure 4: (a) Release position of the 49 drifters and (b) their trajectories over the 6-day period (from 1 to 7 of September 2009) computed with Ocean Parcels using currents at 15 m depth from the eNATL60 simulation in the Mediterranean. The SSH field is shown as background: (a) on the 1st of September and (b) averaged over the 6-day period.

Set 2: For the reconstruction of nadir altimetry SLA using drifters through the MIOST tool (subtask 2.3.3), 146 particles were evenly space released within the Mediterranean study region every 3 months during 1 year (Figure 5). The release dates for the 4 groups of drifters are: 1 July 2009, 1 October 2009, 1 January 2010 and 1 April 2010, respectively. The release positions form a regular grid separated by 45 times the model resolution (45/60º = 0.75º). The Lagrangian trajectories were computed and saved every 1 h during 4 months using horizontal currents at 15 m depth. Particles were removed from the set when they reached the regional boundaries (Figure 6).

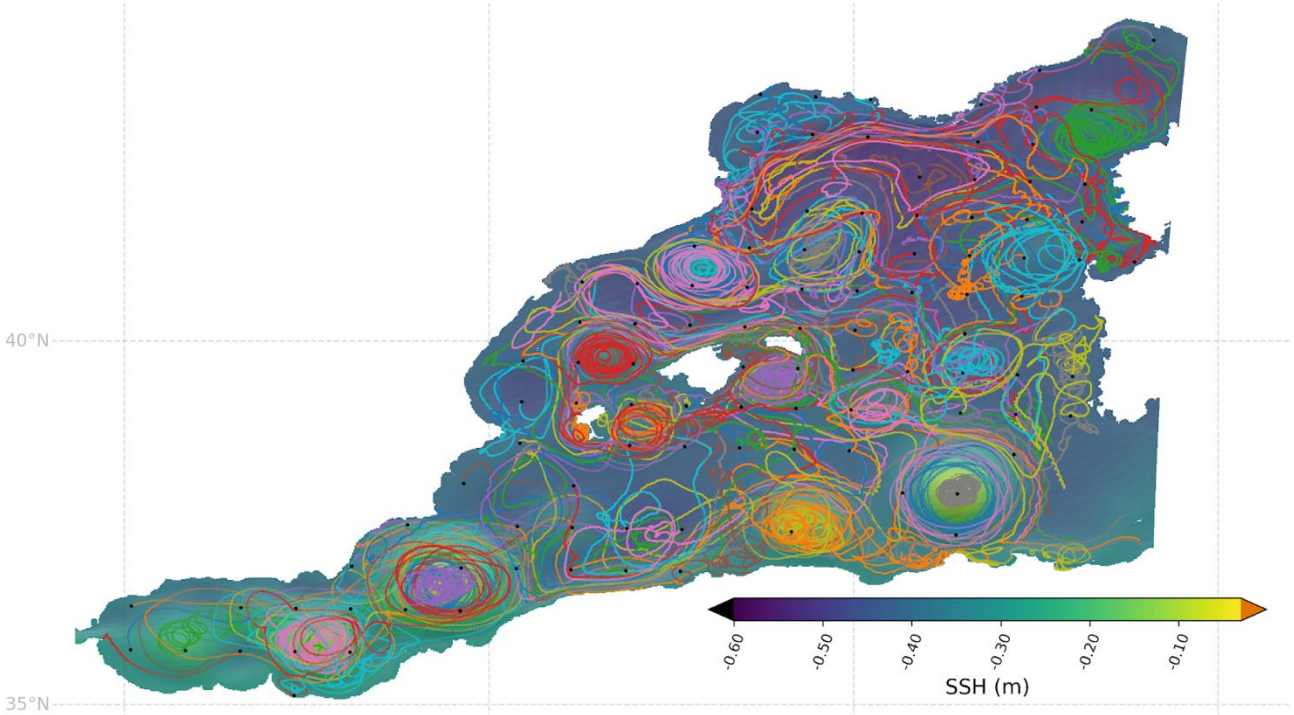

Figure 5: Initial location (black dots) and trajectories (one colour for each drifter trajectory) of the 105 Lagrangian particles that were released in the first group and stayed within the domain for the first period (1 July 2009 to 1 October 2009). Trajectories were computed with Ocean Parcels using horizontal currents at 15 m from the eNATL60 simulation. The averaged SSH field is shown as background.

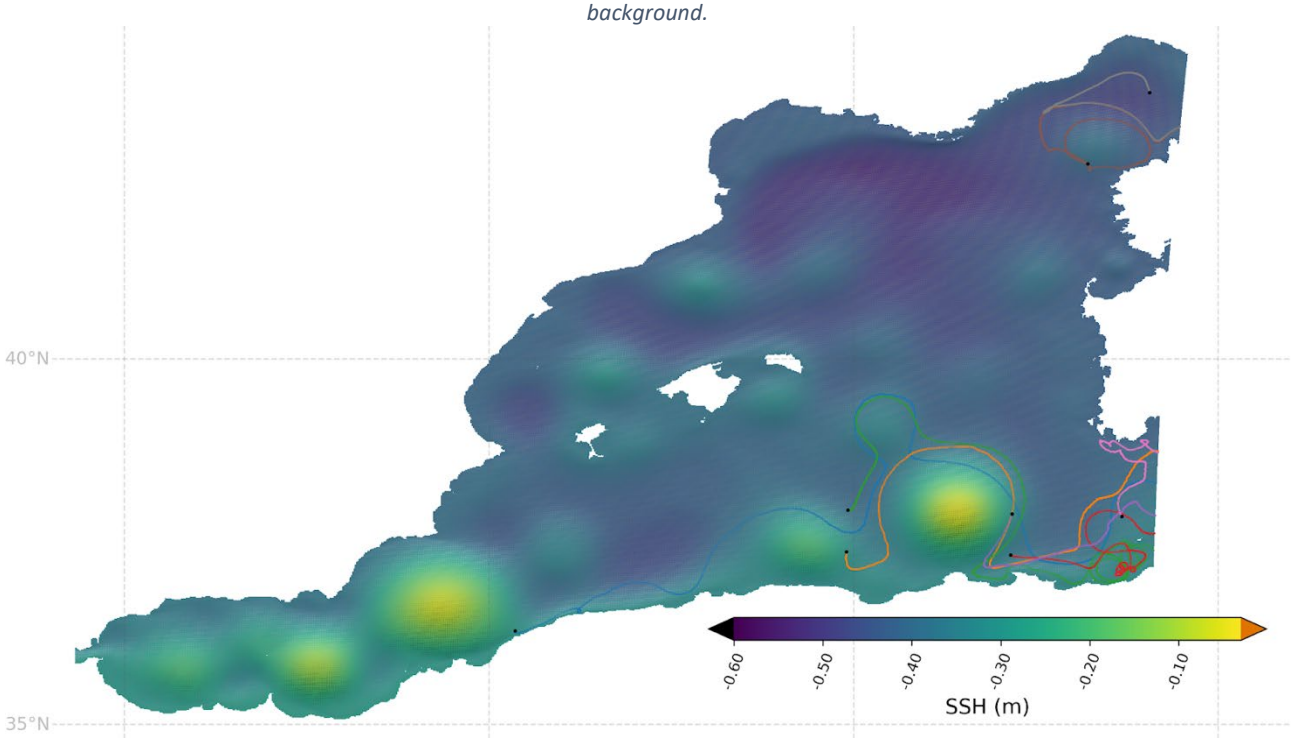

Figure 6: Example of the release position (black dots) and trajectories of 8 Lagrangian particles that left the domain in the 3rd month (2009-08) in the first group. The averaged SSH field is shown as background.

6.5. Nadir altimetry

Along-track nadir altimetry SSH and SLA fields have been extracted from the eNATL60 model in the Mediterranean. The observations have been simulated along tracks of Jason3, Altika, Cryosat-2 (c2n), H2B, Sentinel-3A and Sentinel-3B from 01-07-2020 to 31-12-2020, and from 01-01-2021 to 30-06-2021. Note that even if the model simulations are run in a common temporal period between 01-07-2009 and 30-06-2010, the simulated altimetric observing network represents the observing system in a recent period.

The along-track interpolation needed to extract the altimetric pseudo-observations is made with the "gonzag" software developed by Laurent Brodeau, openly available at https://github.com/brodeau/gonzag. This software interpolates in space and time 2D non-regular gridded model outputs onto satellite tracks (Figure 7). The 2D space interpolation is performed through the bilinear method.

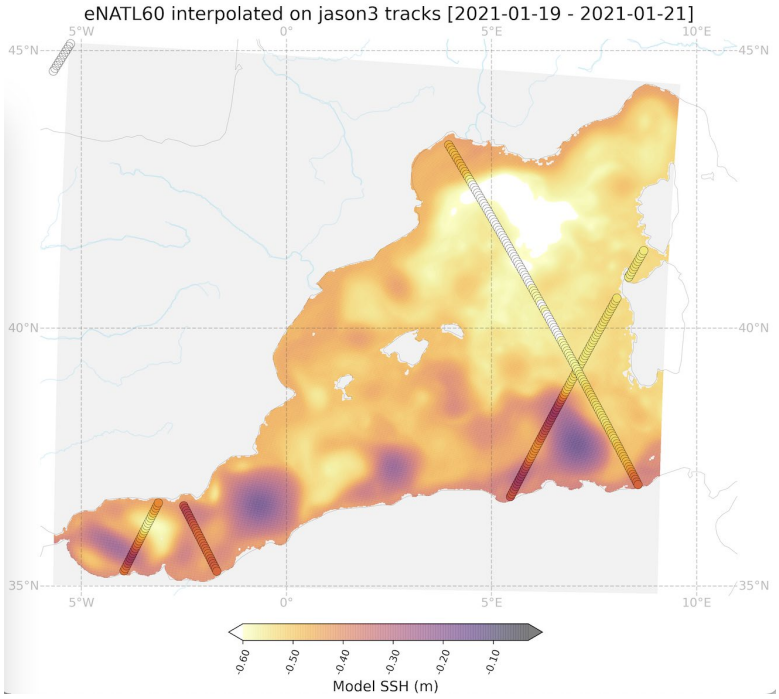

Figure 7: Example of interpolated SSH along Jason3 tracks (3-day period).

The simulated observations of SSH from eNATL60 exhibits rapid changes in sea level across the basin in time periods of 2-3 days. As explained by Ciani et al. (2021), this high-frequency variability is caused by rapidly moving atmospheric pressure disturbances causing storm surges and inverse barometer effects. These rapid changes in SSH cannot be handled by either the MIOST mapping or the WMOP data assimilation reconstruction. With real altimetry observation, this large-scale high-frequency variability is removed using the Dynamic Atmospheric Correction (DAC) derived from atmospheric forcing (Carrere et al. 2016).

Ciani et al. (2021) concluded that applying the DAC correction on their simulation was not satisfactory because significant residuals remained. They solved the issue filtering the large spatial scale of the model field using a Loess filter with a cutoff-length of 600 km before calculating the pseudo-observations. In our study 600 km is approximately the size of our basin, because of this we remove for each model time the spatial mean over the basin to filter the large spatial scales. The altimeter pseudo-observations are therefore sampled from the following calculated SLA field:

SLA(x,t) = SSH(x,t) – MDT(x) – M(t)

with MDT(x) the time mean over the 1-year period (2009-07-01 to 2010-06-31) and M(t) the spatial mean over the basin at each hourly model output (as a proxy for filtering out large spatial scales). Afterwards, to reconstruct the complete SSH signal, we add to the reconstructed SLA the MDT(x) and M(t).

6.6. Sea surface temperature

To apply the reconstruction with model data assimilation, sea surface temperature (SST) observations were simulated from eNATL60 model outputs in the Mediterranean. For the date of the analysis the daily mean surface temperature was considered. The field was first smoothed, using a radius of 10 km to filter out very small structures and simulate a similar effective resolution as the SST L4 product generally used in previous experiments[6]. Secondly, we subsampled the field, considering one observation every 10 km, as it is done in the WMOP operational system. Finally, we considered an SST observation noise generated randomly using a Gaussian distribution with standard deviation equal to the observation error (instrumental error 0.25ºC and representative error 0.5ºC).

6.7. Argo profiles

To implement the reconstruction based on model data assimilation, Argo temperature and salinity profiles were simulated from eNATL60 model outputs in the Mediterranean. The methodology consisted of linearly interpolating the model outputs to the position of the real floats available at present in the region of study in a centred time window of 5 days. We considered an observation noise generated randomly using a Gaussian distribution with standard deviation equal to the observation error (temperature: instrumental error 0.25ºC, representative error 0.1ºC; salinity: instrumental error 0.05, representative error 0.01). We vertically averaged the observations in bins, obtaining a single observation value per WMOP model grid cell. The variance of the observations in a grid cell is added to the observation error (see Hernández-Lasheras and Mourre 2018 for more information).

6.8. SWOT

The 2020 version of the SWOT Simulator[7] was used to simulate SWOT observations from eNATL60 model outputs in the Mediterranean and Atlantic study regions. Two different configurations of SWOT were simulated: the calval phase (fast-sampling) and the science phase (see Figures 8-11). SWOT pseudo-observations have not been used in the analysis shown in this deliverable because we perform the comparisons with the ocean truth provided by the model. However, in future work we may use the simulated SWOT observations to test, for instance, reconstruction methods based on machine-learning techniques.

[6] https://podaac.jpl.nasa.gov/dataset/JPL-L4UHfnd-GLOB-MUR
[7] https://github.com/CNES/swot_simulator

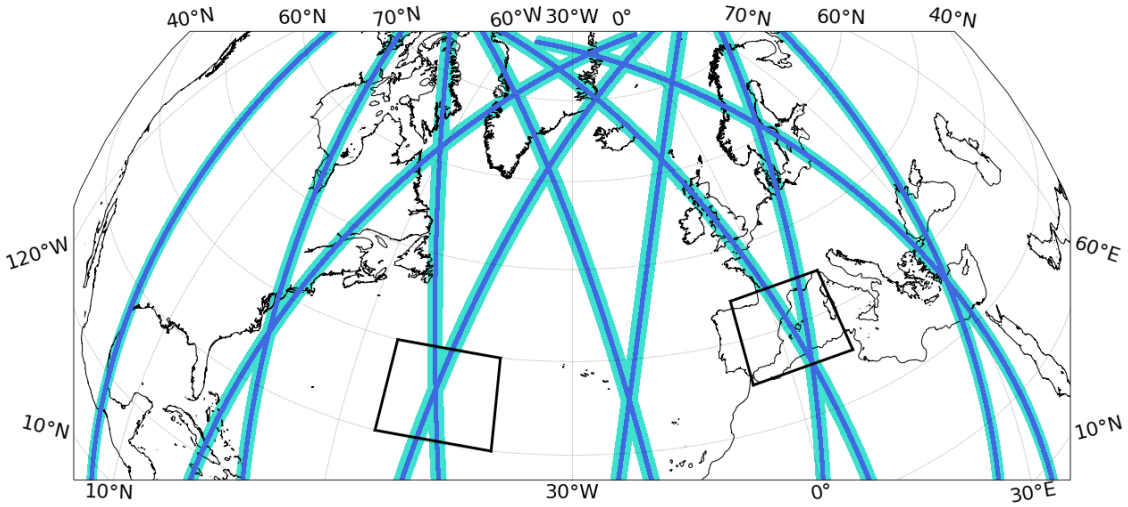

Figure 8: SWOT calval phase (fast-sampling) repeating trajectories. Black boxes show the study regions.

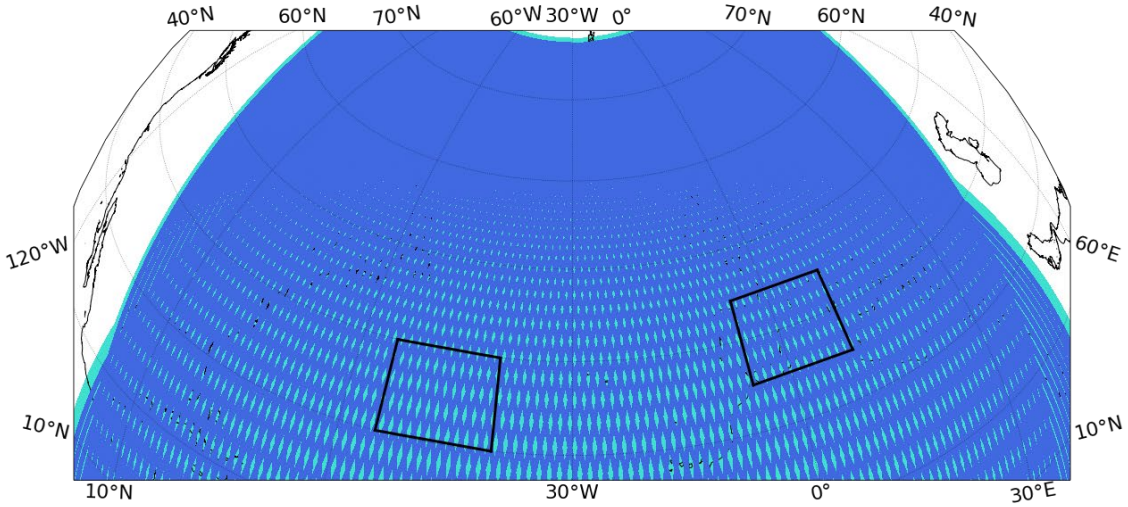

Figure 9: SWOT science phase trajectories. Black boxes show the study regions.

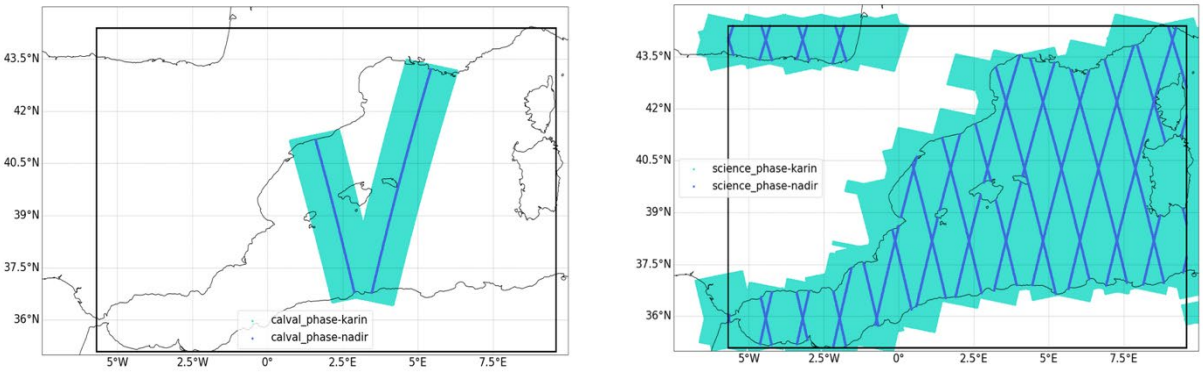

Figure 10: SWOT tracks in the Mediterranean study region: (left) calval phase and (right) science phase.

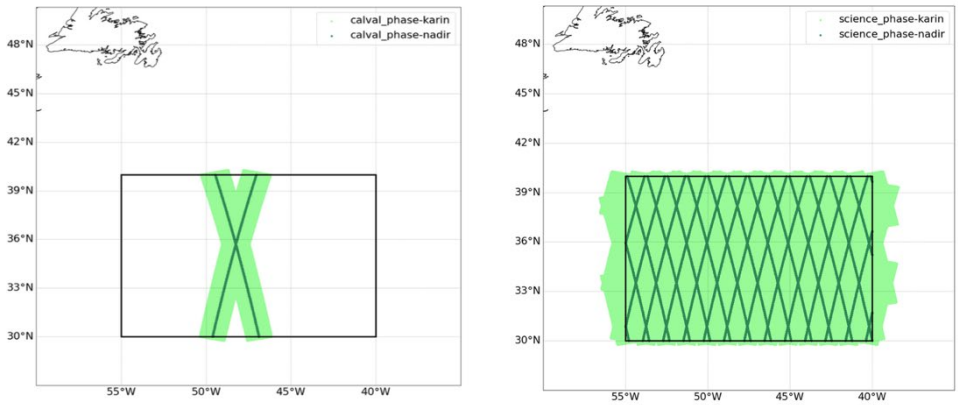

Figure 11: SWOT tracks in the Atlantic study region: (left) calval phase and (right) science phase.

7. Configurations

7.1. Configurations to evaluate different sampling strategies

Overview

Several configurations of the in situ experiment are simulated to evaluate the best sampling strategy to reconstruct fine-scale (~20 km) currents and validate SWOT during the fast-sampling phase. The reference configuration is similar to the PRE-SWOT cruise experiment sampling strategy (Barceló-Llull et al., 2021) in both regions of study within the selected sub-regions. Then, additional configurations are analysed modifying this reference setting to evaluate improvements in the sampling strategy. An overview of these configurations is shown in Tables 2 and 3, and the details of each configuration are presented in the next subsections.

Table 2. Overview of the different configurations simulated. Each configuration has been simulated for both the Mediterranean and Atlantic regions, with some differences in configurations 2a-d to adapt the configuration to each region.

Configuration	Start date	Instrument	Horizontal resolution	Minimum depth [m]	Maximum depth [m]	Vertical resolution [m]
Reference	1-9-2009	CTD	10 km	5	1000	0.5
1	1-9-2009	CTD	10 km	5	500	0.5
2a	1-9-2009	CTD	5 km	5	1000	0.5
2b	1-9-2009	CTD	8 km	5	1000	0.5
2c	1-9-2009	CTD	12 km	5	1000	0.5
2d	1-9-2009	CTD	15 km	5	1000	0.5
3a	1-9-2009	uCTD	6 km	5	500	0.5
3b	1-9-2009	uCTD	2.5 km	5	200	0.5
4	1-1-2010	CTD	10 km	5	1000	0.5
5	1-9-2009	glider CTD	6 km	30	500	1

Table 3. Sampling duration of each configuration in each region of study.

Configuration	Region	Sampling duration [days]
Reference	Mediterranean	4.3125
	Atlantic	4.3125
1	Mediterranean	3.0625
	Atlantic	3.0625
2a	Mediterranean	3.4375
	Atlantic	3.4375
2b	Mediterranean	4.0
	Atlantic	4.0
2c	Mediterranean	3.0625
	Atlantic	4.6875
2d	Mediterranean	2.4375
	Atlantic	5.1875
3a	Mediterranean	1.75
	Atlantic	1.75
3b	Mediterranean	1.75
	Atlantic	1.75

Configuration	Region	Sampling duration [days]
4	Mediterranean	4.3125
	Atlantic	4.3125
5	Mediterranean	3.625
	Atlantic	3.625

General assumptions

Some assumptions were made to simulate the different sampling strategies:

- The research vessel starts the sampling in the northwest corner of the sampling domain, it samples the first zonal transect from west to east, moves southward to the next zonal transect and samples the second transect from east to west; repeat for the other transects.
- We assume that the time needed to do a rosette CTD cast down to 500 m is 30 min, and 60 min for a cast down to 1000 m.
- We assume that during the CTD cast the water column properties do not change and we extract the model data corresponding to the time of the cast launch.
- ADCP observations in strategies including rosette CTD casts: for consistency with what is done in multi-platform experiments (Barceló-Llull et al., 2021), we exclude the ADCP observations during the CTD casts (ship stopped) and also in a distance smaller than the resolution of the ADCP profiles (time of ship decelerating/accelerating in real cruises).
- For the sampling strategy with underway CTD we assume constant ship velocity, also during ship turns, and turns of 90º.

Reference configuration

- *Coordinates defining the CTD grid (Figures 12 and 13):*
  - Med first CTD (top-left) = (1.45ºE, 40.415ºN)
  - Atlantic first CTD (top-left) = (48.70ºW, 35.25ºN)
- *Start date*: 1 September 2009
- *Rosette CTD casts*:
  - Number of zonal transects: 7
  - Number of casts in each transect: 9
  - Horizontal resolution of CTD profiles: 10 km
  - Vertical axis: from 5 to 1000 m depth, with a vertical spacing of 0.5 m
- *ADCP current velocities*:
  - Continuously recorded at a transit speed of 8 knots between CTD casts
  - We exclude ADCP data during the CTD casts (see “General assumptions”)
  - Horizontal resolution of ADCP profiles: 5 min (1.2 km)
  - Vertical axis: from 20 to 600 m depth, with a vertical spacing of 8 m

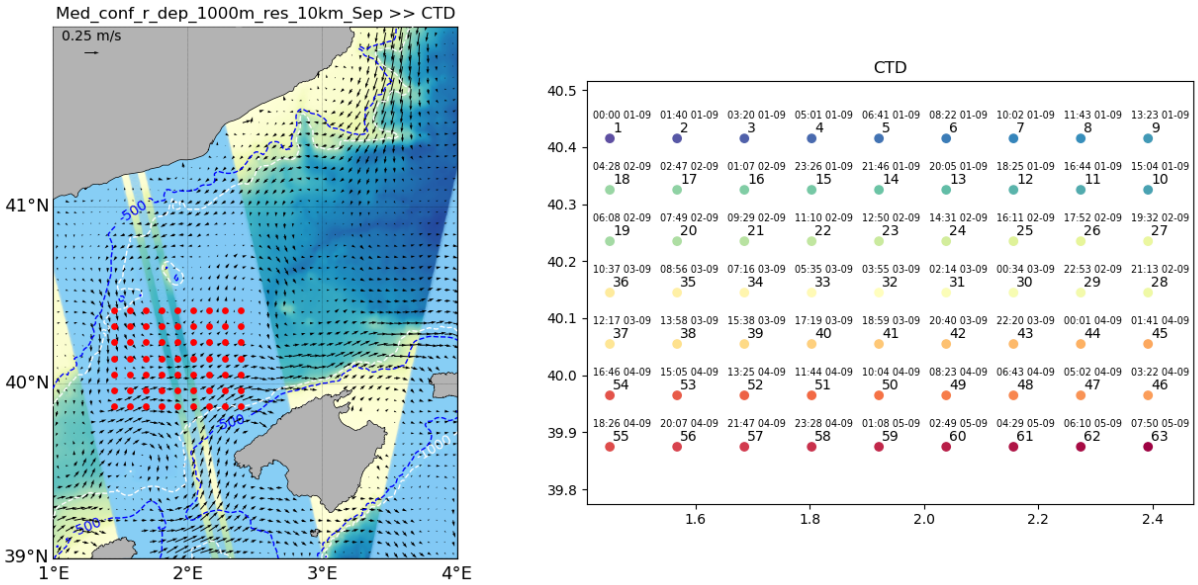

Figure 12: Reference configuration in the Mediterranean. (left) Red dots represent CTD profiles within a swath of SWOT during the fast-sampling phase (blue bands). (right) CTD profiles with date and time of CTD cast release.

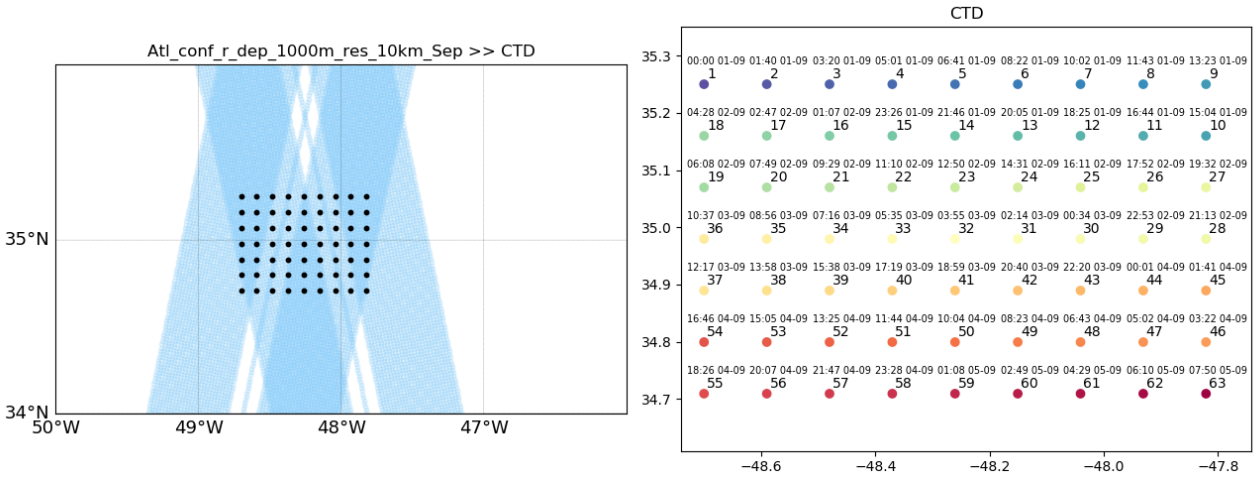

Figure 13: Reference configuration in the Atlantic. (left) Black dots represent CTD profiles within a crossover of SWOT during the fast-sampling phase (blue bands). (right) CTD profiles with date and time of CTD cast release.

Configuration 1

- *Coordinates defining the CTD grid:*
  - Med first CTD (top-left) = (1.45ºE, 40.415ºN)
  - Atlantic first CTD (top-left) = (48.70ºW, 35.25ºN)
- *Start date*: 1 September 2009
- *Rosette CTD casts (Figure 14)*:
  - Number of zonal transects: 7
  - Number of casts in each transect: 9
  - Horizontal resolution of CTD profiles: 10 km
  - Vertical axis: from 5 to 500 m depth, with a vertical spacing of 0.5 m

- *ADCP current velocities*:
  - Continuously recorded at a transit speed of 8 knots between CTD casts
  - We exclude ADCP data during the CTD casts
  - Horizontal resolution of ADCP profiles: 5 min (1.2 km)
  - Vertical axis: from 20 to 600 m depth, with a vertical spacing of 8 m

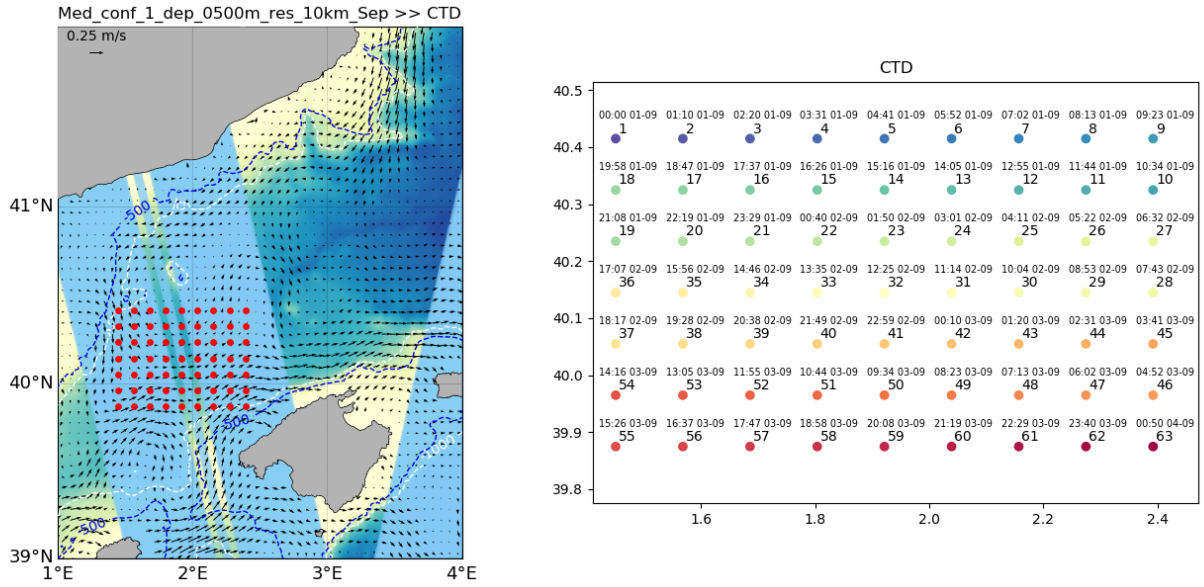

Figure 14: Configuration 1 in the Mediterranean. (left) Red dots represent CTD profiles within a swath of SWOT during the fast-sampling phase (blue bands). (right) CTD profiles with date and time of CTD cast release.

Configuration 2

- *oordinates defining the CTD grid (Figures 15-22):*
  - Med first CTD (top-left):
    - Med start point 5 km: (1.45+0.23ºE, 40.415-0.13ºN) = (1.68ºE, 40.285ºN)
    - Med start point 8 km: (1.45+0.093ºE, 40.415-0.055ºN) = (1.543ºE, 40.36ºN)
    - Med start point 12 km: (1.45ºE, 40.415ºN)
    - Med start point 15 km: (1.45ºE, 40.415ºN)
  - Atlantic first CTD (top-left): the start point is adjusted in the 12 km and 15 km configurations to have the grid centered.
    - Atl start point 5 km: (48.70ºW, 35.25ºN)
    - Atl start point 8 km: (48.70ºW, 35.25ºN)
    - Atl start point 12 km: (48.78ºW, 35.25ºN)
    - Atl start point 15 km: (48.91ºW, 35.35ºN)
- *Start date*: 1 September 2009
- *Rosette CTD casts*:
  - Number of zonal transects: 7, except:
    - Med, 12 km: 6
    - Med, 15 km: 5
  - Number of casts in each transect: 9, except:
    - Med, 12 km: 7 (To stay in deep waters)
    - Med, 15 km: 6 (To stay in deep waters)
  - Horizontal resolution of CTD profiles: 5, 8, 12, 15 km (2a, 2b, 2c, 2d, respectively)
  - Vertical axis: from 5 to 1000 m depth, with a vertical spacing of 0.5 m

- *ADCP current velocities*:
  - Continuously recorded at a transit speed of 8 knots between CTD casts
  - We exclude ADCP data during the CTD casts (see assumptions)
  - Horizontal resolution of ADCP profiles: 5 min (1.2 km)
  - Vertical axis: from 20 to 600 m depth, with a vertical spacing of 8 m

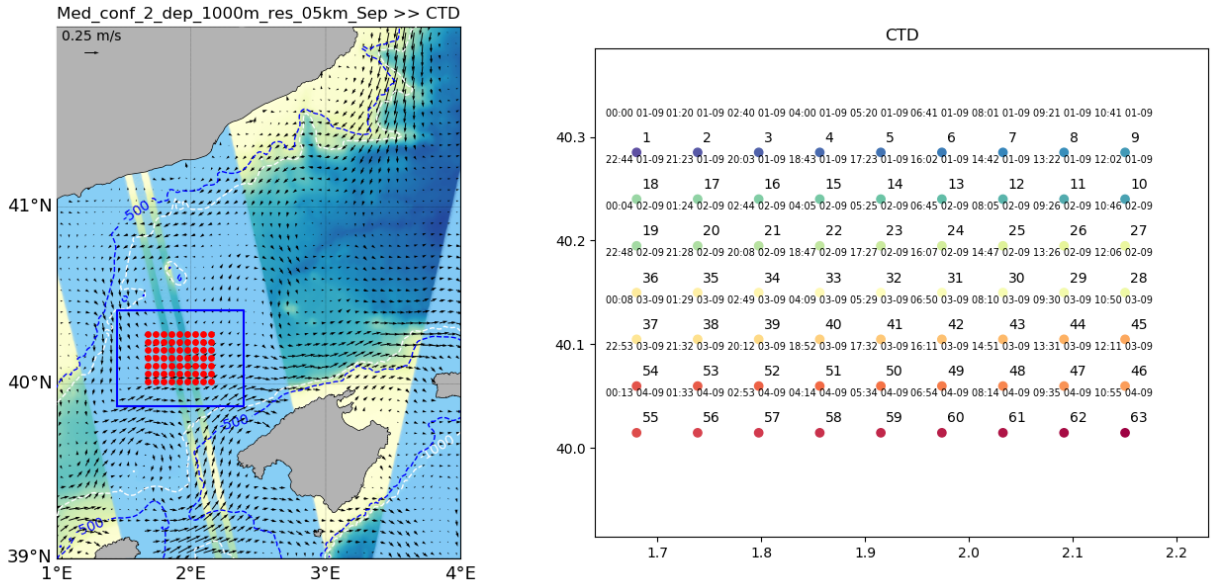

Figure 15: Configuration 2a (5 km) in the Mediterranean. (left) Red dots represent CTD profiles within a swath of SWOT during the fast-sampling phase (blue bands), blue box delimits the reference configuration domain. (right) CTD profiles with date and time of the cast release.

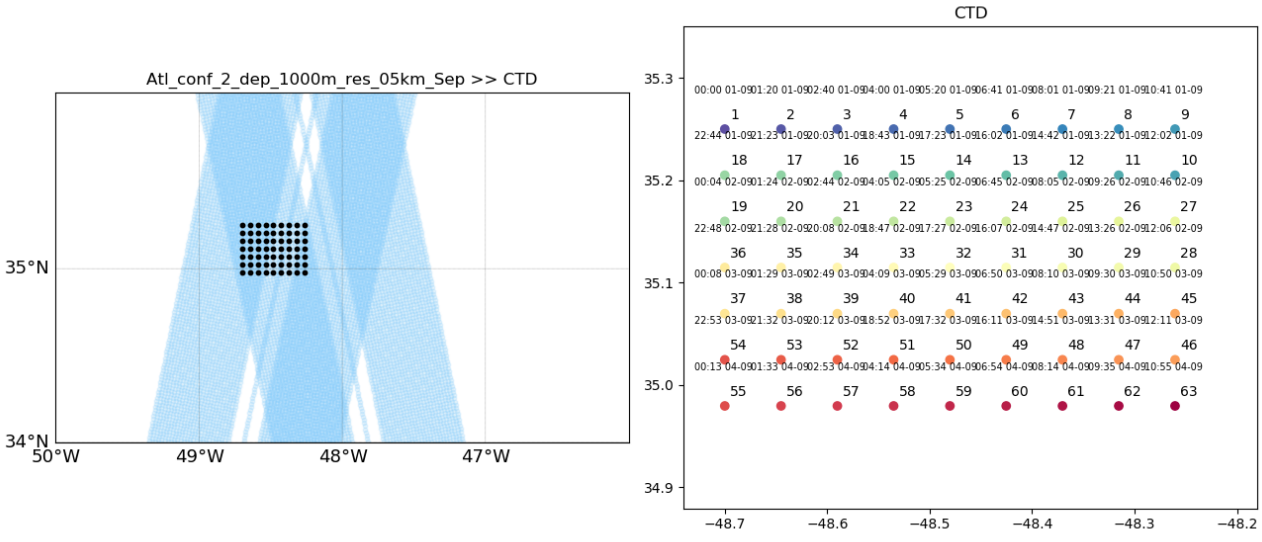

Figure 16: Configuration 2a (5 km) in the Atlantic. (left) Black dots represent CTD profiles within a crossover of SWOT during the fast-sampling phase (blue bands). (right) CTD profiles with date and time of the cast release.

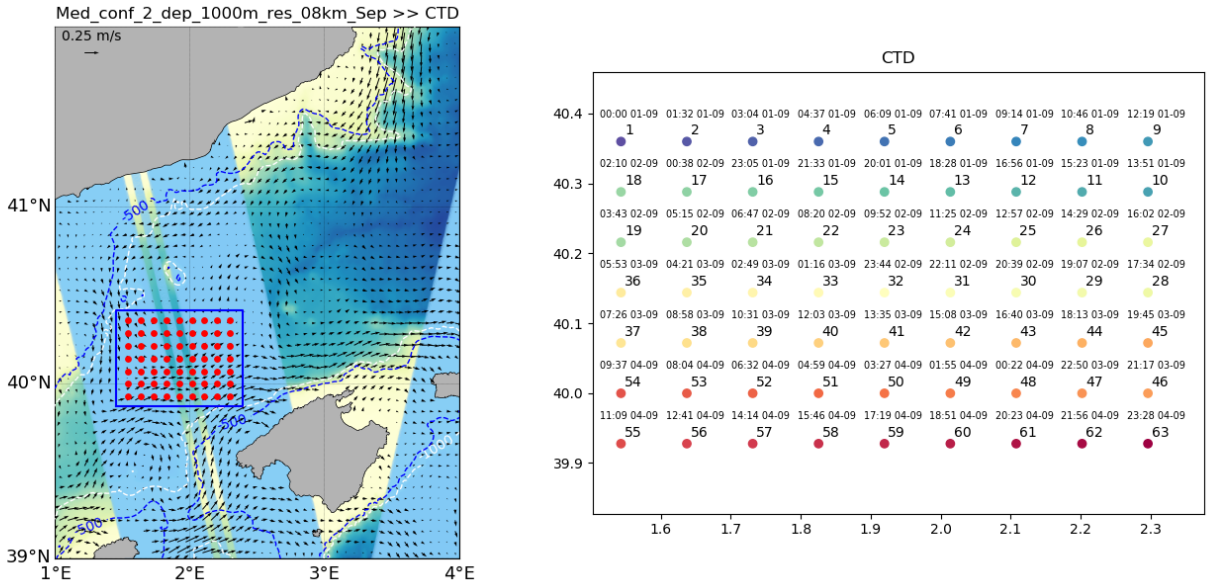

Figure 17: Configuration 2b (8 km) in the Mediterranean. (left) Red dots represent CTD profiles within a swath of SWOT during the fast-sampling phase (blue bands), blue box delimits the reference configuration domain. (right) CTD profiles with date and time of the cast release.

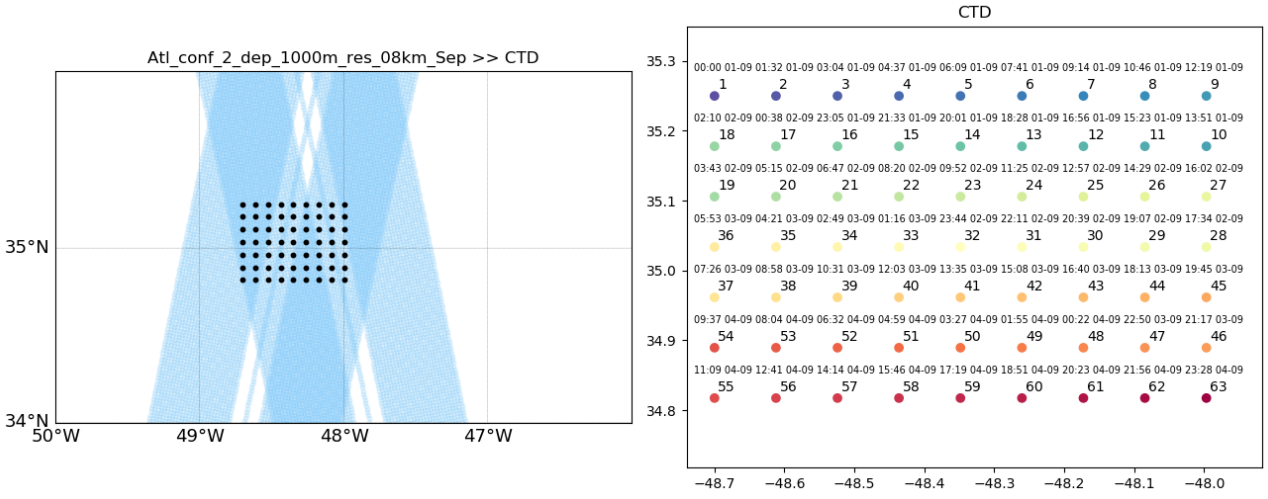

Figure 18: Configuration 2b (8 km) in the Atlantic. (left) Black dots represent CTD profiles within a crossover of SWOT during the fast-sampling phase (blue bands). (right) CTD profiles with date and time of the cast release.

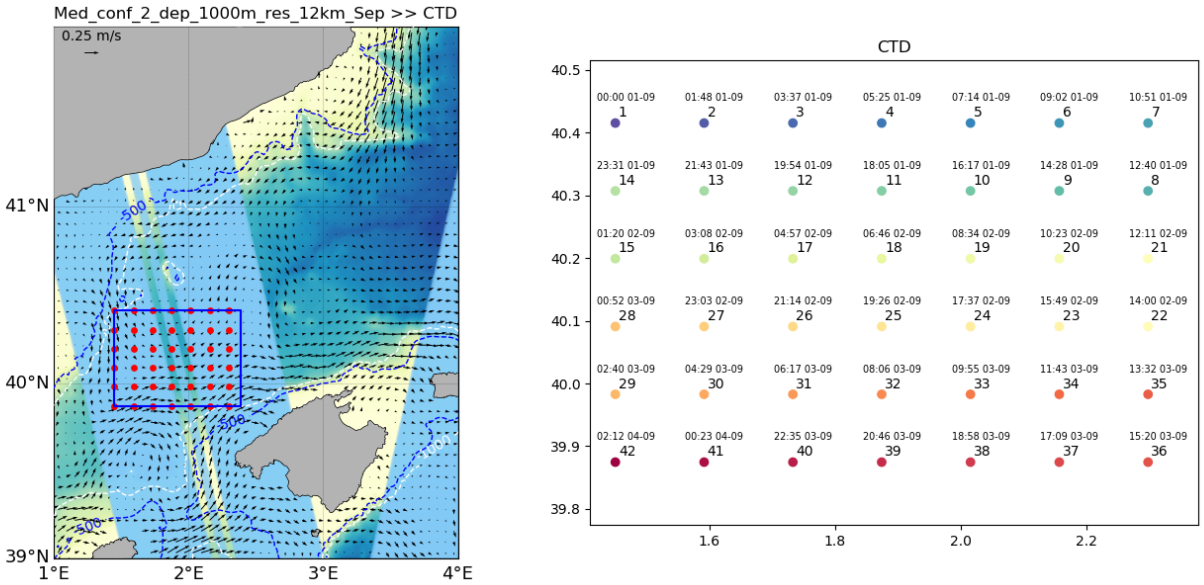

Figure 19: Configuration 2c (12 km) in the Mediterranean. (left) Red dots represent CTD profiles within a swath of SWOT during the fast-sampling phase (blue bands), blue box delimits the reference configuration domain. (right) CTD profiles with date and time of the cast release.

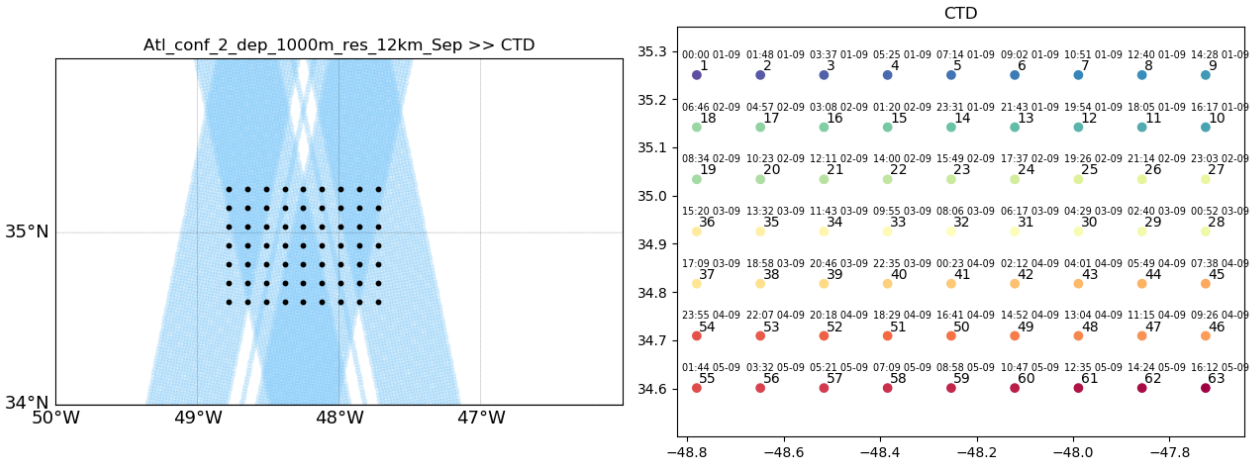

Figure 20: Configuration 2c (12 km) in the Atlantic. (left) Black dots represent CTD profiles within a crossover of SWOT during the fast-sampling phase (blue bands). (right) CTD profiles with date and time of the cast release.

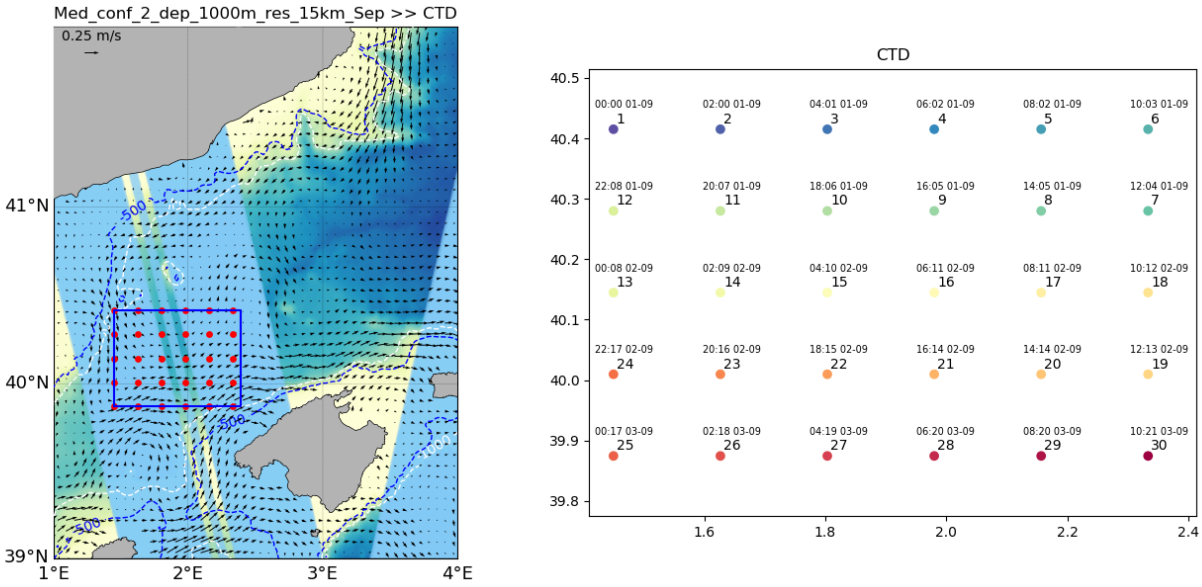

Figure 21: Configuration 2d (15 km) in the Mediterranean. (left) Red dots represent CTD profiles within a swath of SWOT during the fast-sampling phase (blue bands), blue box delimits the reference configuration domain. (right) CTD profiles with date and time of the cast release.

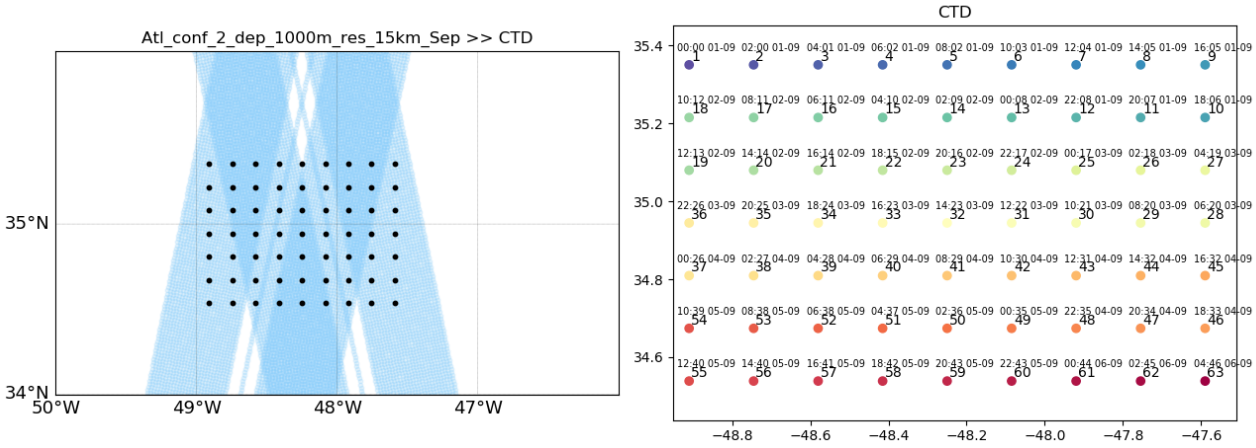

Figure 22: Configuration 2d (15 km) in the Atlantic. (left) Black dots represent CTD profiles within a crossover of SWOT during the fast-sampling phase (blue bands). (right) CTD profiles with date and time of the cast release.

Configuration 3

- *Top-left start point:*
  - Med = (1.45ºE, 40.415ºN)
  - Atl = (48.70ºW, 35.25ºN)
- *Start date*: 1 September 2009
- *uCTD profiles (Figures 23 and 24)*:
  - Continuously recorded at a transit speed of 8 knots
  - Number of zonal transects: 7
  - Longitude of the zonal transects: 80 km
  - Separation between zonal transects: 10 km
  - Configuration 3a:
    - Horizontal resolution of uCTD profiles: 6 km
    - Vertical axis: from 5 to 500 m depth, with a vertical spacing of 0.5 m

- Configuration 3b:
  - Horizontal resolution of uCTD profiles: 2.5 km
  - Vertical axis: from 5 to 200 m depth, with a vertical spacing of 0.5 m

- *ADCP current velocities*:
  - Continuously recorded at a transit speed of 8 knots
  - Horizontal resolution of ADCP profiles: 5 min (1.2 km)
  - Vertical axis: from 20 to 600 m depth, with a vertical spacing of 8 m

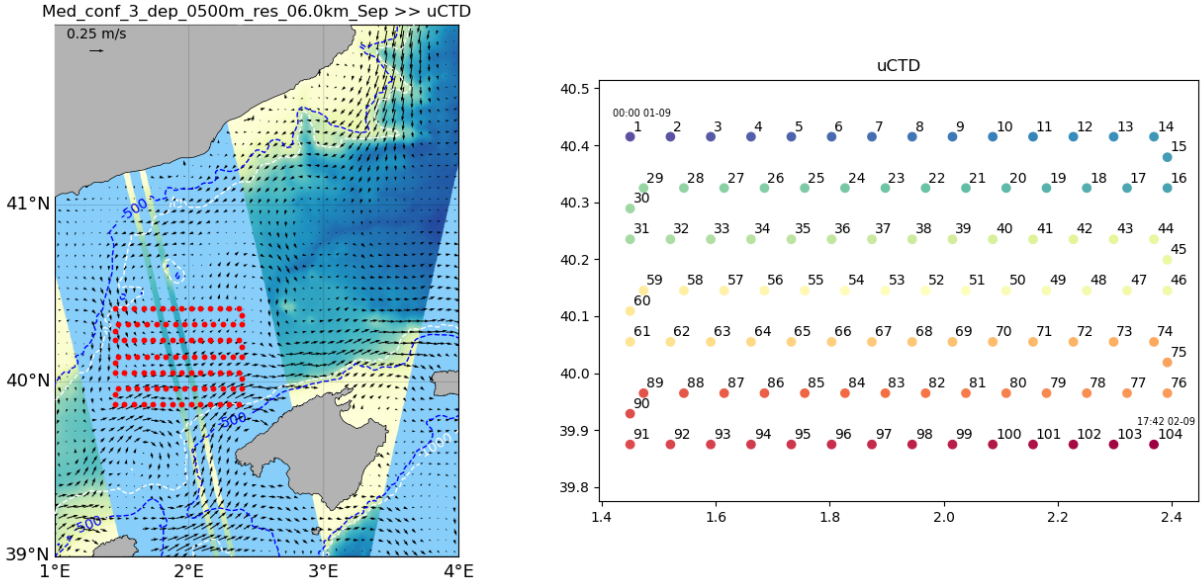

Figure 23: Configuration 3a in the Mediterranean. (left) Red dots represent underway CTD profiles within a swath of SWOT during the fast-sampling phase (blue bands). (right) Underway CTD profiles with initial and final dates.

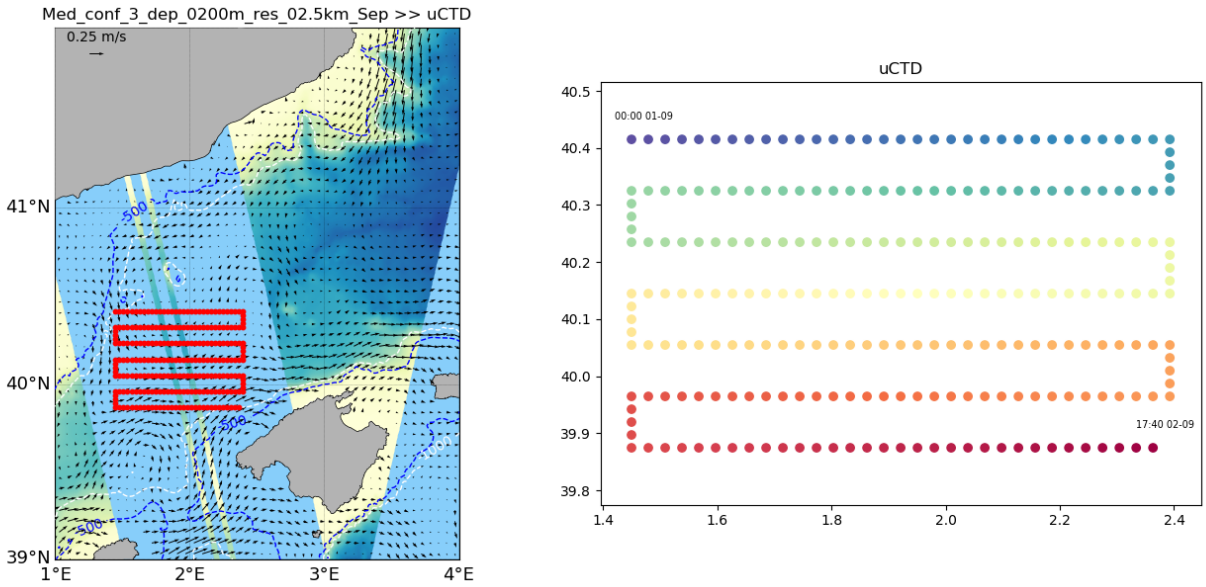

Figure 24: Configuration 3b in the Mediterranean. (left) Red dots represent underway CTD profiles within a swath of SWOT during the fast-sampling phase (blue bands). (right) Underway CTD profiles with initial and final dates.

Configuration 4

- *Coordinates defining the CTD grid:*
  - Med first CTD (top-left) = (1.45ºE, 40.415ºN)
  - Atlantic first CTD (top-left) = (48.70ºW, 35.25ºN)
- *Start date*: 1 January 2010
- *Rosette CTD casts (Figure 25)*:
  - Number of zonal transects: 7
  - Number of casts in each transect: 9
  - Horizontal resolution of CTD profiles: 10 km
  - Vertical axis: from 5 to 1000 m depth, with a vertical spacing of 0.5 m
- *ADCP current velocities*:
  - Continuously recorded at a transit speed of 8 knots between CTD casts
  - We exclude ADCP data during the CTD casts
  - Horizontal resolution of ADCP profiles: 5 min (1.2 km)
  - Vertical axis: from 20 to 600 m depth, with a vertical spacing of 8 m

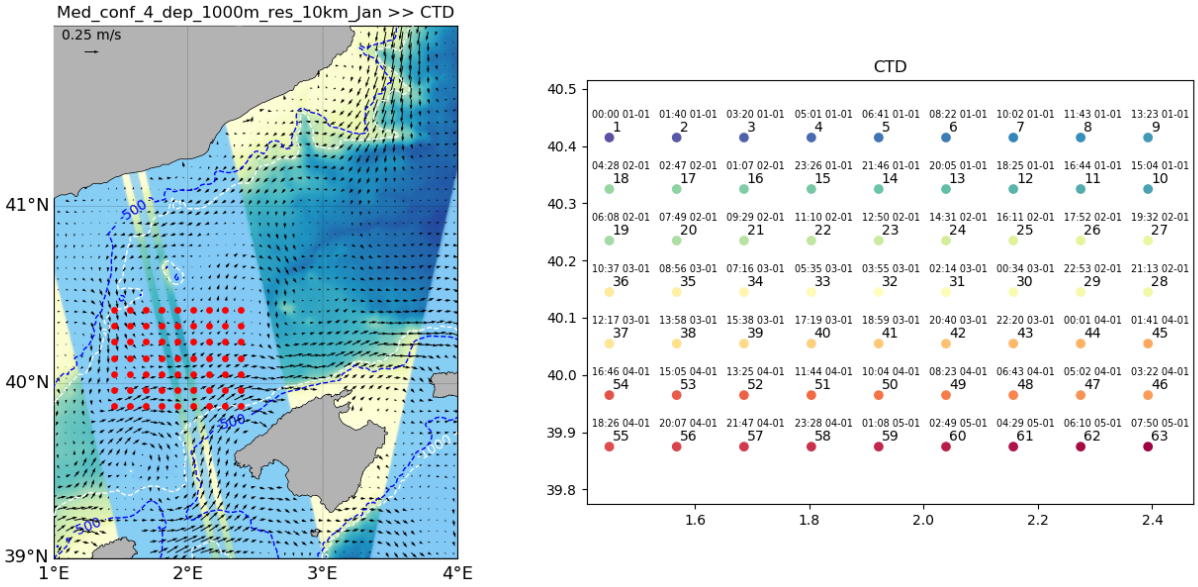

Figure 25: Configuration 4 in the Mediterranean. (left) Red dots represent CTD profiles within a swath of SWOT during the fast-sampling phase (blue bands). (right) CTD profiles with date and time of CTD cast release.

Configuration 5

- *Start date*: 1 September 2009
- *7 gliders (Figures 26 and 27)*:
  - Each one sampling a zonal transect from east to west and simultaneously
  - Constant glider velocity of 0.25 m/s
  - End point of the northern glider transect (north-west):
    - Med = (1.45ºE, 40.415ºN), same as the first CTD in the reference configuration.
    - Atl = (48.70ºW, 35.25ºN)
  - Length of glider transects: 80 km
  - Separation between transects: 10 km

- Horizontal resolution of the glider CTD profiles: 6 km
- Vertical axis: from 30 to 500 m depth, with a vertical spacing of 1 m (as in L2 glider data, e.g. PRE-SWOT)

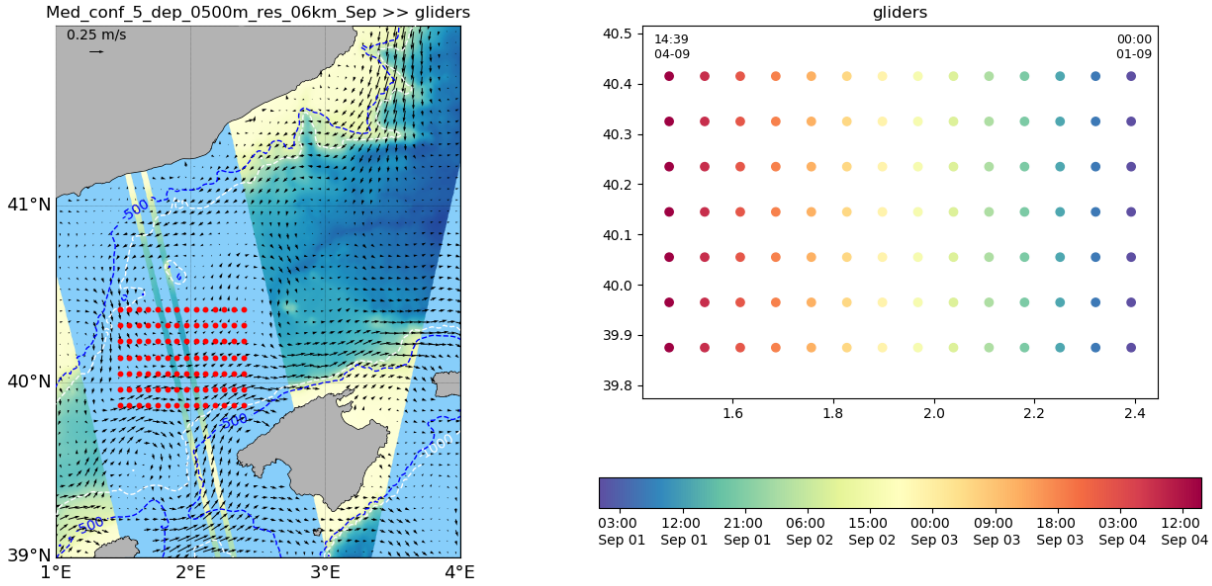

Figure 26: Configuration 5 in the Mediterranean. (left) Red dots represent CTD profiles from 7 gliders sampling simultaneously 7 zonal lines from east to west. (right) Glider CTD profiles with initial and final dates.

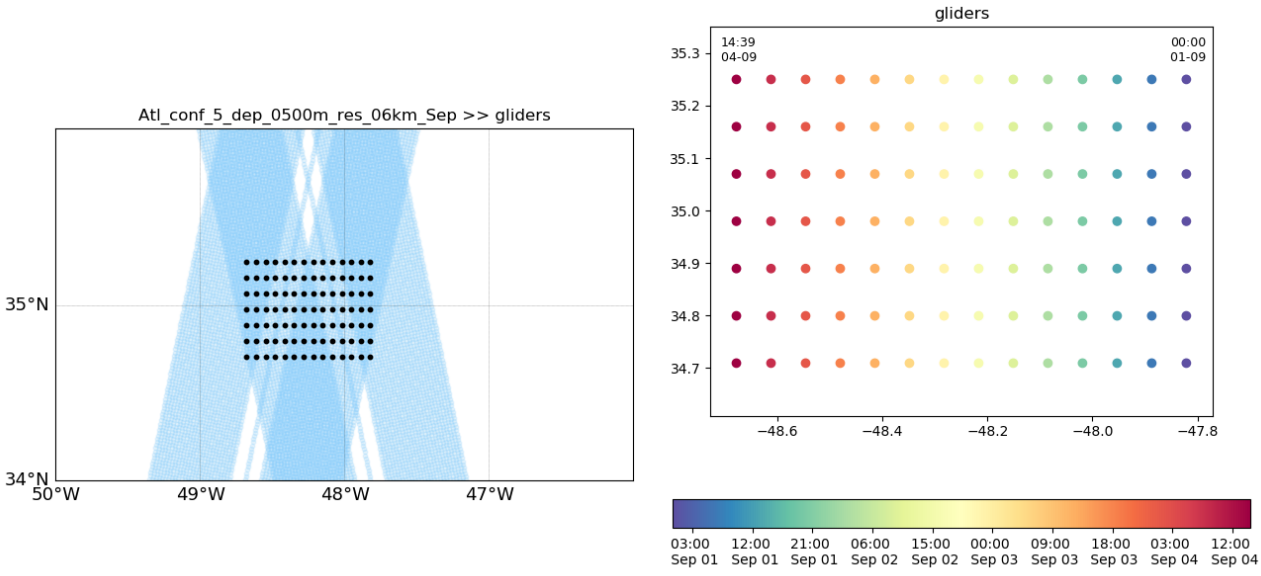

Figure 27: Configuration 5 in the Atlantic. (left) Black dots represent CTD profiles from 7 gliders sampling simultaneously 7 zonal lines from east to west. (right) Glider CTD profiles with initial and final dates.

7.2. Configurations to test different reconstruction methods

To achieve the second objective, we planned to select two common configurations in the Mediterranean to apply the reconstruction methods:

- the reference configuration
- the best configuration identified in subtask 2.3.1

As the reference configuration is a sampling strategy that provides good reconstructed fields in the Mediterranean (see Section 10), we evaluate the different methods of reconstruction only for the reference configuration.

7.3. Configurations to apply the MIOST tool

To accomplish objective 3, we merge with the MIOST tool (see next section) the velocity estimated from simulated drifters with simulated observations of the conventional nadir altimetry to compute daily maps of SLA and surface currents with a grid resolution of 1/16°. In a first experiment we only use nadir altimetry. Then we add a number of drifters representative of the coverage at present, and finally we triple that number of drifters. All the experiments are compared to each other to quantify the impact of each observation system. We also compare the reconstructed fields from each experiment to the ocean truth.

8. Reconstruction methods

8.1. Optimal interpolation

Optimal Interpolation is a powerful method of data analysis that has been widely used by oceanographers and meteorologists to estimate values of geophysical variables on a regular grid from irregularly sampled observations (e.g. Bretherton et al., 1976; Davis, 1985; Le Traon, 1990, Gomis et al., 2001; Pascual et al., 2004, 2017; Escudier et al., 2013; Melnichenko et al., 2014, Barceló-Llull et al., 2017, 2021; Ruiz et al., 2019). This technique determines a point-wise estimate of the interpolated field with minimum ensemble mean-square error, considering information about the variances and correlation functions of the estimated field and the observational data. This method has the advantage to consider error information for each observational platform.

Spatial optimal interpolation

The optimal interpolation algorithm used in field experiments to interpolate CTD and ADCP observations considers the spatial variability and correlation scale of the measurements (e.g., Rudnick, 1996; Pascual et al., 2004; Barceló-Llull et al., 2017, 2021; Ruiz et al., 2019). With this approach the observations collected during the sampling period are considered quasi-synoptic, i.e., they are assumed to represent a stationary state of the ocean at the scales resolved by the sampling. For clarity, from here on this method will be referred to as "spatial optimal interpolation".

In a first analysis, temperature (T) and salinity (S) simulated observations were interpolated onto a regular 3D grid using (i) linear interpolation to interpolate vertically each profile with a vertical spacing of 5 m and (ii) spatial optimal interpolation to interpolate horizontally onto a grid with a spatial resolution of 2 km and applying spatial correlation scales of 25 km (semimajor and semiminor axes of the 2D Gaussian function used to fit the data covariance). The new grid was defined for each configuration by the (longitude, latitude) limits

of the original CTD grid and considering a horizontal resolution of 2 km. The mean fields were assumed to be planar and the uncorrelated noise for the interpolation of temperature and salinity was assumed to be 3% of the signal energy (Barceló-Llull et al., 2021). With the reconstructed T and S 3D fields, we computed the dynamic height (DH) and the corresponding geostrophic velocity (ugeo, vgeo) at the ocean upper layer (5 m for the configurations with CTD/uCTD, 30 m for the glider configuration).

After reconstructing all configurations with the spatial optimal interpolation, we compared the reconstructed DH to the model SSH (ocean truth). First, we needed to define the ocean truth and, as the reconstructed field is supposed to represent a stationary state of the ocean during the sampling period, we performed a sensitivity test. We compared the reconstructed DH to the model SSH on the first, last and central date of the sampling period, and to the averaged field. The results revealed high sensitivity to the field used as the ocean truth. The comparison was done in the same domain for all configurations (domain of configuration 2a), to avoid sensitivity of the results to the domain size. We removed the spatial mean of DH and SSH to the corresponding fields to compare anomalies. Model fields were linearly interpolated to the grid of the reconstruction.

This analysis highlighted the need to use an advanced version of the optimal interpolation that considers the spatio-temporal variability and correlation scale of the observations and from which the resulting map represents a specific date of the sampling period. This method is used to reconstruct altimetry observations (e.g. Escudier et al., 2013) and is explained in the next section.

Spatial correlation scale analysis

The spatial correlation scale was defined after calculating the empirical correlation from T and S pseudo-observations at 100 m depth (approach followed by Barceló-Llull et al., 2021) for each model and region and for the reference configuration (Figures 28 and 33). We concluded that using correlation scales of 25 km was a good compromise between the results obtained from the different models in both regions.

We also calculated the empirical correlation from the original model data averaged for the period of the configuration and including all data inside the configuration domain (Figures 29 and 34). We found consistent results with both approaches, and a sensitivity to the size of the domain. Using model data in bigger domains we obtain higher spatial correlation scales (Figures 30-31 and 35-36). Also, the results are sensitive to the sampling period. With pseudo-observations from configuration #4 (same configuration as the reference but in January) we obtain lower spatial correlation scales (Figures 32 and 37). This is expected because in winter the structures are smaller (reduced Rossby radius of deformation). On the other hand, performing the same analysis in the Mediterranean and Atlantic study regions revealed similar results: ~25 km in the Mediterranean vs. ~20 km in the Atlantic.

Empirical correlation in the Mediterranean

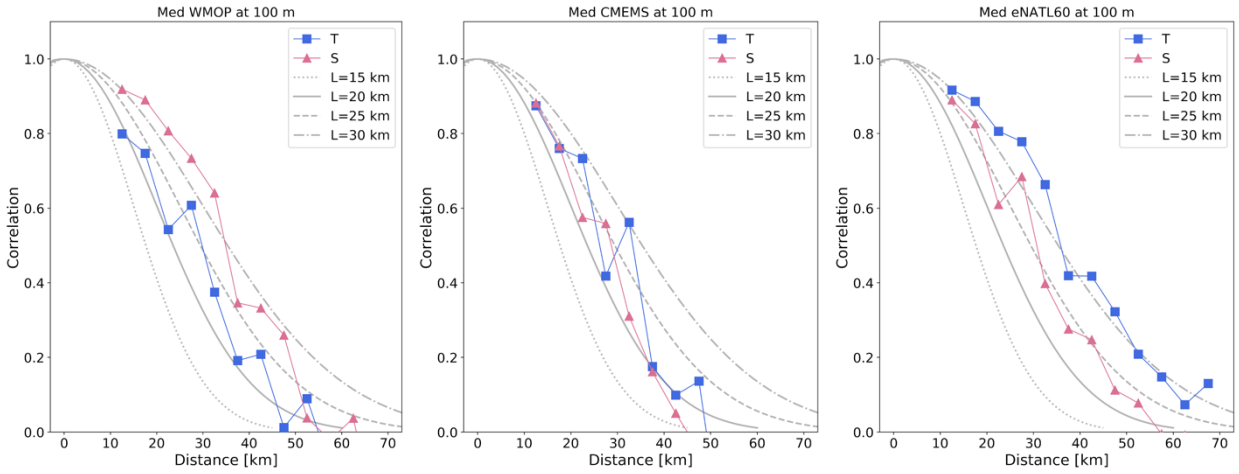

Figure 28: Empirical correlation calculated from the reference configuration pseudo-observations at 100 m depth for each model (CMEMS, WMOP, eNATL60). Correlation between data pairs that are separated by a defined distance (x-axis) and considering a bin size of 5 km for temperature and salinity. Grey lines represent four Gaussian functions with standard deviations of 15, 20, 25, and 30 km. Considering all models, the Gaussian function that resembles better the empirical correlations is the Gaussian with a standard deviation of 25 km.

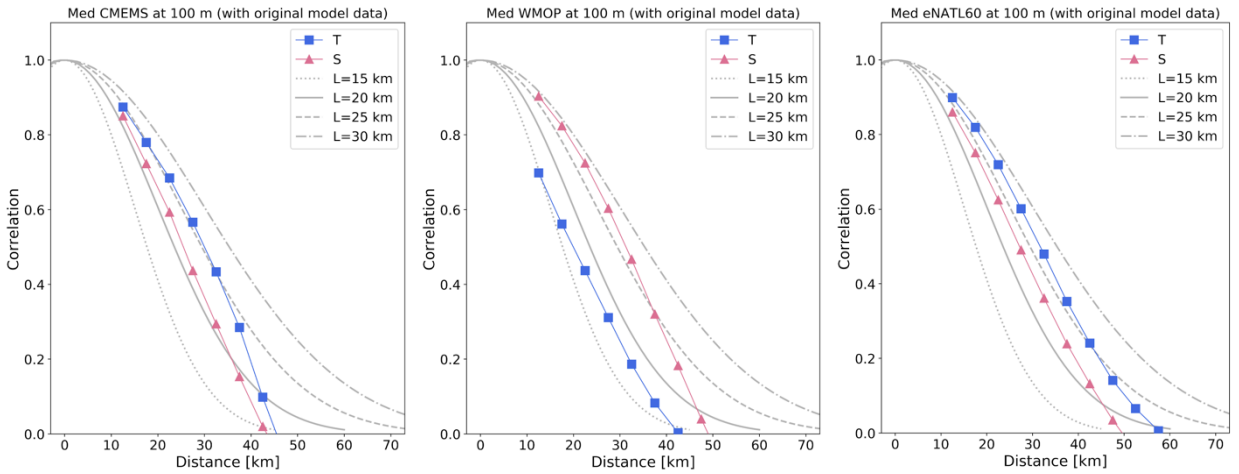

Figure 29: Empirical correlation calculated from the original model data averaged for the period of the configuration and including all data inside the domain of the configuration. Correlation between data pairs that are separated by a defined distance (x-axis) and considering a bin size of 5 km for temperature and salinity. Grey lines represent four Gaussian functions with standard deviations of 15, 20, 25, and 30 km. Considering all models, the Gaussian function that resembles better the empirical correlations is the Gaussian with a standard deviation of 25 km.

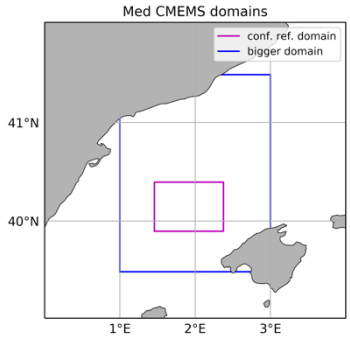

Figure 30: Map in the Mediterranean with the reference configuration domain (magenta box) and the bigger domain (blue box).

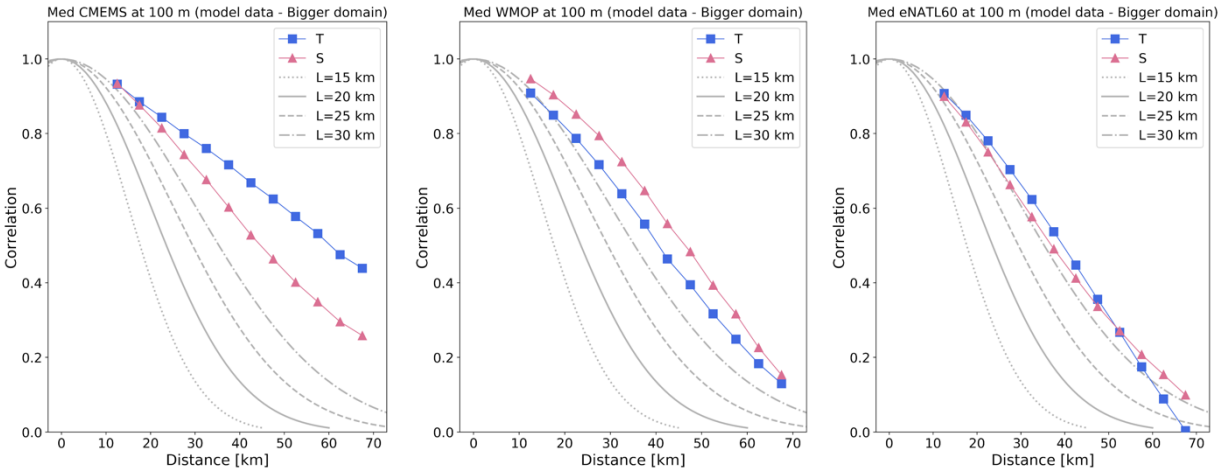

Figure 31: Empirical correlation calculated from the original model data averaged for the period of the reference configuration and including all data inside the bigger domain (blue box in the map). Correlation between data pairs that are separated by a defined distance (x-axis) and considering a bin size of 5 km for temperature and salinity. Grey lines represent four Gaussian functions with standard deviations of 15, 20, 25, and 30 km. The empirical correlation depends on the size of the domain (see Figure 29 for the results in the reference domain (magenta box in the map)).

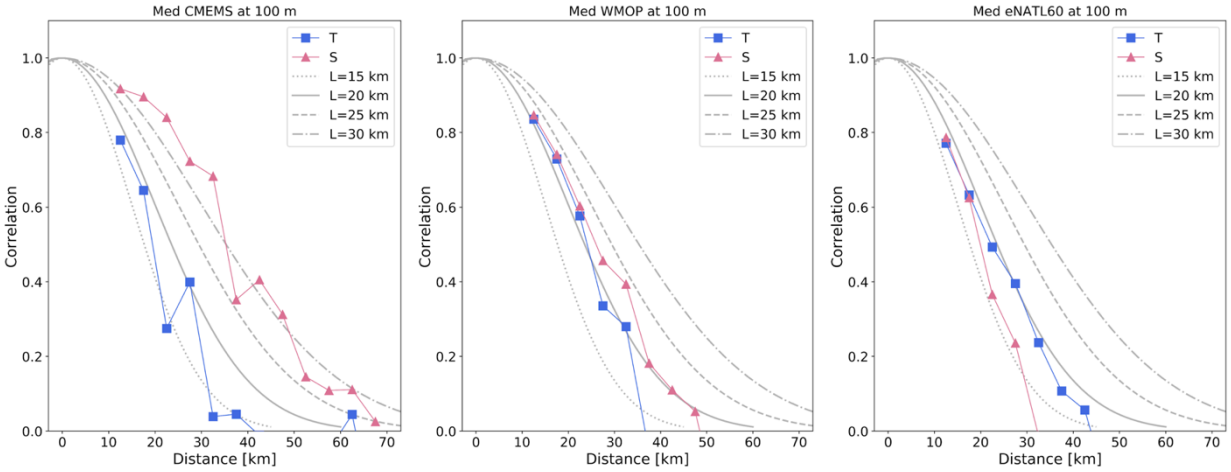

Figure 32: Empirical correlation calculated from the configuration #4 (as the reference configuration but in January) pseudo-observations at 100 m depth for each model (CMEMS, WMOP, eNATL60). Correlation between data pairs that are separated by a defined distance (x-axis) and considering a bin size of 5 km for temperature and salinity. Grey lines represent four Gaussian functions with standard deviations of 15, 20, 25, and 30 km.

Empirical correlation in the Atlantic

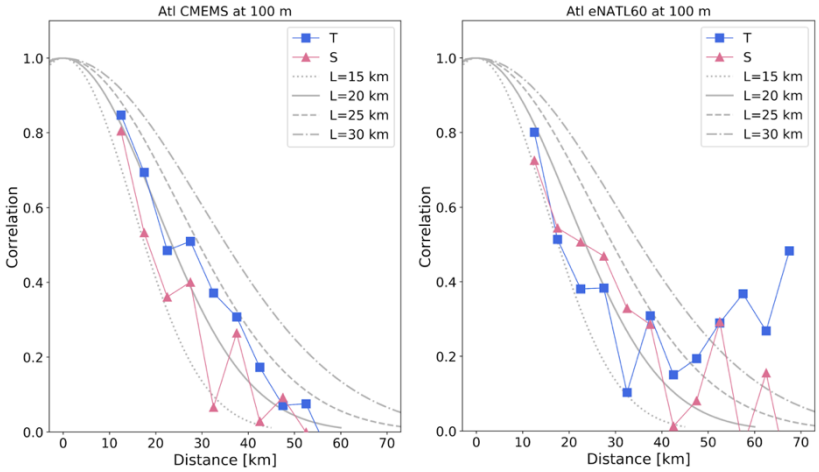

Figure 33: Empirical correlation calculated from the reference configuration pseudo-observations at 100 m depth for each model (CMEMS, eNATL60). Correlation between data pairs that are separated by a defined distance (x-axis) and considering a bin size of 5 km for temperature and salinity. Grey lines represent four Gaussian functions with standard deviations of 15, 20, 25, and 30 km. Considering all models, the Gaussian function that resembles better the empirical correlations is the Gaussian with a standard deviation of 20 km, different than in the Mediterranean.

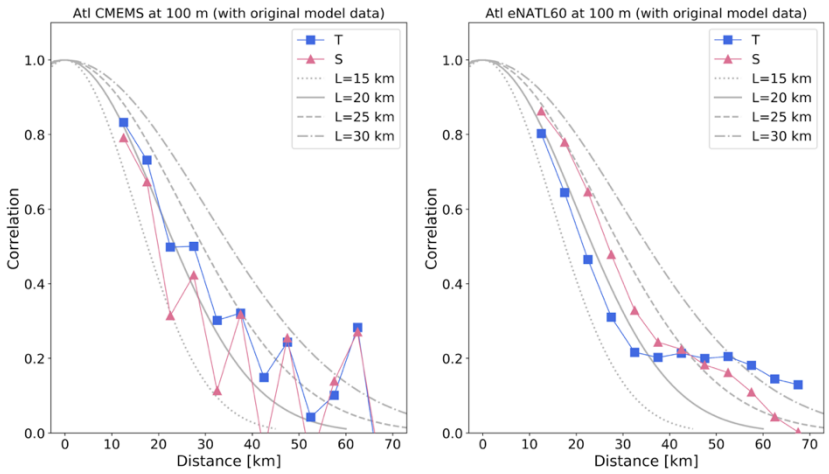

Figure 34: Empirical correlation calculated from the original model data averaged for the period of the configuration and including all data inside the domain of the configuration. Correlation between data pairs that are separated by a defined distance (x-axis) and considering a bin size of 5 km for temperature and salinity. Grey lines represent four Gaussian functions with standard deviations of 15, 20, 25, and 30 km. Considering all models, the Gaussian function that resembles better the empirical correlations is the Gaussian with a standard deviation of 20 km, different than in the Mediterranean.

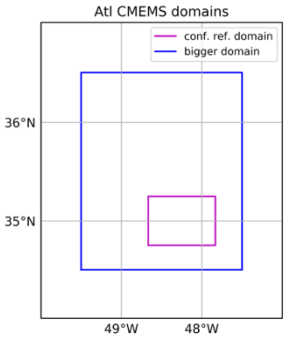

Figure 35: Map in the Atlantic with the reference configuration domain (magenta box) and the bigger domain (blue box).

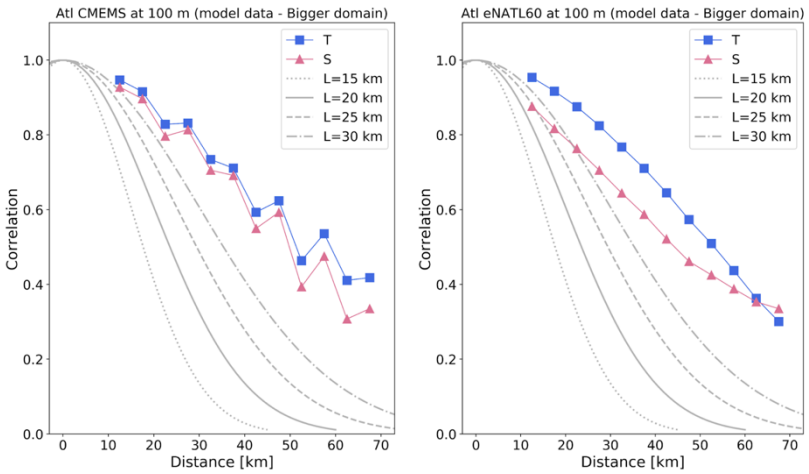

Figure 36: Empirical correlation calculated from the original model data averaged for the period of the reference configuration and including all data inside the bigger domain (blue box in the map). Correlation between data pairs that are separated by a defined distance (x-axis) and considering a bin size of 5 km for temperature and salinity. Grey lines represent four Gaussian functions with standard deviations of 15, 20, 25, and 30 km. The empirical correlation depends on the size of the domain (see Figure 34 for the results in the reference domain (magenta box in the map)).

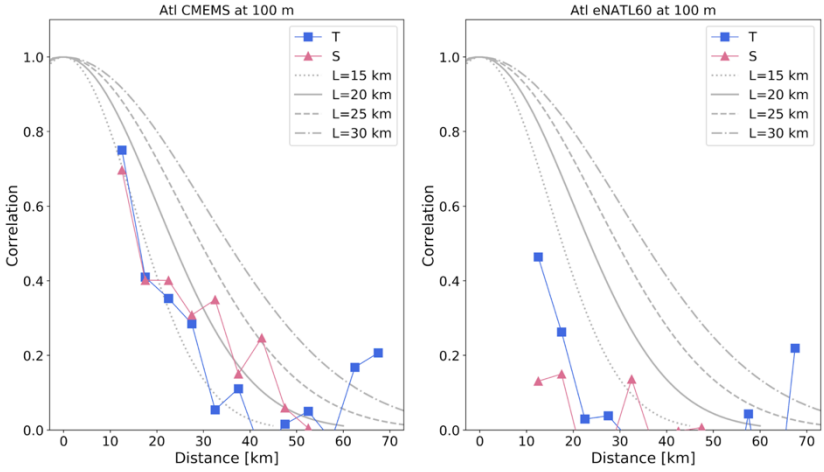

Figure 37: Empirical correlation calculated from the configuration #4 (as the reference configuration but in January) pseudo-observations at 100 m depth for each model (CMEMS, eNATL60). Correlation between data pairs that are separated by a defined distance (x-axis) and considering a bin size of 5 km for temperature and salinity. Grey lines represent four Gaussian functions with standard deviations of 15, 20, 25, and 30 km.

Spatio-temporal optimal interpolation

The spatial optimal interpolation used to reconstruct in situ observations in field experiments only considers the spatial variability of the measurements and assumes quasi-synopticity at the scales resolved by the sampling (e.g., Rudnick, 1996; Pascual et al., 2004; Barceló-Llull et al., 2017, 2021; Ruiz et al., 2019). However, if the structures evolve during the sampling period, the reconstruction of the observations may introduce errors due to the lack of synopticity. For this analysis, we use an advanced version of the optimal interpolation that considers the spatio-temporal variability and correlation scale of the observations and from which the resulting map represents a specific date of the sampling period. This method is applied to reconstruct

altimetry observations (e.g. Escudier et al., 2013) and it includes the time coordinate of each observation and the temporal correlation scale in the correlation function of the optimal interpolation. This function is used to compute correlations between observational points to determine the weights for the data interpolation. Then, to compute the correlation between grid and observational points, we use the same correlation function assuming that the interpolation maps the observations on the central date of the sampling (Table 4). To determine the appropriate temporal correlation scale, we performed an extensive analysis summarized in the next subsection.

We applied the spatio-temporal optimal interpolation to reconstruct all configurations simulated in both regions from all models. Temperature and salinity pseudo-observations were interpolated onto a regular 3D grid using (i) linear interpolation to interpolate vertically each profile with a vertical spacing of 5 m and (ii) spatio-temporal optimal interpolation to interpolate horizontally onto a grid with a spatial resolution of 2 km. We used spatial correlation scales of 20 km (~scales resolved by SWOT, Barceló-Llull et al., 2021) and a temporal correlation scale of 10 days. The new grid was defined for each configuration by the (longitude, latitude) limits of the original CTD grid and considering a horizontal resolution of 2 km. The mean fields were assumed to be planar and the uncorrelated noise for the interpolation of temperature and salinity was assumed to be 3% of the signal energy (Barceló-Llull et al., 2021). The interpolation was done on the central date of the sampling, which is different for each configuration (See Table 4).

Table 4. Reconstruction date for each configuration in each region.

Configuration	Region	Reconstruction date
Reference	Mediterranean	2009-09-03 03:00
	Atlantic	2009-09-03 03:00
1	Mediterranean	2009-09-02 12:00
	Atlantic	2009-09-02 12:00
2a	Mediterranean	2009-09-02 18:00
	Atlantic	2009-09-02 18:00
2b	Mediterranean	2009-09-03 00:00
	Atlantic	2009-09-03 00:00
2c	Mediterranean	2009-09-02 12:00
	Atlantic	2009-09-03 09:00
2d	Mediterranean	2009-09-02 06:00
	Atlantic	2009-09-03 15:00
3a	Mediterranean	2009-09-01 21:00
	Atlantic	2009-09-01 21:00
3b	Mediterranean	2009-09-01 21:00
	Atlantic	2009-09-01 21:00
4	Mediterranean	2010-01-03 03:00
	Atlantic	2010-01-03 03:00
5	Mediterranean	2009-09-02 19:30
	Atlantic	2009-09-02 19:30

With the reconstructed T and S 3D fields, we computed the dynamic height (DH) and the corresponding geostrophic velocity (ugeo, vgeo) at the ocean upper layer (5 m for the configurations with CTD/uCTD, 30 m for the glider configuration), following the same procedure that will be applied to validate SWOT with real observations during the fast-sampling phase (Barceló-Llull et al., 2021).

The reconstructed DH is compared to the model SSH on the interpolation date (ocean truth). The comparison is done in the same domain for all configurations (domain of configuration 2a), to avoid sensitivity of the results to the domain size. The spatial mean of DH and SSH over this domain was subtracted to the corresponding fields to compare anomalies. Model fields were linearly interpolated to the date and grid of the reconstruction. In the same way, the reconstructed geostrophic velocity magnitude is compared to the horizontal velocity magnitude from the model on the interpolation date (ocean truth). Both comparisons are done through the RMSE-based score (RMSEs), a metric used in the ocean data challenge[8].

Temporal correlation scale analysis

We performed an extensive analysis to find the temporal correlation scale for the spatio-temporal optimal interpolation. After testing different methods without finding the expected results, we concluded that the analysis of the spatial and temporal correlation scales cannot be done separately, as both parameters work together in the optimal interpolation algorithm. We finally made a cross-validation to find the best combination.

Previous tests

Previously we performed the following tests:

(i) Calculate spatial and temporal empirical correlations separately from pseudo-observations. We observed a contamination of the spatial correlation in the temporal correlation, not observed otherwise. This may indicate a dominance of the spatial correlation over the temporal correlation (Figure 38). However, with this approach we were mixing both scales: we were evaluating different correlation functions from pseudo-observations sampled at different locations and times.

(ii) Calculate spatial and temporal correlation functions separately from model outputs. This approach was aimed to solve the issue of the pseudo-observations mixing temporal and spatial variability. It consists of:

- Calculate the spatial correlation function (Ls) including all model data within the sampling domain at each time step during the sampling period, and adjust the correlation function to a Gaussian (we use scipy.optimize.curve_fit in Python) to obtain its standard deviation, which is the spatial correlation scale. Average the Ls values obtained for each time step.

- Calculate Lt in each grid point during a time window defined by the sampling period: in one grid point extract T and S values during the time window and calculate the corresponding temporal correlation function (bin size = 0.125 days = 3 h; bin array from 0.0625 days = 1.5 h). Adjust a Gaussian function and obtain the standard deviation, which corresponds to the temporal correlation scale. The analysis was done for all grid points within the sampling domain.

[8] https://github.com/ocean-data-challenges/2020a_SSH_mapping_NATL60/blob/master/notebooks/example_data_eval.ipynb

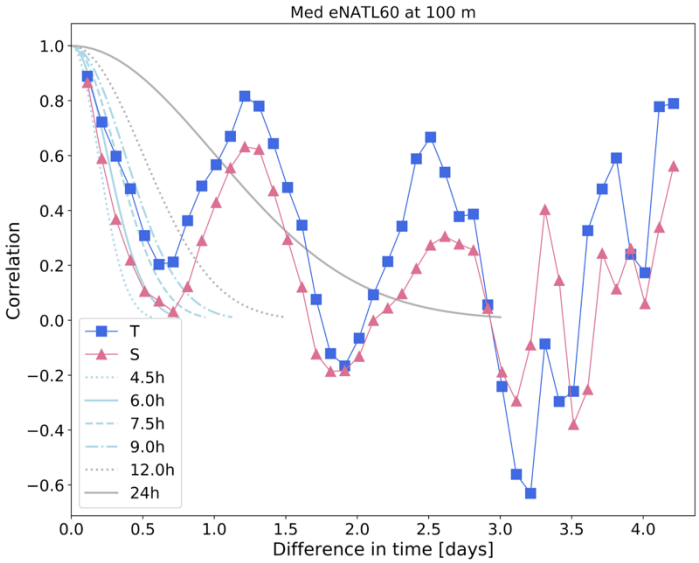

Figure 38: Empirical temporal correlation in the Mediterranean from T and S pseudo-obs at 100 m depth generated from eNATL60. The spatial correlation dominates the temporal correlation of the pseudo-observations sampled in different location and times.

We obtained the following results for Ls:

- Domain and period of the reference configuration in the Mediterranean (from 2009-09-01 00:00 to 2009-09-05 07:30). T and S data from eNATL60 at 100 m depth. Bin size: 5 km; bin array from 10 to 70 km. To have a better fit with a Gaussian, we adjust the correlation function while it goes from 1 to 0.
    - L spatial from T model data: 24.24 ± 2.16 km
    - L spatial from S model data: 21.90 ± 0.45 km
- Domain and period of the configuration 4 in the Med (from 2010-01-01 00:00 to 2010-01-05 07:30). T and S data from eNATL60 at 100 m depth. Bin size: 5 km; Bin array from 10 to 70 km. To have a better fit with a Gaussian, we adjust the correlation function while it goes from 1 to 0.
    - L spatial from T model data: 16.95 ± 1.66 km
    - L spatial from S model data: 13.79 ± 1.53 km

  The results for Lt were very different between different location within the domain (Figure 39). To improve the results, we smoothed the model data before calculating Lt so that only scales higher than Ls (~15km) were considered. The maps still showed high variability of Lt.

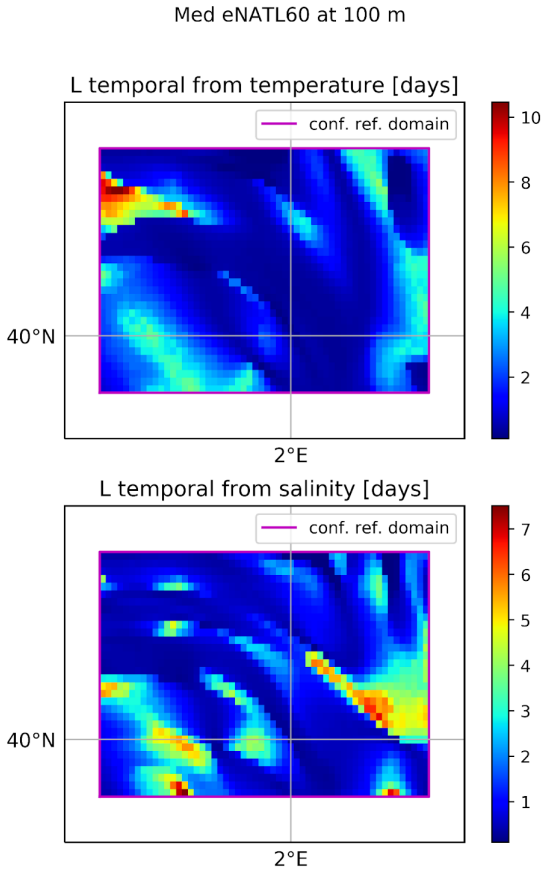

Figure 39: Map with the temporal correlation scale obtained in each grid point within the sampling domain during the sampling period (reference configuration), from temperature and salinity model data, respectively. To have a better fit with a Gaussian, we adjust the correlation function while it goes from 1 to 0. High Lt means higher correlation of the data at this location during a longer period.

(iii) Calculate the temporal correlation scale from SSH in the western Mediterranean.

- **No filtering the original SSH**

We calculated the temporal correlation of SSH from eNATL60 for the period of the reference configuration and for the whole western Mediterranean. The methodology consists of computing the correlation function at each grid point considering data during the period of the reference configuration. We computed the correlation coefficient of those data pairs separated by a distance in time of 3 hours. Bin size: 2*0.0625 days = 3 hours; bin array from 0.0625 days = 1.5h (time between CTD stations) to 4.3125 days (sampling duration). We fitted a Gaussian function to the full correlation function (without removing the values < 0). With this we obtained the Lt value at each grid point (the std of the Gaussian function that fits best the correlation function). We also calculated the RMSE of the fit (correlation function vs. Gaussian function) considering the data where the Gaussian function > 0.01. We called this metric: RMSEv.

Lt has low values (< 1 day) in almost the whole domain (Figure 40), including the Alboran Sea, in which the Alboran gyre is present during long periods of time and, hence, we expect high temporal correlation

scales. The question that came from this analysis is why we obtain small values of Lt. The fit of the correlation functions was correct and we tried to improve the methodology.

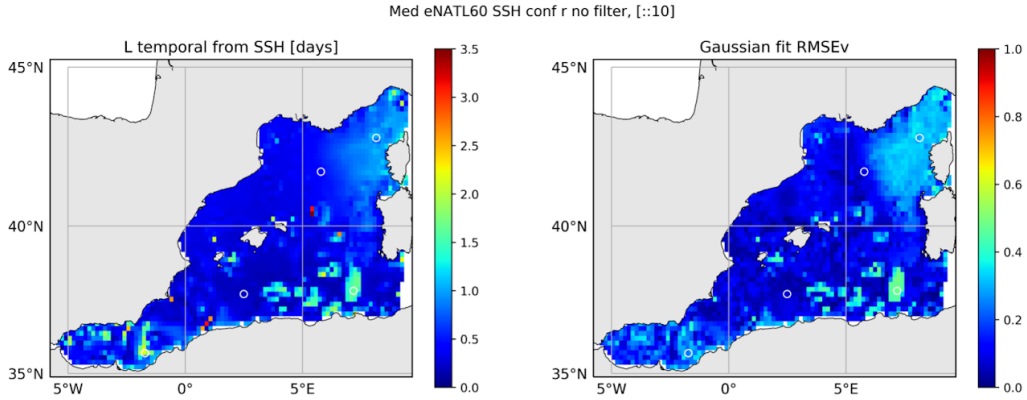

Figure 40: (left) Map of Lt computed from eNATL60 SSH outputs (subsampled: 1 out of 10 data points) for the reference configuration time period. (right) RMSE of the Gaussian fit considering the data where the Gaussian function > 0.01.

- **2D Gaussian filter to SSH fields to keep spatial scales > 20 km**

We applied a 2D Gaussian filter to SSH fields in order to keep spatial scales larger than 20 km, and then we repeated the analysis. For the reference configuration period (summer) we obtained the same Lt values as with no filtering, but without the small-scale patterns with higher Lt observed in Figure 40. We did the same analysis for the configuration #4 (winter) without finding differences with respect to the original fields (no filtering). The obtained Lt values were too small in summer and also in winter. One reason may be the contamination of model outputs by high-frequency variability (Ciani et al., 2021; see Section 6.5). To explore this issue, we filtered the large spatial scales (scales responsible for the high-frequency variability) and we repeated the analysis.

- **Remove spatial mean of SSH and apply 2D Gaussian filter to keep spatial scales > 20 km**

Instead of filtering the large spatial scales (computationally expensive) we removed the spatial mean of SSH at each time step. The spatial scales responsible of introducing high temporal variability in eNATL60 outputs are of the order of 600 km (Ciani et al., 2021; see Section 6.5), and in the Mediterranean a Gaussian filter with this scale is similar to remove the spatial mean. We repeated the analysis of Lt removing first the spatial mean of SSH at each time step and then applying the Gaussian filter with L=30 km (20 km wavelength). We still obtained too low values of Lt (Figure 41).

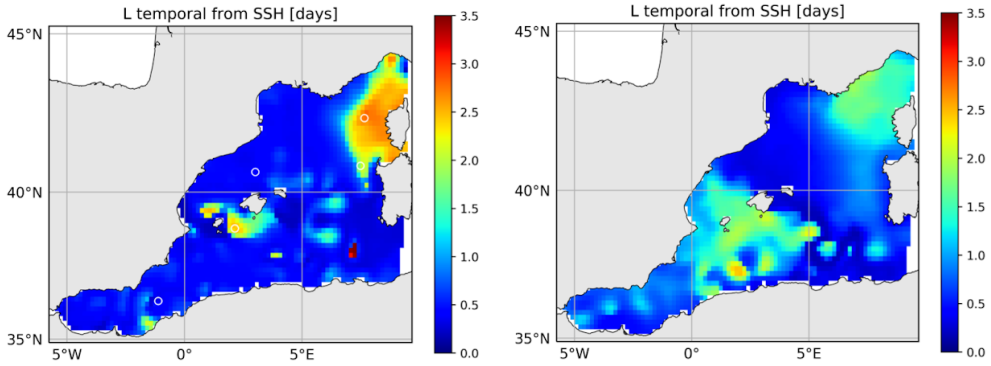

Figure 41: Maps of Lt computed from eNATL60 SSH outputs (subsampled: 1 out of 10 data points) for the (left) reference configuration and (right) configuration #4 time periods. The spatial mean of SSH was removed at each time step and a Gaussian filter was applied to the residuals to keep spatial scales > 20 km.

- **Conclusion**

The correlation function depends on the coherence of the signal. If the signal has coherence during the time window, the Lt will be high. If the signal has high variability during the time window, and low coherence, then Lt is small. From the example in Figure 42 and the evolution of SSH maps (not shown), we observed that even if the correlation is calculated inside a gyre, where we expect high Lt values, the calculated Lt is small. We repeated the analysis using a longer time window of 20 days without improving the results. We concluded that this analysis could not provide the results we expected and that a cross-validation was needed.

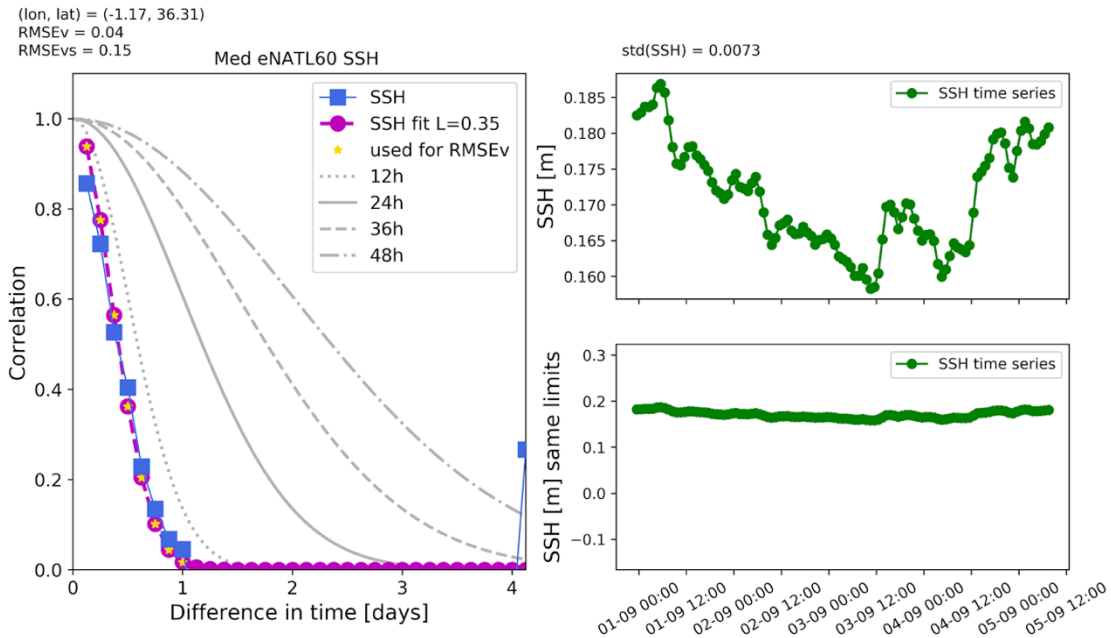

Figure 42: (left) Correlation function calculated from SSH (blue squares) at (lon, lat) = (1.17ºW, 36.31ºN) (western white circle in Figure 41) and Gaussian fit with Lt=0.35 days (magenta dots). (top right) Temporal series of SSH during the time window used to compute Lt. (bottom right) Same as previous figure with different limits.

(iv) Calculate the 2D correlation from pseudo-observations (Figure 3.2 in Rudnick et al., 2017). The methodology consists of computing the correlation coefficient of those pseudo-observations separated by a distance di (di=10, 20, 30, … km) and time ti (bins start with t0 = 0.0625 days = 1.5h (time between CTD stations) and we use a bin size of 3*0.0625 days = 4.5 hours), and map the resulting 2D correlations. We used the original T and S pseudo-observations at 100 m depth for the reference configuration in the Mediterranean simulated from eNATL60. The resulting 2D correlations maps are shown in Figure 43. To have complete maps without gaps, we applied the same analysis to model data (next section).

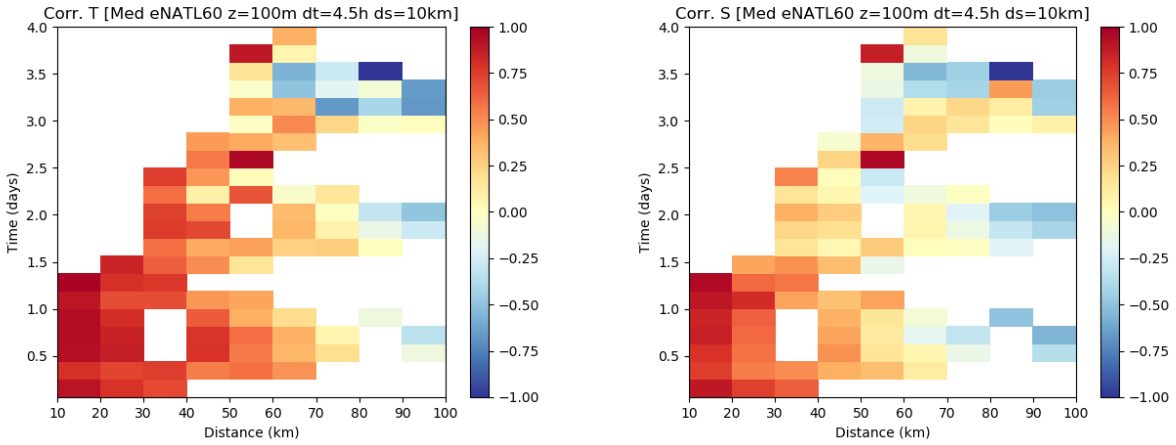

Figure 43: 2D correlation maps from T and S pseudo-observations at 100 m depth for the reference configuration in the Mediterranean simulated from eNATL60.

(v) Calculate the 2D correlation from model data (Figure 3.2 in Rudnick et al., 2017). The methodology consists of computing the correlation coefficient between data pairs separated by a distance di (di=10, 20, 30, … km) and time ti (bins start with t0 = 0.0625 days = 1.5h (time between CTD stations) and we use a bin size of 3*0.0625 days = 4.5 hours), and map the resulting 2D correlations. We used hourly eNATL60 model outputs within the reference configuration domain and sampling period (in the Mediterranean and at 100 m depth), but only considering 1 data point out of 3 in time, latitude and longitude (to save computing time). With model data, the 2D correlation maps (Figure 44) reveal a dominance of the spatial scales over the temporal scales. Within the same distance bin, the correlation slightly decreases when increasing time, but the biggest difference is between distance bins. However, the methodology to fit a 2D Gaussian to these maps is not clear and we decided to do the cross-validation analysis.

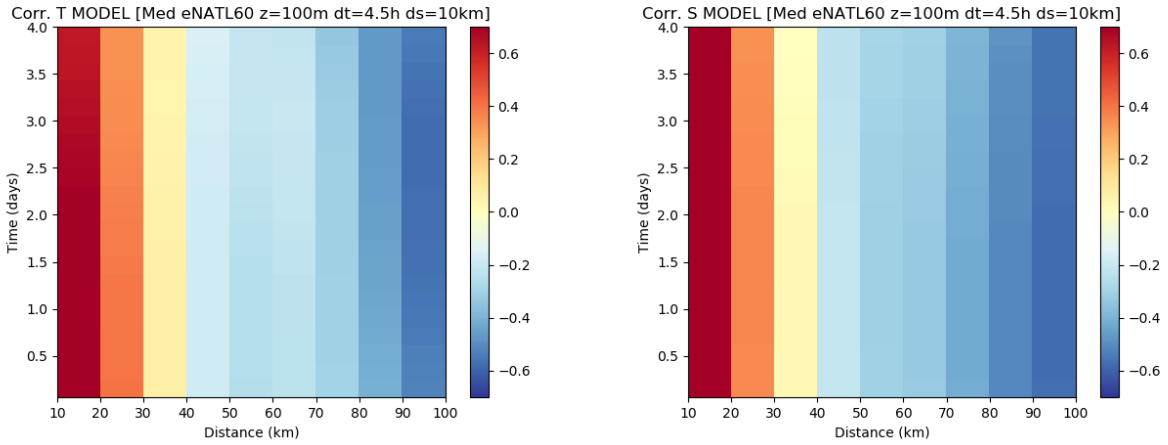

Figure 44: 2D correlation maps from T and S eNATL60 model data within the domain and sampling period of the reference configuration in the Mediterranean at 100 m depth.

Cross-validation in the Mediterranean

After ending the analysis of Lt without obtaining the expected result, we concluded that the analysis that could evaluate the best combination of parameters (Ls, Lt) for the spatio-temporal optimal interpolation (OI) was a cross-validation. The goal was to find the combination that provides the reconstruction more similar to the ocean truth. This analysis was done in the Mediterranean and for the reference configuration, and then extended to every week during 1 year. We generated pseudo-observations of SSH (instead of T and S) to apply the optimal interpolation only to one depth layer and save computational time. To simulate the observations, eNATL60 SSH data were linearly interpolated to the coordinates and time of each CTD profile of the reference configuration. Before, (i) we interpolated the original SSH field from eNATL60 outputs to a regular grid with a horizontal spacing of 1/60º and, (ii) the spatial mean of SSH computed over the western Mediterranean domain was subtracted to the SSH field in each time step to remove the high-frequency variability (Ciani et al., 2021; see Section 6.5) (Figures 45 and 46). SSH pseudo-observations were considered perfect, i.e., we did not simulate measurement error (Le Guillou et al., 2021 and ocean data challenge[9]).

[9] https://github.com/ocean-data-challenges/2020a_SSH_mapping_NATL60

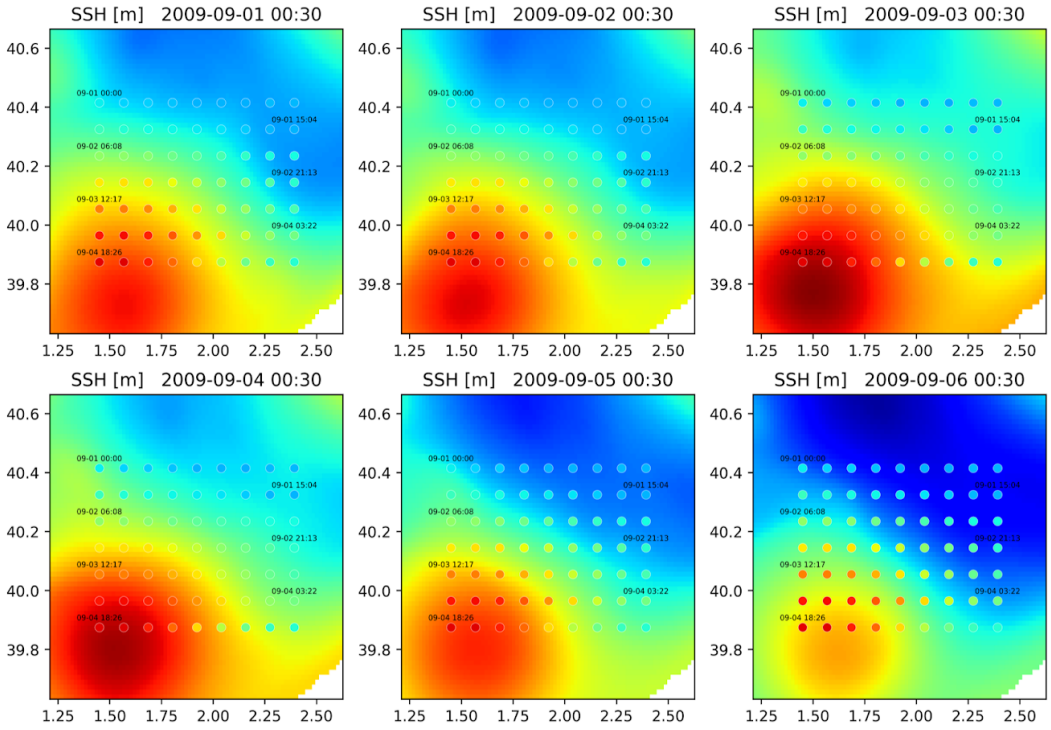

Figure 45: (dots) Pseudo-observations of SSH simulated from the eNATL60 model data including the high-frequency variability (see Section 6.5). The background is the eNATL60 SSH data in different dates during the sampling period. During 6 days we can observe the evolution of the high-frequency variability in the reference configuration domain.

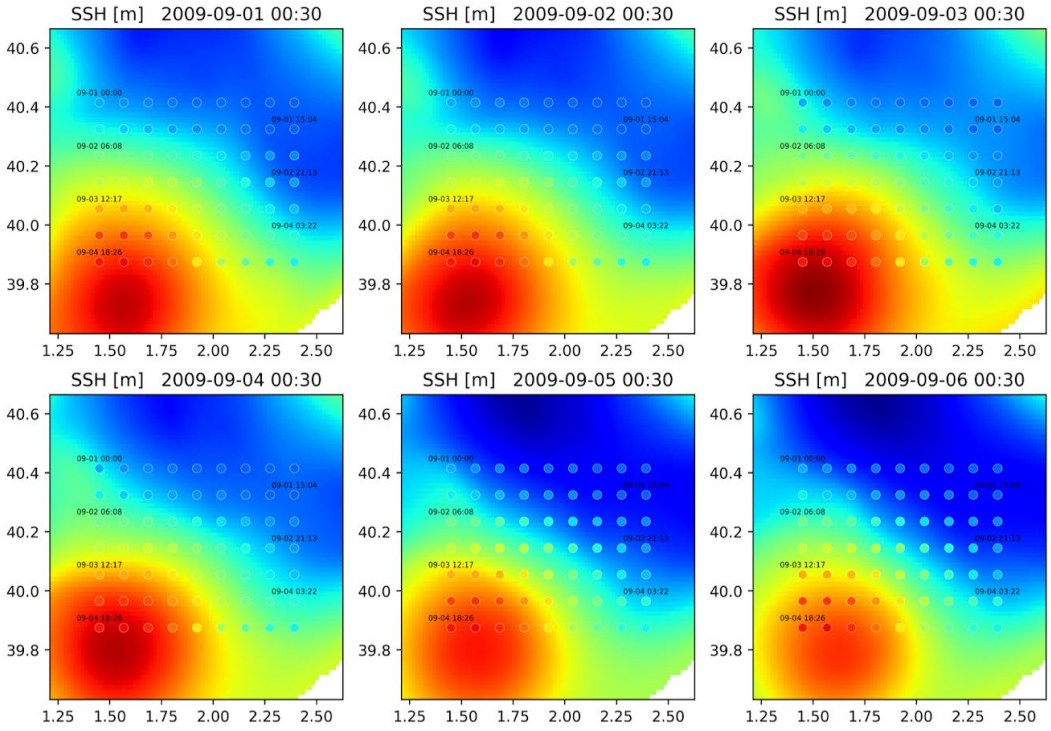

Figure 46: (dots) Pseudo-observations of SSH simulated from the eNATL60 SSH field after removing the spatial mean in each time step. The background is the eNATL60 SSH field without the spatial mean in different dates during the sampling period.

As a first cross-validation test, the pseudo-observations of SSH were reconstructed with the spatio-temporal OI applying different values of noise-to-signal error, Ls and Lt. The reconstructed fields were then linearly interpolated to the ocean truth grid. For the comparison between reconstructed and ocean truth SSH we calculated the RMSE-based score (RMSEs) over the domain, a metric used in the ocean data challenge[10]. A RMSEs of 1 means perfect reconstruction, while a RMSEs of 0 means bad reconstruction.

$$\text{RMSE-based score} = 1 - [\text{RMS}(\text{SSHrec} - \text{SSHtruth})/\text{RMS}(\text{SSHtruth})]$$

Values tested:

- Ls = [10, 12, 14, 16, 18, 20, 22, 24, 26, 28] km
- Lt = [1, 2, 3, 4, 5, 6, 7, 8, 9, 10] days
- errors = [0.05%, 0.3%, 1%, 3%]

The cross-validation was first done for the reference configuration period (reconstruction date: 2009-09-03 03:30). We found small differences in the RMSEs between the best and worst reconstructions [~0.9 vs. ~0.7]. This suggests that the spatio-temporal OI works well with different combinations of parameters, and that we need to do the analysis for 1 year as different structures may lead to different statistics.

The cross-validation was then done every 7 days for 1 year. The configuration of the simulated observations (longitude and latitude of each observation) was the same as the reference configuration, but the date of each observation was changed to start a new sampling every 7 days during 1 year. The first configuration started on 02-07-2009 and a new configuration started every 7 days afterwards. We simulated a total of 52 configurations during the 1-year period. The configuration (or sampling) duration is 4.33 days (4 days, 7 h and 50 min). The first configuration goes from 2009-07-02 00:00 to 2009-07-06 07:50, and the last configuration from 2010-06-24 00:00 to 2010-06-28 07:50. Note that the model data is available from 2009-07-01 00:30 to 2010-06-30 23:30. The reconstruction date was defined as the central date of each configuration minus 15 minutes to have the same time as the model outputs (hh:30) and avoid temporal interpolation. For instance, for the first configuration the reconstruction time is 2009-07-04 03:30.

Table 5. Combination of spatial (Lx in the table) and temporal (Lt) correlation scales that provides the reconstruction of SSH with the highest RMSE-based score for each noise-to-signal error variance and configuration (identified by the reconstruction date).

Date	error = 0.05%	error = 0.3%	error = 1%	error = 3%
2009-07-04 03:30	Lx=10km Lt=07days	Lx=10km Lt=07days	Lx=12km Lt=10days	Lx=12km Lt=10days
2009-07-11 03:30	Lx=28km Lt=10days	Lx=28km Lt=09days	Lx=28km Lt=04days	Lx=28km Lt=03days
2009-07-18 03:30	Lx=14km Lt=01days	Lx=28km Lt=01days	Lx=26km Lt=01days	Lx=26km Lt=01days
2009-07-25 03:30	Lx=28km Lt=01days	Lx=28km Lt=01days	Lx=28km Lt=01days	Lx=28km Lt=01days
2009-08-01 03:30	Lx=28km Lt=10days	Lx=26km Lt=09days	Lx=24km Lt=01days	Lx=22km Lt=01days
2009-08-08 03:30	Lx=28km Lt=10days	Lx=28km Lt=02days	Lx=28km Lt=02days	Lx=28km Lt=02days
2009-08-15 03:30	Lx=18km Lt=04days	Lx=28km Lt=09days	Lx=26km Lt=06days	Lx=22km Lt=05days
2009-08-22 03:30	Lx=26km Lt=02days	Lx=24km Lt=10days	Lx=26km Lt=08days	Lx=22km Lt=05days
2009-08-29 03:30	Lx=28km Lt=02days	Lx=28km Lt=01days	Lx=28km Lt=02days	Lx=26km Lt=03days
2009-09-05 03:30	Lx=28km Lt=01days	Lx=28km Lt=01days	Lx=28km Lt=02days	Lx=28km Lt=02days
2009-09-12 03:30	Lx=20km Lt=10days	Lx=28km Lt=10days	Lx=24km Lt=05days	Lx=22km Lt=03days
2009-09-19 03:30	Lx=28km Lt=02days	Lx=28km Lt=02days	Lx=28km Lt=02days	Lx=28km Lt=02days
2009-09-26 03:30	Lx=28km Lt=02days	Lx=24km Lt=10days	Lx=24km Lt=08days	Lx=22km Lt=06days

[10] https://github.com/ocean-data-challenges/2020a_SSH_mapping_NATL60/blob/master/notebooks/example_data_eval.ipynb

Date	error = 0.05%	error = 0.3%	error = 1%	error = 3%
2009-10-03 03:30	Lx=14km Lt=01days	Lx=14km Lt=01days	Lx=14km Lt=01days	Lx=14km Lt=01days
2009-10-10 03:30	Lx=28km Lt=02days	Lx=28km Lt=02days	Lx=28km Lt=02days	Lx=28km Lt=02days
2009-10-17 03:30	Lx=14km Lt=01days	Lx=18km Lt=01days	Lx=20km Lt=01days	Lx=20km Lt=01days
2009-10-24 03:30	Lx=10km Lt=02days	Lx=10km Lt=02days	Lx=10km Lt=02days	Lx=10km Lt=02days
2009-10-31 03:30	Lx=28km Lt=01days	Lx=28km Lt=10days	Lx=28km Lt=05days	Lx=28km Lt=03days
2009-11-07 03:30	Lx=26km Lt=02days	Lx=28km Lt=01days	Lx=28km Lt=01days	Lx=28km Lt=01days
2009-11-14 03:30	Lx=18km Lt=01days	Lx=28km Lt=01days	Lx=28km Lt=01days	Lx=28km Lt=01days
2009-11-21 03:30	Lx=10km Lt=02days	Lx=10km Lt=02days	Lx=10km Lt=02days	Lx=10km Lt=02days
2009-11-28 03:30	Lx=22km Lt=01days	Lx=28km Lt=01days	Lx=28km Lt=01days	Lx=28km Lt=01days
2009-12-05 03:30	Lx=28km Lt=02days	Lx=28km Lt=02days	Lx=28km Lt=02days	Lx=28km Lt=02days
2009-12-12 03:30	Lx=14km Lt=08days	Lx=18km Lt=10days	Lx=24km Lt=10days	Lx=20km Lt=07days
2009-12-19 03:30	Lx=28km Lt=10days	Lx=28km Lt=08days	Lx=28km Lt=01days	Lx=28km Lt=03days
2009-12-26 03:30	Lx=20km Lt=02days	Lx=28km Lt=02days	Lx=28km Lt=02days	Lx=26km Lt=02days
2010-01-02 03:30	Lx=24km Lt=02days	Lx=28km Lt=07days	Lx=28km Lt=04days	Lx=28km Lt=02days
2010-01-09 03:30	Lx=24km Lt=02days	Lx=28km Lt=01days	Lx=28km Lt=01days	Lx=28km Lt=01days
2010-01-16 03:30	Lx=12km Lt=01days	Lx=12km Lt=01days	Lx=14km Lt=01days	Lx=16km Lt=01days
2010-01-23 03:30	Lx=26km Lt=10days	Lx=26km Lt=04days	Lx=24km Lt=04days	Lx=22km Lt=05days
2010-01-30 03:30	Lx=12km Lt=02days	Lx=12km Lt=02days	Lx=28km Lt=10days	Lx=28km Lt=07days
2010-02-06 03:30	Lx=10km Lt=01days	Lx=28km Lt=01days	Lx=28km Lt=01days	Lx=28km Lt=01days
2010-02-13 03:30	Lx=10km Lt=02days	Lx=28km Lt=10days	Lx=28km Lt=05days	Lx=28km Lt=03days
2010-02-20 03:30	Lx=12km Lt=01days	Lx=28km Lt=01days	Lx=28km Lt=01days	Lx=28km Lt=01days
2010-02-27 03:30	Lx=10km Lt=01days	Lx=28km Lt=01days	Lx=28km Lt=10days	Lx=28km Lt=10days
2010-03-06 03:30	Lx=20km Lt=01days	Lx=14km Lt=02days	Lx=28km Lt=02days	Lx=28km Lt=02days
2010-03-13 03:30	Lx=14km Lt=06days	Lx=16km Lt=10days	Lx=16km Lt=10days	Lx=16km Lt=10days
2010-03-20 03:30	Lx=28km Lt=07days	Lx=28km Lt=05days	Lx=26km Lt=04days	Lx=24km Lt=03days
2010-03-27 03:30	Lx=20km Lt=04days	Lx=20km Lt=03days	Lx=20km Lt=03days	Lx=18km Lt=03days
2010-04-03 03:30	Lx=28km Lt=10days	Lx=28km Lt=08days	Lx=28km Lt=04days	Lx=28km Lt=02days
2010-04-10 03:30	Lx=16km Lt=01days	Lx=18km Lt=01days	Lx=20km Lt=01days	Lx=18km Lt=05days
2010-04-17 03:30	Lx=14km Lt=10days	Lx=10km Lt=10days	Lx=10km Lt=10days	Lx=10km Lt=10days
2010-04-24 03:30	Lx=20km Lt=10days	Lx=20km Lt=10days	Lx=24km Lt=10days	Lx=20km Lt=06days
2010-05-01 03:30	Lx=28km Lt=01days	Lx=28km Lt=01days	Lx=10km Lt=10days	Lx=28km Lt=10days
2010-05-08 03:30	Lx=28km Lt=04days	Lx=28km Lt=03days	Lx=26km Lt=03days	Lx=22km Lt=03days
2010-05-15 03:30	Lx=28km Lt=05days	Lx=26km Lt=04days	Lx=26km Lt=03days	Lx=26km Lt=03days
2010-05-22 03:30	Lx=22km Lt=10days	Lx=26km Lt=02days	Lx=22km Lt=02days	Lx=24km Lt=03days
2010-05-29 03:30	Lx=16km Lt=10days	Lx=18km Lt=10days	Lx=16km Lt=06days	Lx=28km Lt=09days
2010-06-05 03:30	Lx=18km Lt=10days	Lx=26km Lt=01days	Lx=22km Lt=01days	Lx=20km Lt=01days
2010-06-12 03:30	Lx=20km Lt=10days	Lx=22km Lt=06days	Lx=22km Lt=03days	Lx=24km Lt=02days
2010-06-19 03:30	Lx=28km Lt=10days	Lx=28km Lt=06days	Lx=28km Lt=04days	Lx=28km Lt=03days
2010-06-26 03:30	Lx=16km Lt=09days	Lx=14km Lt=04days	Lx=16km Lt=03days	Lx=16km Lt=03days

The combination of parameters (Ls, Lt) that provides the reconstruction of SSH with the highest RMSEs (named "winner combination") is listed in Table 5 for each noise-to-signal error and configuration. The winner combination is different for each error and configuration because it depends on the features we aim to reconstruct, which are different for each configuration, and because the error we assume also impacts the interpolation. Note that between the winner combination and the other combinations the differences in RMSEs may be small and, hence, the winner combination is not the only good option.

This analysis highlighted the need to fix the noise-to-signal error variance assumed by the interpolation. After reviewing other studies, we fixed a noise-to-signal error variance of 0.3%, the value used in the ocean data

challenge[11], in which they also reconstruct simulated observations of SSH without including measurement errors. We also fixed the spatial correlation scale to focus on SWOT scales of ~20 km (note that in altimetry the spatial and temporal correlation scales applied to map the SSH observations are always the same). A spatial correlation scale of 20 km is a good option considering the sampling resolution of 10 km and the size of the sampling domain (Barceló-Llull et al., 2021), and a good compromise between the different values found in the spatial correlation scale analysis. With these parameters fixed, different values of Lt were tested: 2, 3, 4, 5, 6, 7, 8, 9 and 10 days.

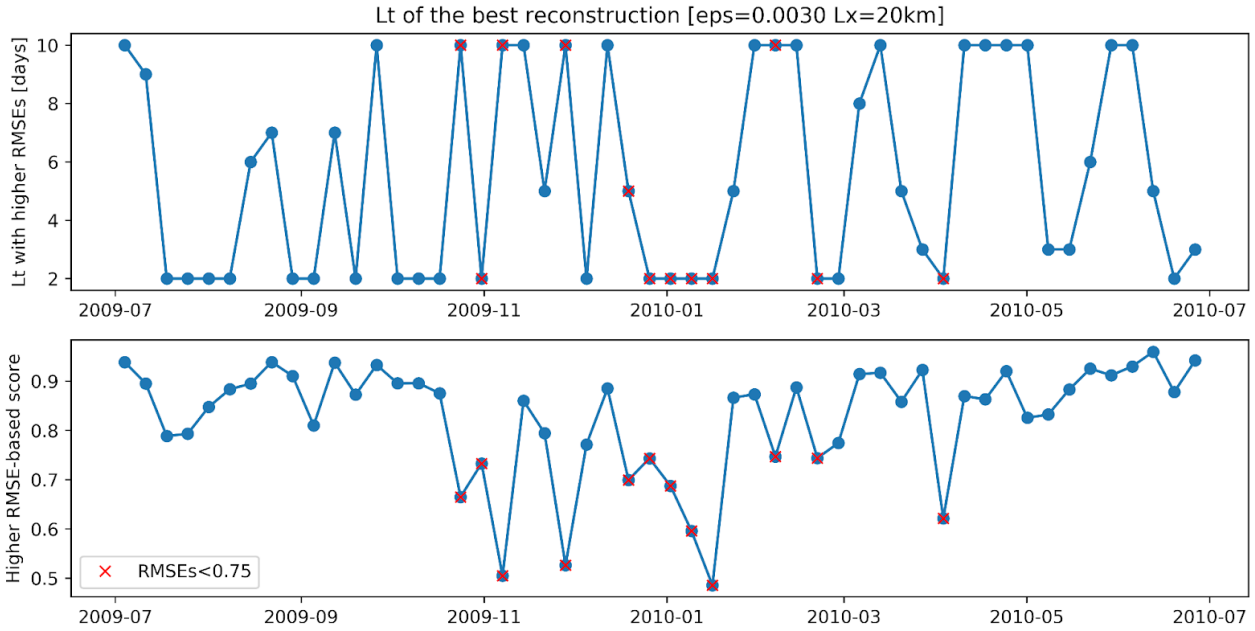

Figure 47: (Top) Temporal correlation scale (Lt) of the best SSH reconstructions made with the spatio-temporal optimal interpolation (noise-to-signal error variance of 0.3% and spatial correlation scale of 20 km). (Bottom) RMSE-based score of the corresponding reconstructions.

Analysing the Lt values of the reconstructions with the highest RMSEs for each date (Figure 47), we observe that in 20 dates Lt = 2 days provides the best reconstructions, while Lt = 10 days gives the best reconstruction on 17 dates. This means that the more extreme values of Lt provide the best reconstructions in different configurations. However, we know from previous analysis that other values of Lt may provide also good results (high RMSEs). For example, for the reference configuration period (applying an error of 0.3% and Ls = 20 km) the reconstruction with the highest RMSEs (0.86) is the one with Lt = 2 days, while Lt = 4 days provides the reconstruction with the lowest RMSEs (0.83). However, in both cases the RMSEs is high (0.86 vs. 0.83) and close to 1 (RMSEs of 1 means perfect reconstruction).

[11] https://github.com/ocean-data-challenges/2020a_SSH_mapping_NATL60/blob/master/notebooks/baseline_oi.ipynb Noise level assumed: 5% in standard deviation (0.05**2 = 0.0025 = 0.25% ~ 0.3% in variance).

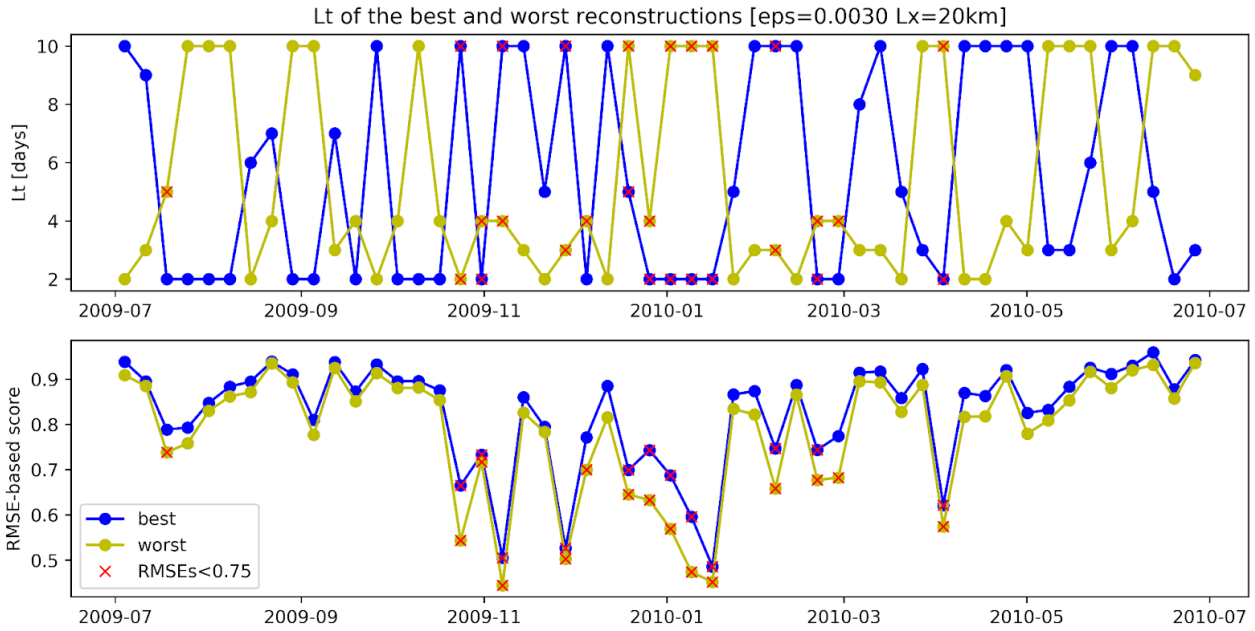

Figure 48: (Top) Temporal correlation scale (Lt) of the best (blue) and worst (yellow) SSH reconstructions made with the spatio-temporal optimal interpolation (noise-to-signal error variance of 0.3% and spatial correlation scale of 20 km). (Bottom) RMSE-based score of the corresponding reconstructions.

Extending this comparison to all configurations (Figure 48), the Lt values which provide the lowest RMSEs are Lt = 2 days in 11 dates, Lt = 10 days in 17 dates and Lt = [3,4] days in 22 dates. Hence, the Lt values of the best and worst reconstructions are highly dependent on the structures/dates. However, the differences in RMSEs between the best and worst reconstructions are small. In most dates (~40) the RMSEs is higher than 0.75 for both reconstructions, which means that all Lt values tested provide good reconstructions, even if they are different between them (Figure 49).

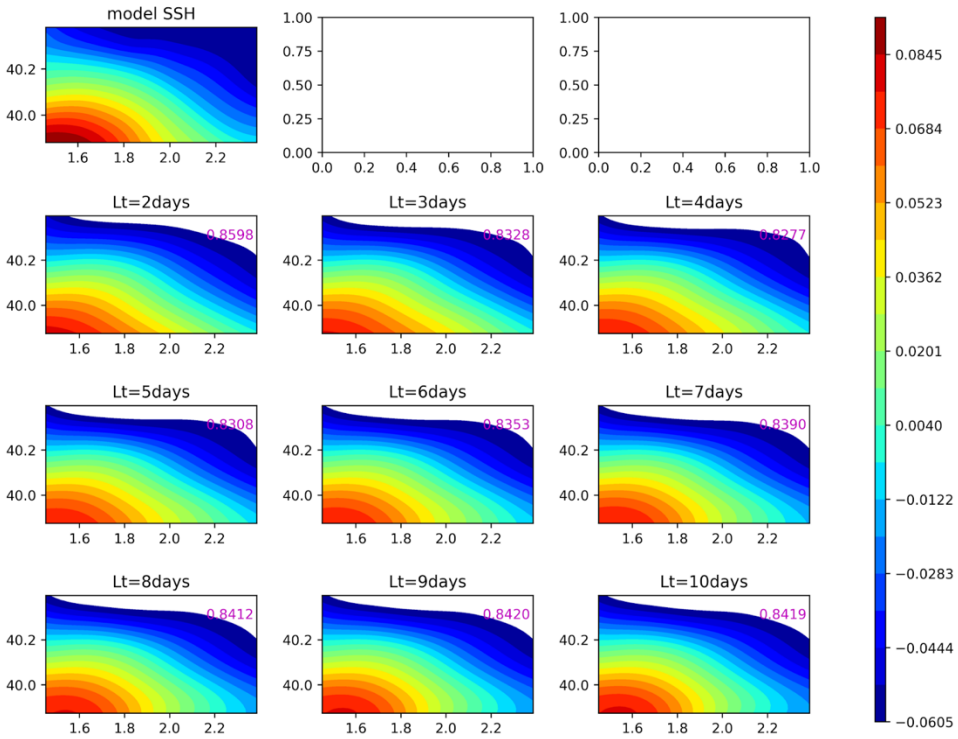

Figure 49: SSH model field (ocean truth) and reconstructed fields for different values of Lt for the reference configuration on 2009-09-03 03:30 (noise-to-signal error variance of 0.3% and spatial correlation scale of 20 km). The reconstruction with the highest RMEs is the one with Lt = 2 days (RMSEs = 0.860), and the second-best reconstruction is the one with Lt = 9 days (0.842). Both reconstructed fields are similar to the model SSH, even if they are different between them.

Fixing the two extreme values of Lt:

- Lt = 10 days: quasi-synoptic observations during the sampling period
- Lt = 2 days: non-synoptic observations during the sampling period,

we evaluate the temporal evolution of the RMSEs of both reconstructions (Figure 50). High values of RMSEs for both reconstructions are observed in most dates: one reconstruction has higher values than the other and vice versa without following a defined pattern. The differences between both reconstructions are overall small, except in some cases in January where the Lt = 2 days reconstruction is better than the one with Lt = 10 days, however the RMSEs values are below 0.75 in both cases (see maps below). The worst reconstruction date is 2010-01-16 03:30; Lt = 2 days provides a RMSEs of 0.49 and Lt = 10 days a RMSEs 0.45. We checked maps of SSH in January and found that they still have high-frequency variability. This is the reason of the low values of RMSEs for the reconstructions performed in January.

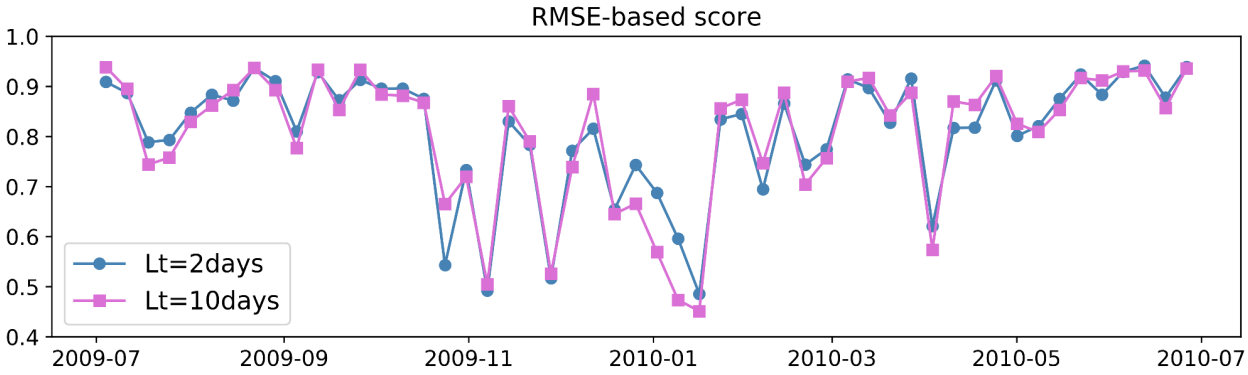

Figure 50: RMSE-based score of the SSH reconstructions made with the spatio-temporal optimal interpolation assuming Lt = 2 days (blue) and Lt = 10 days (magenta) (noise-to-signal error variance of 0.3% and spatial correlation scale of 20 km). Pseudo-observations of SSH generated in the Mediterranean from eNATL60.

The same analysis has been done from SSH pseudo-observations generated from WMOP (Figure 51). High values of RMSEs for both reconstructions are observed in all dates while the differences between both reconstructions are small. The results are consistent with the outcome from the analysis of eNATL60 SSH pseudo-observations.

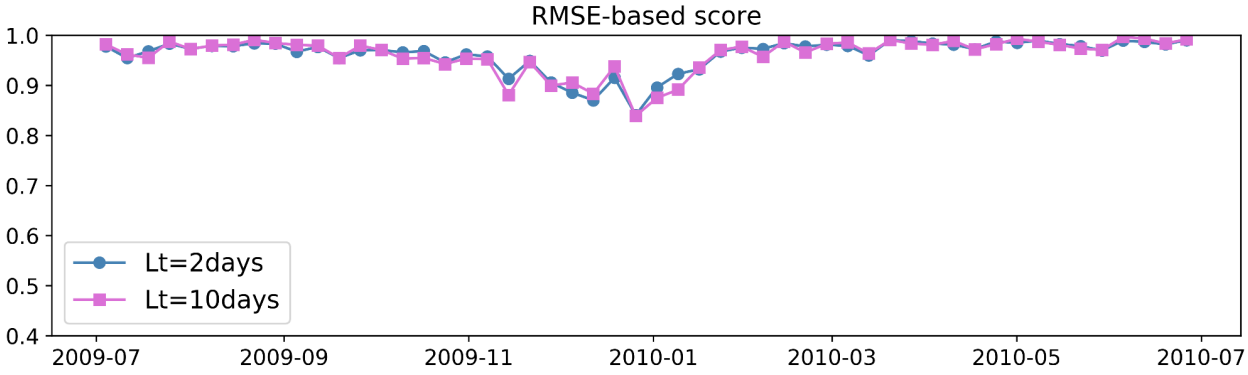

Figure 51: RMSE-based score of the SSH reconstructions made with the spatio-temporal optimal interpolation assuming Lt = 2 days (blue) and Lt = 10 days (magenta) (noise-to-signal error variance of 0.3% and spatial correlation scale of 20 km). Pseudo-observations of SSH generated in the Mediterranean from WMOP.

In the Atlantic, following the same steps, the sensitivity test of SSH pseudo-observations generated from eNATL60 drives to comparable results as the analysis in the Mediterranean (Figure 52). Similar values of RMSEs are obtained for both reconstructions in all the dates analysed; these values are high except in one specific date in March.

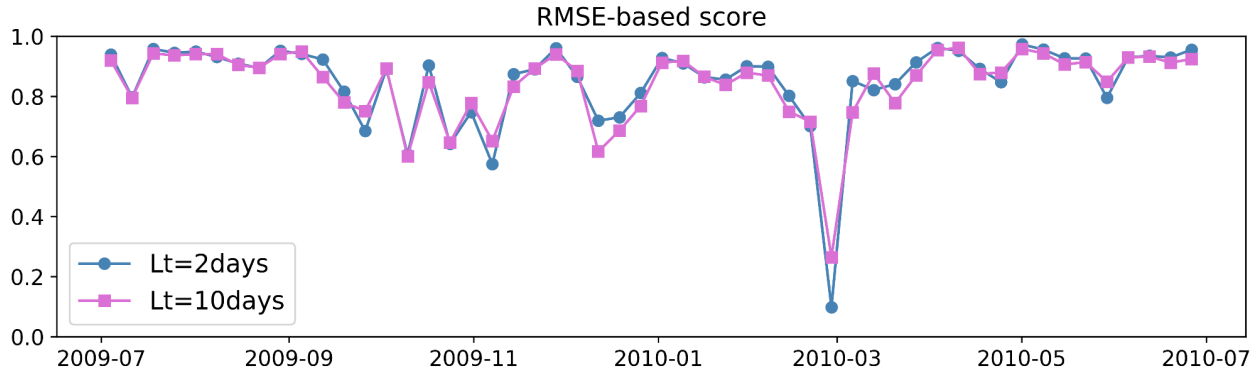

Figure 52: RMSE-based score of the SSH reconstructions made with the spatio-temporal optimal interpolation assuming Lt = 2 days (blue) and Lt = 10 days (magenta) (noise-to-signal error variance of 0.3% and spatial correlation scale of 20 km). Pseudo-observations of SSH generated in the Atlantic from eNATL60.

We conclude that reconstructions done through the spatio-temporal optimal interpolation assuming a temporal correlation scale of 2 days, which means non-synoptic observations during the sampling period, leads to similar RMSE-based scores than assuming Lt = 10 days. Hence, using a temporal correlation scale of 10 days and assuming quasi-synoptic observations is a good option for the interpolation of observations in a sampling strategy similar to the reference configuration. The improvement introduced by assuming a temporal correlation scale of 2 days (non-synoptic observations) is not always translated in better reconstructions.

8.2. Machine-learning

The objective of applying a reconstruction method based on machine learning is to evaluate if it can make accurate predictions from sea surface fields such as salinity and temperature. Deep Learning techniques, with their many connected layers, are useful for the extraction of non-linear chaotic underlying dynamics in nature, specifically at the ocean surface (Sinha et al., 2021; Manucharyan et al. 2021).

In order to overcome the issue of sparse and noisy observations, a variational assimilation framework is used, as it is known for leading to significant improvements in terms of the spatial scales resolved by the interpolation compared to the optimal interpolation and other data-driven schemes (e.g. dinEOF) (Lopez-Radcenco et al., 2018). The variational data assimilation approach along with Deep Learning techniques are merged in the 4D-VarNet model (Fablet et al., 2019; Beauchamp et al., 2020).

4D-VarNet finds the best compromise between a Neural Network-based model propagator and observations to have a reconstructed field of the variables of interest. This is done within a deep learning differentiation scheme, and therefore the amount of data available for the training step is crucial for the performance of this method.

The main challenge here, given the small amount of data obtained from an oceanographic campaign, is to find the optimal neural network architecture to retrieve the dynamics and correlations in the region used for the spatial interpolation.

4D-VarNet model

The model applied to reconstruct the simulated observations is the 4DVarNet model. It is based on the 4D-Var model of data assimilation and a prior state given by Convolutional Neural Networks. 4D-Var is a four-dimensional variational model which generalizes from the 3D-Var model (Carrassi et al., 2018) to take into

account the temporal dimension over an assimilation window (Figure 53). The objective is to find the initial condition such that the difference between observation and reconstruction is minimized within the assimilation window. For each new assimilation window, the observations are assimilated using a segment of the previous prediction. For this analysis we aim to reconstruct surface fields and, hence, the depth component is not taken into account in the model.

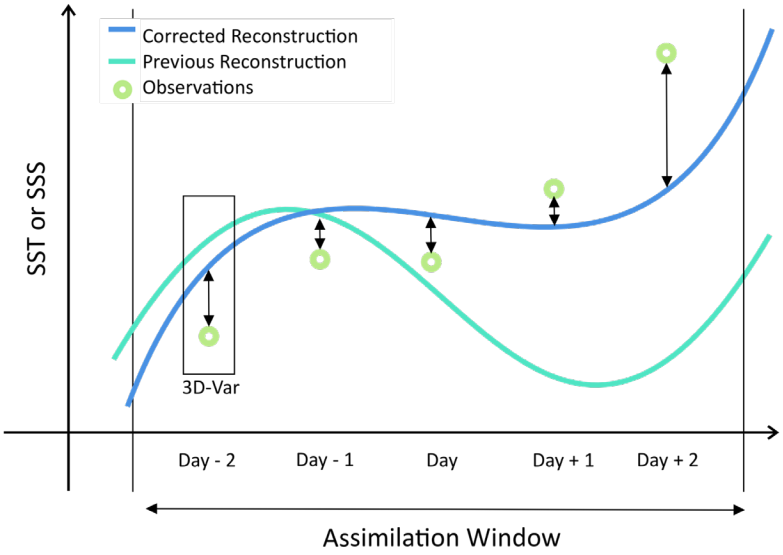

Figure 53: 4D-Var model assimilation scheme.

The objective is to minimize the error between the time-dependent state x, and a dynamical prior $\Phi(x)$,

$$\hat{x} = arg\ min_x ||x - \Phi(x)||$$

$\Phi(x)$ is a trainable plug-and-play prior (Fablet et al, 2021). In this case, due to the small amount of data an auto-encoder architecture is used as prior (Figure 54). A simple Principal Component Analysis (PCA) could also be used, but as the problem comes from geophysical fluid dynamics non-linearities appear and they should be captured.

With the auto-encoder Neural Network architecture the goal is to look for a coordinate transformation of the state u which enables to explain better the underlying dynamics. Then, the objective is to predict accurately how the latent space z evolves. This is done by means of an encoder f, a decoder g, and u which is given by the observations and the lower resolution field (Lusch et al., 2018).

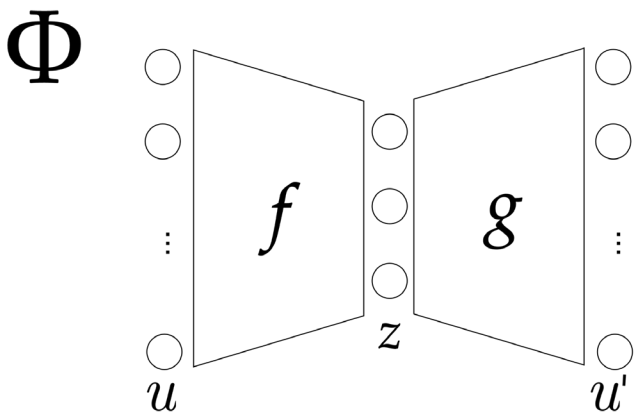

Figure 54: Auto-encoder architecture for the dynamical prior.

The state u is introduced, then the variables of the latent space z are inferred and the decoder will create a prediction field u'. This prediction is then compared with the Ground Truth, and by minimizing the loss function with an iterative process, the variables from the latent space are adjusted.

Note that the dimension of the latent space, as well as the encoder f and decoder g, are to be set up by hand. Here, most of the parameters of the model appear, therefore due to the small amount of data this structure must be kept as simple as possible.

8.3. Model data assimilation

The WMOP Data Assimilation system employs a Multimodel Local Ensemble Optimal Interpolation (EnOI) scheme. It is a widely used method, which represents a good alternative to more complex and computationally expensive methods as EnKF or 4Dvar. It consists in a sequence of analyses (model updates given a set of observations) and model forward simulations.

The Background error covariances are computed from an ensemble of realizations, which are generated from randomly sampling inter-annually a set of different hindcast simulations. Each member could be extracted from any year of the hindcast period within a 90-day time-window centred on the analysis date after removing the seasonal cycle. They reflect the mesoscale variability, representing dynamically consistent covariances between different model variables and depths. The configuration used in this work has been previously employed in several studies in the western Mediterranean Sea (e.g. Pascual et al., 2017; Barceló-Llull et al., 2018; Hernández-Lasheras and Mourre, 2018, Hernández-Lasheras et al., 2021) and in the operational system. More details of the data assimilation procedure can be found in Hernández-Lasheras and Mourre (2018).

8.4. MIOST tool

To map multivariate and multiscale sea level and surface current, we use the Multiscale Inversion for Ocean Surface Topography (MIOST) variational tool to retrieve both geostrophic and ageostrophic currents. This tool has been developed first by Ubelmann et al. (2021) to reconstruct ocean currents combining altimetry and spaceborne doppler data in an observing system simulation experiment as a preparatory work of the ESA SKIM mission (Ardhuin et al. 2019).

The MIOST method is fully described in Ubelmann et al. (2021). MIOST is based on the Optimal Interpolation and in particular the Sherman-Morrison-Woodbury transformation, allowing the inversion in state space and not in the observation space. Working in state space allows the use of a large number of observations (larger than the state grid size). This decomposition is useful to manage multiple signals of various scales in time and/or space (Ubelmann et al. 2021) and allows the decomposition of the signal into representors representing different time and space scales (mesoscale to large-scale) and different physical signals (geostrophy, internal waves, near-inertial oscillations, tropical waves, Ekman component…). It allows thus to go beyond the geostrophic approximation and thus the reconstruction of ageostrophic components of the circulation.

Each sub-component of the system is decomposed on a wavelet basis. The first component is the geostrophic component. This component has a signature on both topography and currents. The time-space wavelet basis is defined along coordinates (longitude, latitude, time) for wavelengths between 80 km and 900 km spanning in all directions of the plane, the time decorrelation scale associated is about 10 days. The second component is the ageostrophic component (decomposed in rotational and divergence parts). This component has a signature only on currents by construction. We choose a decorrelation time scale equal to 2 days and a decorrelation length scale equal to 500 km to mainly reconstruct Ekman currents.

9. Design of in situ sampling strategies to reconstruct fine-scale ocean currents in the context of SWOT satellite validation

9.1. Maps of reconstructed fields in the Mediterranean

Configurations simulated from the CMEMS Mediterranean reanalysis

Reconstructed dynamic height

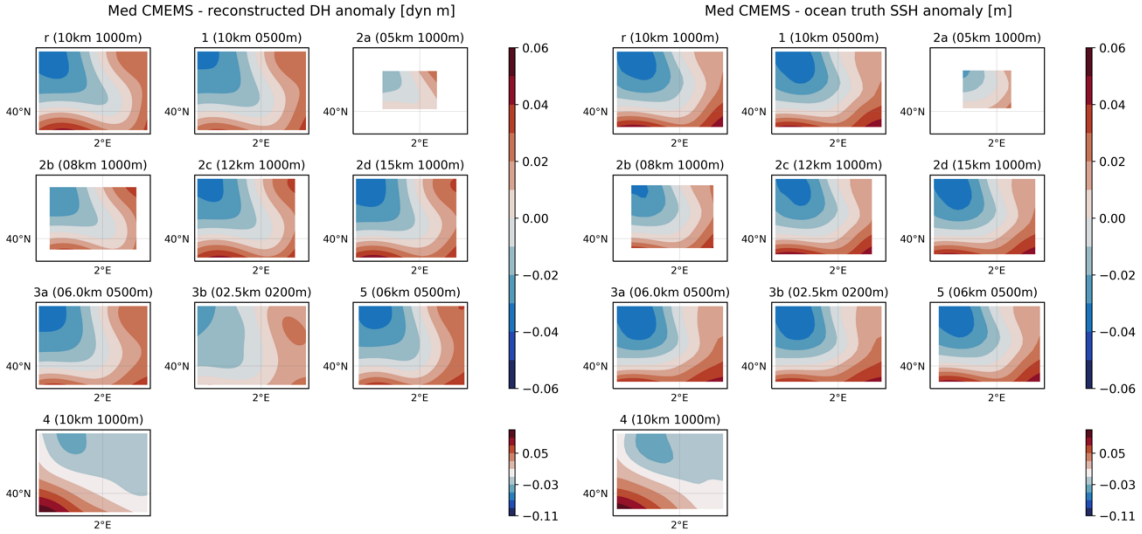

Figure 55: (Left) Dynamic height (DH) anomaly at the upper layer (5 m for all configurations except for configuration 5 (gliders), in which the upper layer is at 30 m) reconstructed from each configuration simulated from the CMEMS Mediterranean reanalysis model. (right) Sea surface height (SSH) anomaly from the CMEMS Mediterranean reanalysis model on the same date as each reconstruction (model fields were linearly interpolated to the date of the corresponding reconstruction (see Table 4)) and within the configuration domain. (all) To compute anomalies, the spatial average over each configuration domain is subtracted to the corresponding field. Note that to calculate statistics model fields are interpolated onto the reconstruction grid and the anomalies are computed within configuration 2a domain for all configurations.

Reconstructed geostrophic velocity magnitude

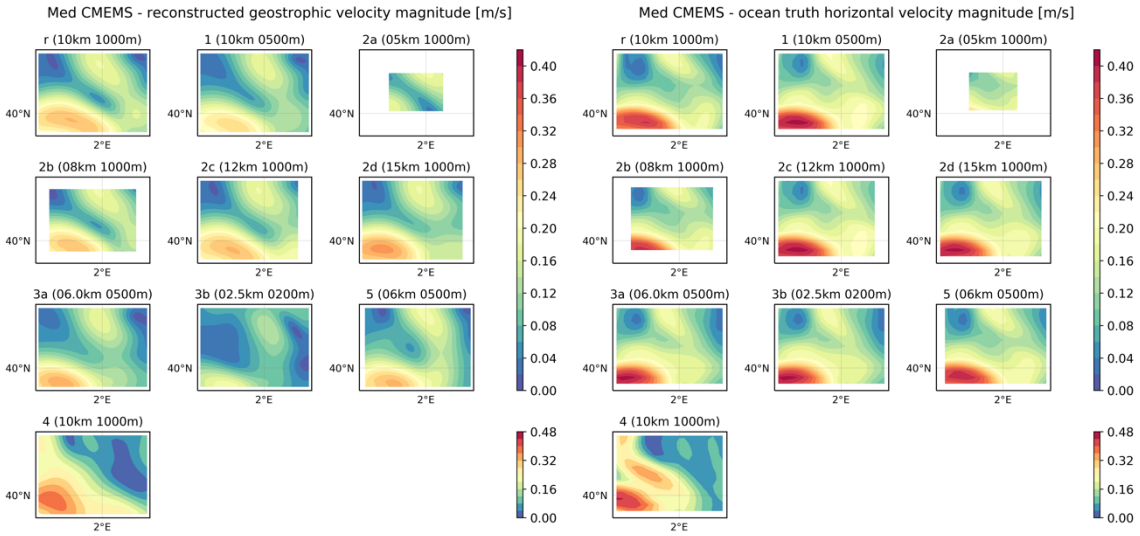

Figure 56: (Left) Geostrophic velocity magnitude at the upper layer (5 m for all configurations except for configuration 5 (gliders), in which the upper layer is at 30 m) reconstructed from each configuration simulated from the CMEMS Mediterranean reanalysis model. (right) Horizontal velocity magnitude from the CMEMS Mediterranean reanalysis model on the same date as each reconstruction (model fields were linearly interpolated to the date of the corresponding reconstruction (see table 4)) and within the configuration domain. Note that to calculate statistics model fields are interpolated onto the reconstruction grid and the statistics are computed within configuration 2a (5 km) domain for all configurations.

Configurations simulated from eNATL60

Reconstructed dynamic height

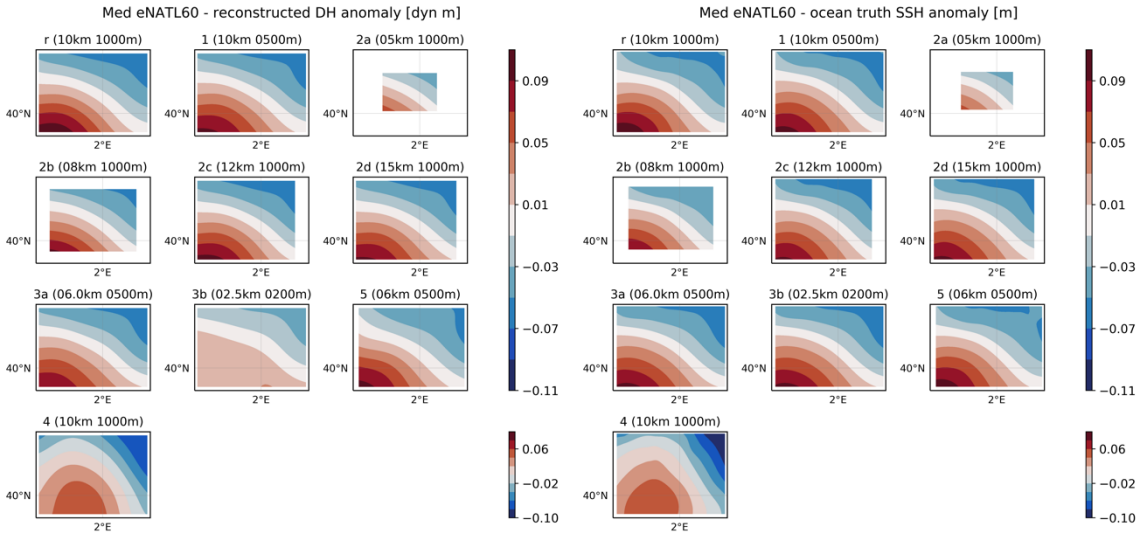

Figure 57: (Left) Dynamic height (DH) anomaly at the upper layer (5 m for all configurations except for configuration 5 (gliders), in which the upper layer is at 30 m) reconstructed from each configuration simulated from eNATL60 in the Mediterranean. (right) Sea surface height (SSH) anomaly from eNATL60 on the same date as each reconstruction (model fields were linearly interpolated to the date of the corresponding reconstruction (see Table 4)) and within the configuration domain. (all) To compute anomalies, the spatial average over each configuration domain is subtracted to the corresponding field. Note that to calculate statistics model fields are interpolated onto the reconstruction grid and the anomalies are computed within configuration 2a (5 km) domain for all configurations.

Reconstructed geostrophic velocity magnitude

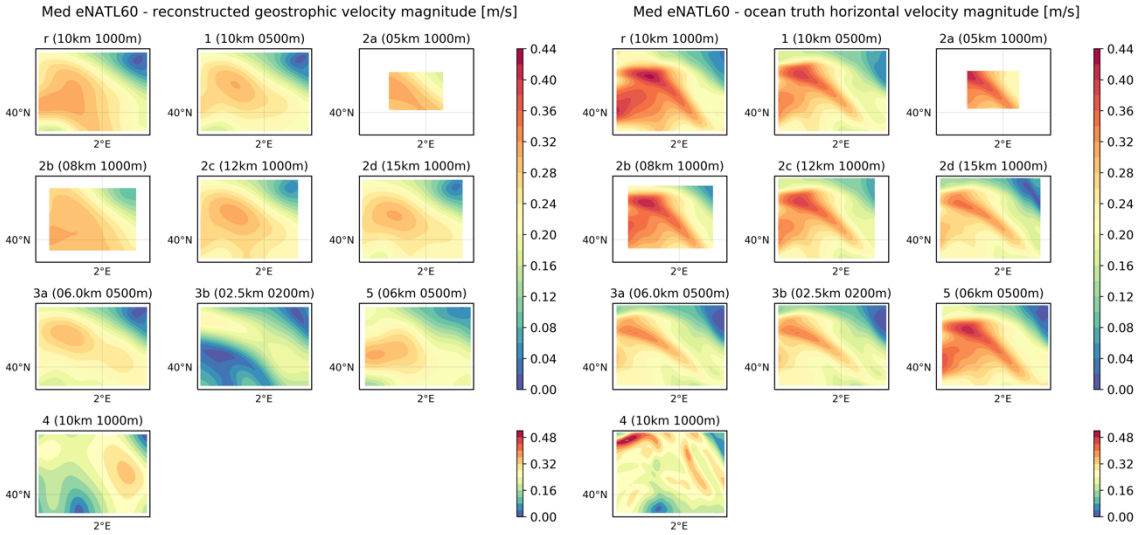

Figure 58: (Left) Geostrophic velocity magnitude at the upper layer (5 m for all configurations except for configuration 5 (gliders), in which the upper layer is at 30 m) reconstructed from each configuration simulated from eNATL60 in the Mediterranean. (right) Horizontal velocity magnitude from eNATL60 on the same date as each reconstruction (model fields were linearly interpolated to the date of the corresponding reconstruction (see table 4)) and within the configuration domain. Note that to calculate statistics model fields are interpolated onto the reconstruction grid and the statistics are computed within configuration 2a (5 km) domain for all configurations.

Configurations simulated from WMOP

Reconstructed dynamic height

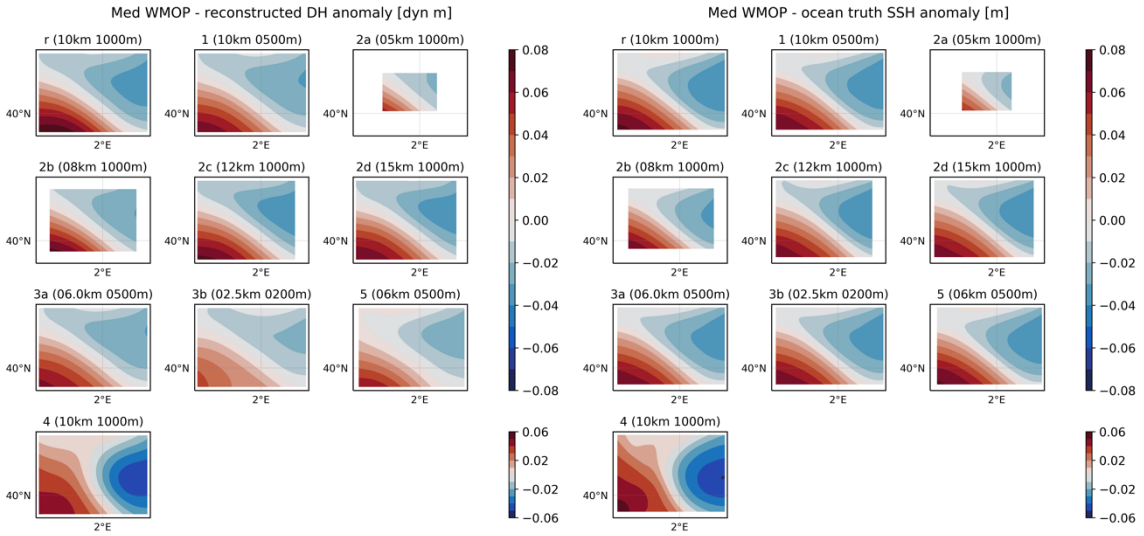

Figure 59: (Left) Dynamic height (DH) anomaly at the upper layer (5 m for all configurations except for configuration 5 (gliders), in which the upper layer is at 30 m) reconstructed from each configuration simulated from WMOP. (right) Sea surface height (SSH) anomaly from WMOP on the same date as each reconstruction (model fields were linearly interpolated to the date of the corresponding reconstruction (see Table 4)) and within the configuration domain. (all) To compute anomalies, the spatial average over each configuration domain is subtracted to the corresponding field. Note that to calculate statistics model fields are interpolated onto the reconstruction grid and the anomalies are computed within configuration 2a (5 km) domain for all configurations.

Reconstructed geostrophic velocity magnitude

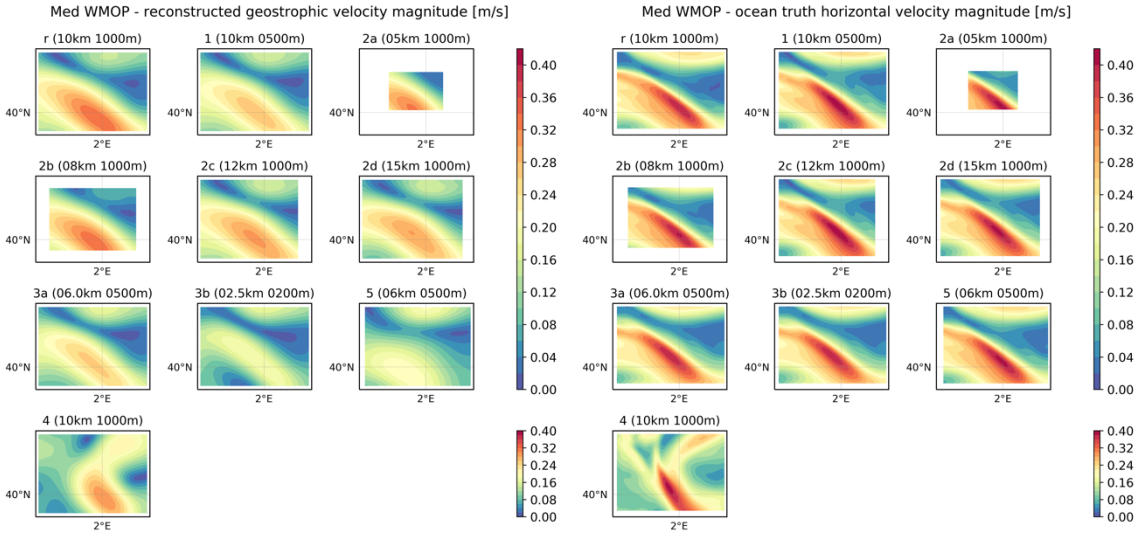

Figure 60: (Left) Geostrophic velocity magnitude at the upper layer (5 m for all configurations except for configuration 5 (gliders), in which the upper layer is at 30 m) reconstructed from each configuration simulated from WMOP. (right) Horizontal velocity magnitude from WMOP on the same date as each reconstruction (model fields were linearly interpolated to the date of the corresponding reconstruction (see table 4)) and within the configuration domain. Note that to calculate statistics model fields are interpolated onto the reconstruction grid and the statistics are computed within configuration 2a (5 km) domain for all configurations.

9.2. Maps of reconstructed fields in the Atlantic

Configurations simulated from the CMEMS global reanalysis

Reconstructed dynamic height

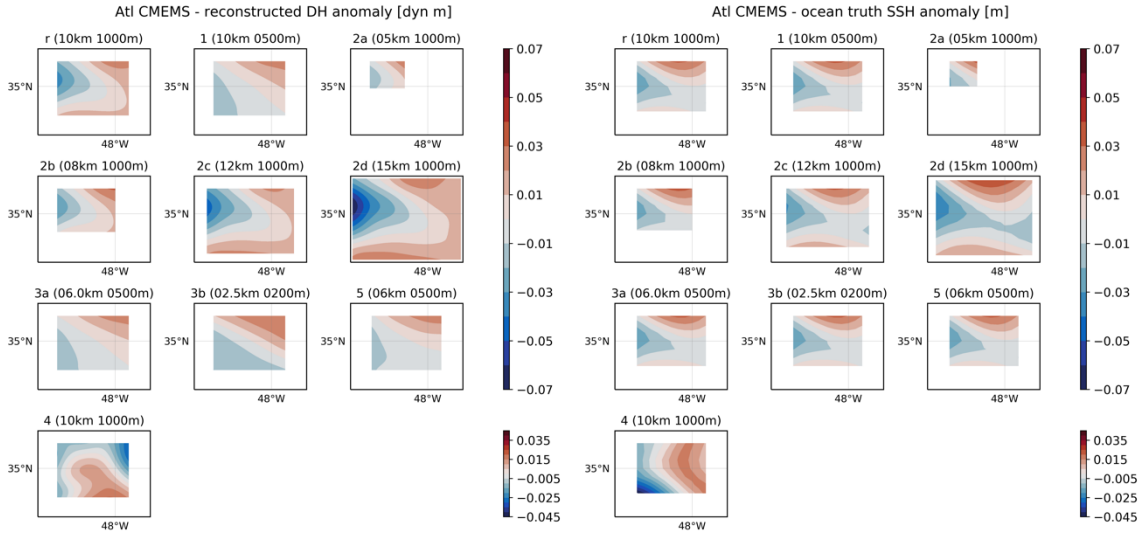

Figure 61: (Left) Dynamic height (DH) anomaly at the upper layer (5 m for all configurations except for configuration 5 (gliders), in which the upper layer is at 30 m) reconstructed from each configuration simulated from the CMEMS global reanalysis model in the Atlantic. (right) Sea surface height (SSH) anomaly from the CMEMS global reanalysis model on the same date as each reconstruction (model fields were linearly interpolated to the date of the corresponding reconstruction (see Table 4)) and within the configuration domain. (all) To compute anomalies, the spatial average over each configuration domain is subtracted to the corresponding field. Note that to calculate statistics model fields are interpolated onto the reconstruction grid and the anomalies are computed within configuration 2a (5 km) domain for all configurations.

Reconstructed geostrophic velocity magnitude

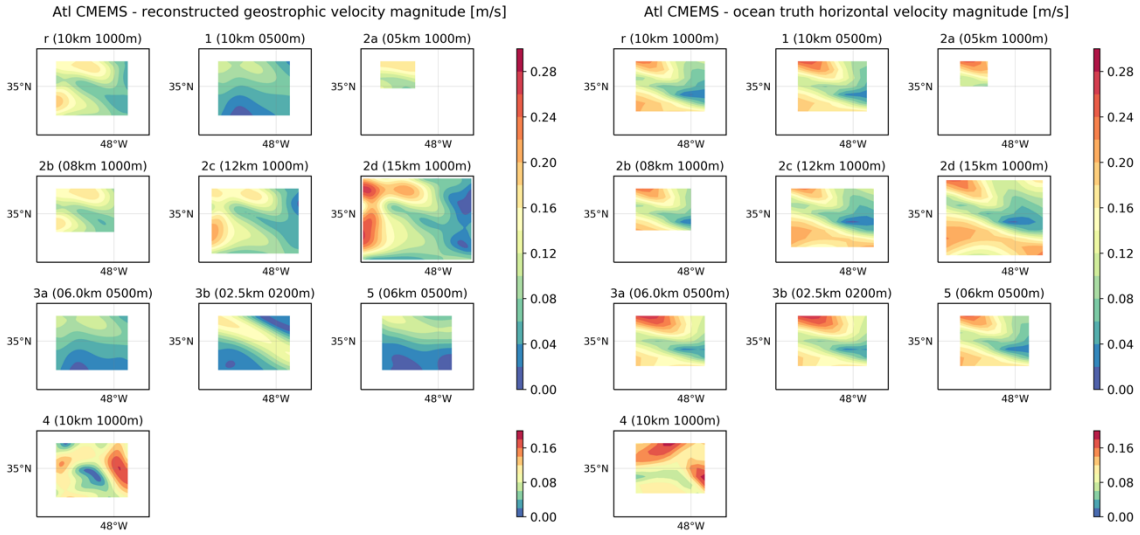

Figure 62: (Left) Geostrophic velocity magnitude at the upper layer (5 m for all configurations except for configuration 5 (gliders), in which the upper layer is at 30 m) reconstructed from each configuration simulated from the CMEMS global reanalysis model in the Atlantic. (right) Horizontal velocity magnitude from the CMEMS global reanalysis model on the same date as each reconstruction (model fields were linearly interpolated to the date of the corresponding reconstruction (see table 4)) and within the configuration domain. Note that to calculate statistics model fields are interpolated onto the reconstruction grid and the statistics are computed within configuration 2a (5 km) domain for all configurations.

Configurations simulated from eNATL60

Reconstructed dynamic height

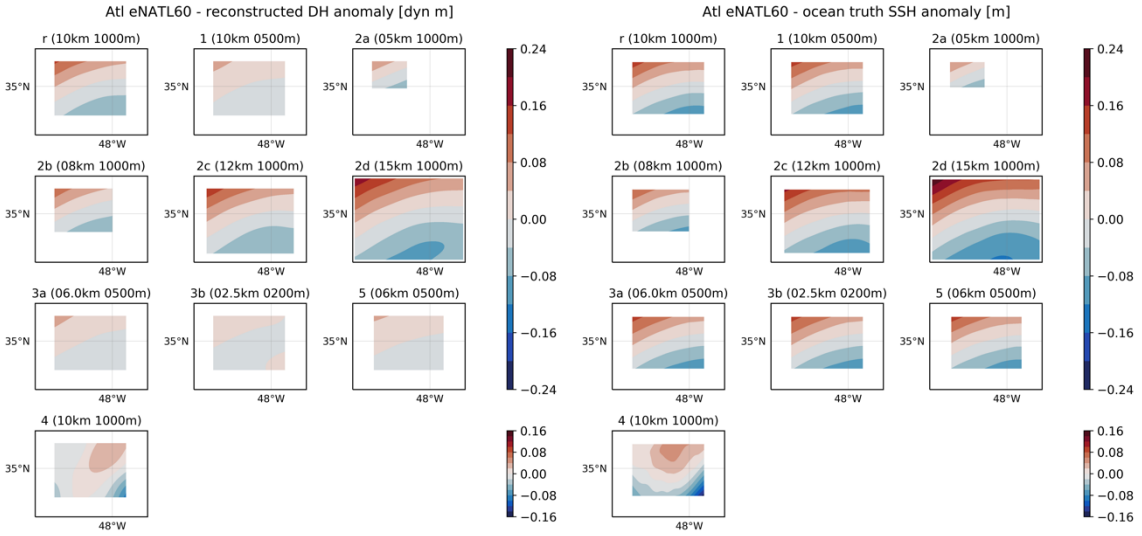

Figure 63: (Left) Dynamic height (DH) anomaly at the upper layer (5 m for all configurations except for configuration 5 (gliders), in which the upper layer is at 30 m) reconstructed from each configuration simulated from eNATL60 in the Atlantic. (right) Sea surface height (SSH) anomaly from eNATL60 on the same date as each reconstruction (model fields were linearly interpolated to the date of the corresponding reconstruction (see Table 4)) and within the configuration domain. (all) To compute anomalies, the spatial average over each configuration domain is subtracted to the corresponding field. Note that to calculate statistics model fields are interpolated onto the reconstruction grid and the anomalies are computed within configuration 2a (5 km) domain for all configurations.

Reconstructed geostrophic velocity magnitude

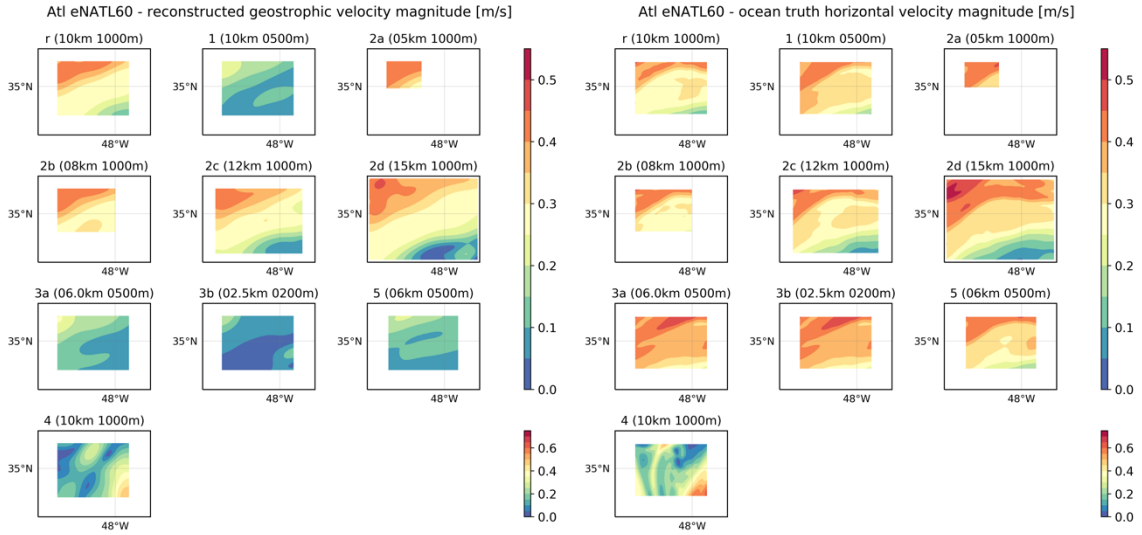

Figure 64: (Left) Geostrophic velocity magnitude at the upper layer (5 m for all configurations except for configuration 5 (gliders), in which the upper layer is at 30 m) reconstructed from each configuration simulated from eNATL60 in the Atlantic. (right) Horizontal velocity magnitude from eNATL60 on the same date as each reconstruction (model fields were linearly interpolated to the date of the corresponding reconstruction (see table 4)) and within the configuration domain. Note that to calculate statistics model fields are interpolated onto the reconstruction grid and the statistics are computed within configuration 2a (5 km) domain for all configurations.

9.3. Evaluation of the best sampling strategies

Approach

To evaluate the best configurations in each region, we compare the reconstructed fields (DH and geostrophic velocity magnitude) to the corresponding ocean truth fields (SSH and horizontal velocity magnitude) (Figures 55-60 for the Mediterranean, Figures 61-64 for the Atlantic). The comparison is done through the RMSE-based score (Figures 65-66 for the Mediterranean, Figures 67-68 for the Atlantic, Tables 6-9). The procedure consists of the following steps:

- Extract model fields in a bigger domain than the corresponding configuration. Linearly interpolate them to the date of the reconstruction and onto the reconstruction grid.
- Limit model and reconstructed fields within the domain of configuration 2a.
- Compute anomalies of DH and SSH subtracting the spatial average of each field over the new domain (configuration 2a).
- Calculate the RMSE-based score (RMSEs) between reconstructed and model fields, for each configuration, model and region.

$$\text{RMSE-based score} = 1 - [\text{RMS}(\text{reconstruction} - \text{truth})/\text{RMS}(\text{truth})]$$

Analysis in the Mediterranean

Comparison based on the DH reconstruction

The RMSE-based score (RMSEs) computed from the reconstructed DH and ocean truth SSH anomaly fields in the Mediterranean is represented in Figure 65 for each model and configuration, and in the leaderboard (Table 6). The configurations simulated from each model have similar scores between them, while the scores are different for each model. The reconstructions from eNATL60 have the highest scores, while the reconstructions from the CMEMS reanalysis have the lowest scores. This may be due to the root-mean-square of the ocean truth, that is different for each model and similar between different configurations simulated from the same model (see RMSE-based score equation). In addition, the eNATL60 has higher resolution than the other models. This may also impact the reconstructions. Here we evaluate the configurations with better scores for each model and then assess the best sampling strategies considering the results from the 3 models.

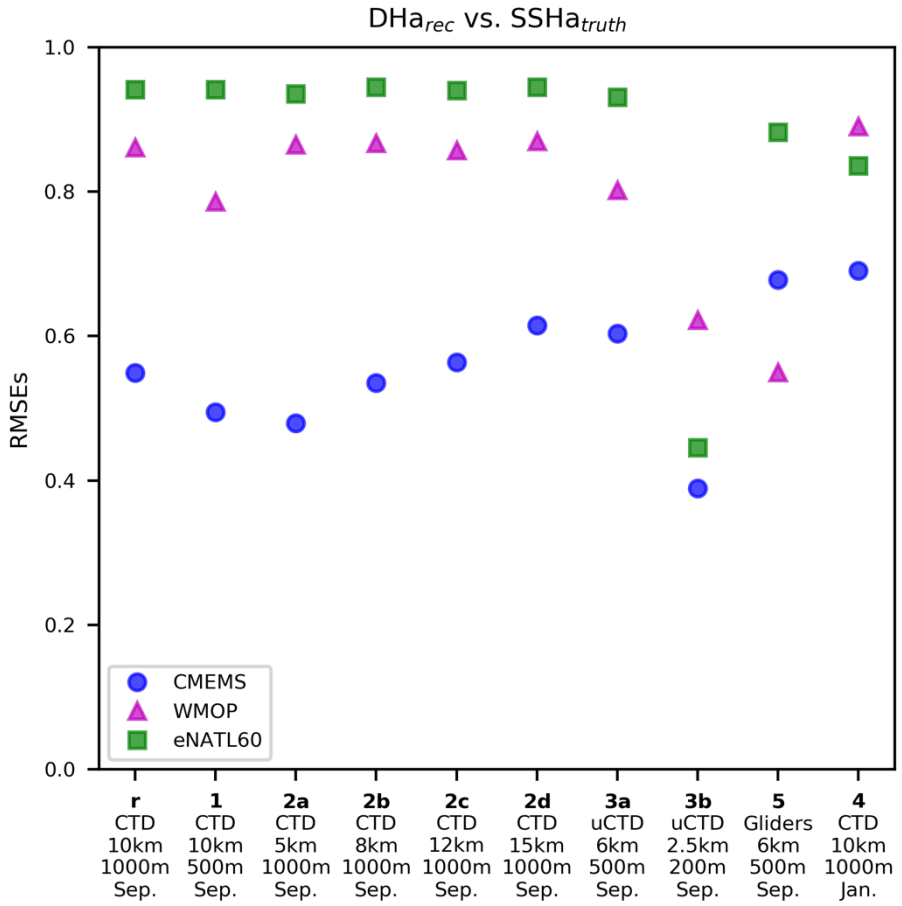

Figure 65: RMSE-based score (RMSEs) of the reconstructed DH anomaly vs. the ocean truth SSH anomaly for each configuration (x-axis) and model (different markers) for the Mediterranean.

A result that is clear from this analysis is that configuration 3b, in which CTD rosette casts are replaced by an underway CTD sampling one profile every 2.5 km and with a vertical extension of 200 m, is the configuration with the lowest scores for eNATL60 and CMEMS, and the second with the lowest scores for WMOP. Maps of DH show that for this configuration the values of DHa are lower than for the other reconstructions and ocean truth (Figures 55, 57 and 59). This may indicate that deeper profiles are needed in order to reconstruct the DH and geostrophic velocities at the ocean upper layer, while the increase on the horizontal resolution of CTD profiles does not introduce improvements with respect to the other configurations. For WMOP, configuration 5, in which CTD rosette casts are replaced by 7 gliders sampling zonal transects simultaneously, has the lowest scores.

Table 6. Leaderboard of all configurations evaluated in the Mediterranean (simulated from 3 different models), disregarding configuration 4 that is used to analyse seasonality. Leaderboard based on the RMSE-based score of the reconstructed DH anomaly vs. the ocean truth SSH anomaly.

Leaderboard for DH reconstruction		
Rank	**RMSEs**	**Configuration**
01	0.9448	2b (CTD 8km 1000m Sep.) eNATL60
02	0.9448	2d (CTD 15km 1000m Sep.) eNATL60
03	0.9412	1 (CTD 10km 500m Sep.) eNATL60
04	0.9411	r (CTD 10km 1000m Sep.) eNATL60
05	0.9404	2c (CTD 12km 1000m Sep.) eNATL60
06	0.9357	2a (CTD 5km 1000m Sep.) eNATL60
07	0.9307	3a (uCTD 6km 500m Sep.) eNATL60
08	0.8823	5 (Gliders 6km 500m Sep.) eNATL60
09	0.8694	2d (CTD 15km 1000m Sep.) WMOP
10	0.8674	2b (CTD 8km 1000m Sep.) WMOP
11	0.8650	2a (CTD 5km 1000m Sep.) WMOP
12	0.8609	r (CTD 10km 1000m Sep.) WMOP
13	0.8572	2c (CTD 12km 1000m Sep.) WMOP
14	0.8019	3a (uCTD 6km 500m Sep.) WMOP
15	0.7864	1 (CTD 10km 500m Sep.) WMOP
16	0.6781	5 (Gliders 6km 500m Sep.) CMEMS
17	0.6223	3b (uCTD 2.5km 200m Sep.) WMOP
18	0.6149	2d (CTD 15km 1000m Sep.) CMEMS
19	0.6034	3a (uCTD 6km 500m Sep.) CMEMS
20	0.5634	2c (CTD 12km 1000m Sep.) CMEMS
21	0.5495	5 (Gliders 6km 500m Sep.) WMOP
22	0.5491	r (CTD 10km 1000m Sep.) CMEMS
23	0.5352	2b (CTD 8km 1000m Sep.) CMEMS
24	0.4946	1 (CTD 10km 500m Sep.) CMEMS
25	0.4797	2a (CTD 5km 1000m Sep.) CMEMS
26	0.4457	3b (uCTD 2.5km 200m Sep.) eNATL60
27	0.3891	3b (uCTD 2.5km 200m Sep.) CMEMS

Regarding the best sampling strategies, with eNATL60 seven configurations have scores higher than 0.93 (Table 6): reference, 1, 2a-d, 3a. This means that different strategies provide reconstructions similar to the ocean truth and are good options. Configuration 5 has a lower score (0.8823) than the other configurations, but this value is still high.

For the sampling strategies simulated from WMOP, the configurations that consider CTD casts down to 1000 m and separated by different horizontal resolutions (reference, 2a-d) have RMSEs between 0.8572 and 0.8694; these scores are high and similar between them. Configurations that sample the water column down to 500 m depth have lower scores, however they are still high: configuration 3a has a RMSEs of 0.8019 and configuration 1 has a score of 0.7864. Between the reference configuration and configuration 1, which have the same horizontal resolution but different vertical extension, the difference in the RMSEs is 0.8609-0.7864=0.0745~0.07. This is the improvement introduced when sampling the depth layer between 500 and 1000 m depth, even if this sampling is slower (4.3125 days) than only sampling the upper 500 m (3.0625 days) (Table 3).

The configuration simulated from the CMEMS Mediterranean reanalysis with the highest RMSEs is the sampling strategy with gliders (configuration 5, 0.6781), consisting of CTD profiles down to 500 m depth and separated by 6 km. The other configurations with scores higher than 0.5 are: 2d (0.6149), 3a (0.6034), 2c (0.5634), r (0.5491) and 2b (0.5352). Maps of DH (Figure 55) show the higher absolute value of the anomalies computed from these reconstructions with respect to the reconstructions with lower scores (2a, 3b).

Configuration 4, that consists of the same sampling strategy as the reference but starting the sampling in January instead of in September, has high scores with the three models evaluated: 0.8356 with eNATL60, 0.8903 with WMOP, 0.6905 with CMEMS. These values are higher than the RMSEs obtained for the reference configuration simulated from WMOP (0.8609) and CMEMS (0.5491), and lower for the configuration simulated from eNATL60 (0.9411). This means that in both seasons the reference configuration, consisting of CTD casts separated by 10 km and down to 1000 m, provides reconstructions with high scores. Note that in different periods there are different structures in the same study region, and in winter the upper layer is characterized by smaller scales because the mixed-layer decreases the first Rossby radius of deformation (ref.). Even with these differences between seasons, the reference configuration is a sampling strategy that provides reconstructions similar to the ocean truth in both cases.

Comparison based on the geostrophic velocity reconstruction

With respect to the RMSEs computed from the reconstructed geostrophic velocity magnitude, it is important to note that the ocean truth field also includes the ageostrophic component of the horizontal flow. As a result of this, high scores indicate that the reconstruction is similar to the ocean truth and that this field is dominated by geostrophic balance (Barceló-Llull et al., 2021). Otherwise, low scores may mean that the ocean truth is dominated by ageostrophic motions and/or that the reconstruction is not able to capture the structures of the ocean truth.

For the reconstruction of geostrophic velocity magnitude, similarly than for the DH, the configurations simulated from eNATL60 have the highest scores, while the ones simulated from the CMEMS reanalysis have the lowest values (Figure 66, and Table 7). However, there are two differences with respect to the reconstruction of DH: (i) with the three models we obtain more similar values of RMSEs, and (ii) the scores are more different between configurations simulated from the same model.

In this case, configuration 3b, considering uCTD profiles down to 200 m depth with a horizontal separation of 2.5 km, is also the sampling strategy with the lowest scores for eNATL60 and CMEMS, and the second with the lowest scores for WMOP, supporting the result obtained for DH. For WMOP, configuration 5, consisting of seven gliders sampling zonal transects simultaneously, has the lowest score. Maps of the reconstructed geostrophic velocity magnitude (Figures 56, 58 and 60) show that with configuration 3b the reconstructed field has lower magnitude than the ocean truth and the other reconstructions, except for WMOP that the reconstructed velocity for configuration 5 has also low values.

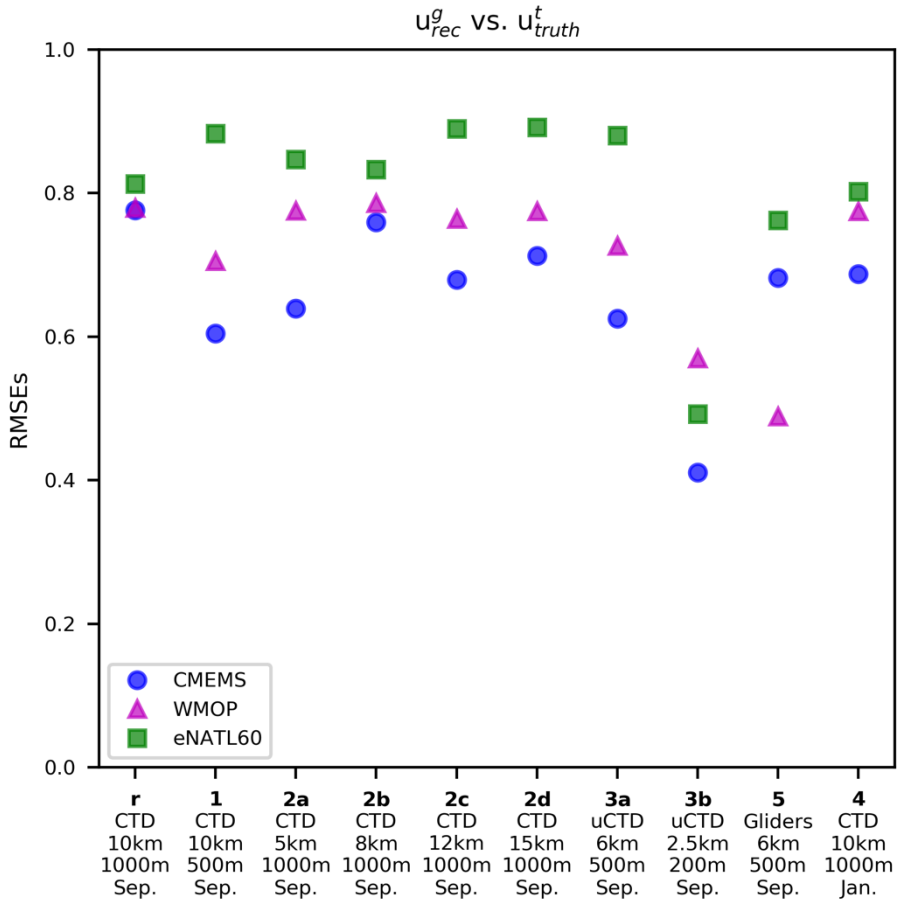

Figure 66: RMSE-based score (RMSEs) of the reconstructed geostrophic velocity magnitude vs. the ocean truth horizontal velocity magnitude for each configuration (x-axis) and model (different markers) for the Mediterranean.

To evaluate the best sampling strategies, we focus on the results obtained for each model. With eNATL60 four configurations have scores higher than 0.88 (Table 7): 2d (15 km, 1000 m), 2c (12 km, 1000 m), 1 (10 km, 500 m), and 3a (uCTD, 6 km, 500 m). The configurations 2a (5 km, 1000 m), 2b (8 km, 1000 m) and reference (10 km, 1000 m) have scores between 0.81 and 0.85. In all cases the reconstructed velocity has lower magnitude than the ocean truth (Figure 58). However, the ocean truth horizontal velocity is different for each configuration: for configurations 2d, 2c, 1, and 3a has lower magnitude than for configurations 2a, 2b and reference. This variation in magnitude may introduce the differences in RMSEs observed between the two sets of configurations. The reconstructed geostrophic velocity for the sampling strategy with gliders has also lower magnitude than the ocean truth; the RMSEs for configuration 5 is 0.7623. The sampling strategy considering uCTD profiles down to 200 m depth and with a horizontal spacing of 2.5 km (configuration 3b) provides the reconstruction with the lowest score (0.4457). The low magnitude of the reconstructed geostrophic velocity for all configurations simulated from eNATL60 may be due to the ageostrophic motions represented by the ocean truth and not resolved by our reconstruction (Barceló-Llull et al., 2021).

Concerning the patterns of maximum horizontal velocity, the ocean truth fields have an elongated shape-oriented northwest-southeast, while the reconstructed fields have a more circular shape (Figure 58). The difference in pattern is more evident in configuration 4 (winter). In summer the upper layer is stratified due

to solar warming, while in winter there is a mixed layer that decreases the first Rossby radius of deformation and, in consequence, the structures are smaller. In winter the reconstructed field is not able to represent the small-scales observed in the ocean truth. This is expected due to the sampling resolution (10 km) and spatial correlation scale (20 km) used in the optimal interpolation. The reconstructed geostrophic velocity magnitude for the same sampling strategy in winter (configuration 4) has a RMSEs of 0.8019 while in summer (reference configuration) is 0.8130, high scores in both cases.

Table 7. Leaderboard of all configurations evaluated in the Mediterranean (simulated from 3 different models), disregarding configuration 4 that is used to analyse seasonality. Leaderboard based on the RMSE-based score of the reconstructed geostrophic velocity magnitude vs. the ocean truth horizontal velocity magnitude.

Leaderboard for geostrophic velocity reconstruction		
Rank	**RMSEs**	**Configuration**
01	0.8915	2d (CTD 15km 1000m Sep.) eNATL60
02	0.8897	2c (CTD 12km 1000m Sep.) eNATL60
03	0.8829	1 (CTD 10km 500m Sep.) eNATL60
04	0.8802	3a (uCTD 6km 500m Sep.) eNATL60
05	0.8467	2a (CTD 5km 1000m Sep.) eNATL60
06	0.8331	2b (CTD 8km 1000m Sep.) eNATL60
07	0.8130	r (CTD 10km 1000m Sep.) eNATL60
08	0.7859	2b (CTD 8km 1000m Sep.) WMOP
09	0.7792	r (CTD 10km 1000m Sep.) WMOP
10	0.7760	r (CTD 10km 1000m Sep.) CMEMS
11	0.7757	2a (CTD 5km 1000m Sep.) WMOP
12	0.7750	2d (CTD 15km 1000m Sep.) WMOP
13	0.7642	2c (CTD 12km 1000m Sep.) WMOP
14	0.7623	5 (Gliders 6km 500m Sep.) eNATL60
15	0.7595	2b (CTD 8km 1000m Sep.) CMEMS
16	0.7268	3a (uCTD 6km 500m Sep.) WMOP
17	0.7128	2d (CTD 15km 1000m Sep.) CMEMS
18	0.7050	1 (CTD 10km 500m Sep.) WMOP
19	0.6820	5 (Gliders 6km 500m Sep.) CMEMS
20	0.6796	2c (CTD 12km 1000m Sep.) CMEMS
21	0.6392	2a (CTD 5km 1000m Sep.) CMEMS
22	0.6255	3a (uCTD 6km 500m Sep.) CMEMS
23	0.6044	1 (CTD 10km 500m Sep.) CMEMS
24	0.5696	3b (uCTD 2.5km 200m Sep.) WMOP
25	0.4926	3b (uCTD 2.5km 200m Sep.) eNATL60
26	0.4892	5 (Gliders 6km 500m Sep.) WMOP
27	0.4109	3b (uCTD 2.5km 200m Sep.) CMEMS

The sampling strategies simulated from WMOP allow the reconstruction of the geostrophic velocity field with a pattern similar to the ocean truth (Figure 60). In summer the maximum magnitude is distributed in an elongated northwest-southeast shape in both the ocean truth and the reconstructed fields for those configurations with RMSEs higher than 0.7 (Table 7): reference (10 km, 1000 m), 1 (10 km, 500 m), 2a-d (5, 8, 12, 15 km, 1000 m), 3a (uCTD, 6 km, 500 m). The sampling strategy with uCTD considering profiles down to 200 m depth and with a horizontal spacing of 2.5 km (configuration 3b) also reconstructs an elongated

shape, but the magnitude is lower than for the other reconstructions (RMSEs = 0.5696). The configuration with the lowest score is the sampling strategy with gliders (RMSEs = 0.4892). In this case the magnitude is low and the pattern is more circular than the elongated shape of the ocean truth.

Considering the best reconstructions for WMOP, the configurations with a CTD cast separation of 5 km (2a), 8 km (2b) and 10 km (reference) represent the geostrophic velocity with a higher magnitude than the configurations with a horizontal spacing of 12 km (2c) and 15 km (2d) (Figure 60). Configuration 1, that has the same horizontal resolution than the reference but the CTD profiles sample the water column down to 500 m instead of 1000 m, and configuration 3a, consisting of uCTD profiles down to 500 m separated by 6 km, have scores of 0.7050 and 0.7268, respectively, and reconstruct a lower magnitude than the previous sampling strategies.

In conclusion, for the configurations simulated from WMOP, the sampling strategies that provide reconstructions more similar to the ocean truth consists of CTD casts down to 1000 m depth and separated by 5, 8 and 10 km. While configurations separated by 12 and 15 km or down to 500 m depth reproduce the shape of the horizontal velocity magnitude but with lower values. With a cast separation of 5 or 8 km, the sampling domain has to be reduced in order to obtain synoptic fields, while with a separation of 12 and 15 km we can sample the same domain as the reference configuration but faster, loosing spatial resolution but obtaining good reconstructions for the period evaluated. A good compromise is the reference configuration: CTD casts separated by 10 km and down to 1000 m depth. To sample the domain in a shorter period, an alternative is to release the CTD casts down to 500 m depth (configuration 1). With this sampling strategy we can reconstruct a shape similar to the ocean truth with a lower horizontal velocity magnitude, which introduces a difference in RMSEs of 0.7792-0.7050 = 0.0742 ~ 0.07 with respect to the same configuration but with casts down to 1000 m. Another option is to replace CTD casts for an uCTD with a horizontal spacing between profiles of 6 km and a vertical extension of 500 m. This strategy has the advantage to sample the same domain in 1.75 days in comparison to 4.31 days for the reference configuration and 3.06 days for configuration 1.

Concerning seasonality, in winter the pattern of maximum horizontal velocity magnitude is different than in summer as different structures are present in the region of study (configuration 4 in Figure 60), but the sampling strategy consisting of CTD casts separated by 10 km and down to 1000 m allows a reconstruction with a RMSEs of 0.7749, similar to the value obtained in summer (0.7792).

The configuration simulated from the CMEMS Mediterranean reanalysis with the highest scores is the reference (0.7760), followed by configurations 2b, 2d, 5, 2c, 2a, 3a and 1 (Table 7), all of them representing a similar pattern of geostrophic velocity with an underestimation of the magnitude with respect to the ocean truth (Figure 56). The reconstruction with the lowest scores is from configuration 3b (0.4109); the magnitude captured by this sampling strategy is lower than for the other configurations. Regarding seasonality, the ocean truth in winter shows higher small-scale variability than in summer. The reconstruction smooths the fields, but the overall pattern is similar, with a slight underestimation of the magnitude (RMSEs = 0.6871).

Analysis in the Atlantic

Comparison based on the DH reconstruction

The RMSE-based score (RMSEs) computed from the reconstructed DH and ocean truth SSH anomaly fields in the Atlantic is represented in Figure 67 for each model and configuration, and in the leaderboard (Table 8). The configurations simulated from the CMEMS global reanalysis have similar scores, while the configurations

from eNATL60 have important dissimilarities between them. The eNATL60 has higher resolution (hourly and 1/60º) than the CMEMS reanalysis (daily and 1/12°), hence, each model resolves different dynamics and distinct results are expected.

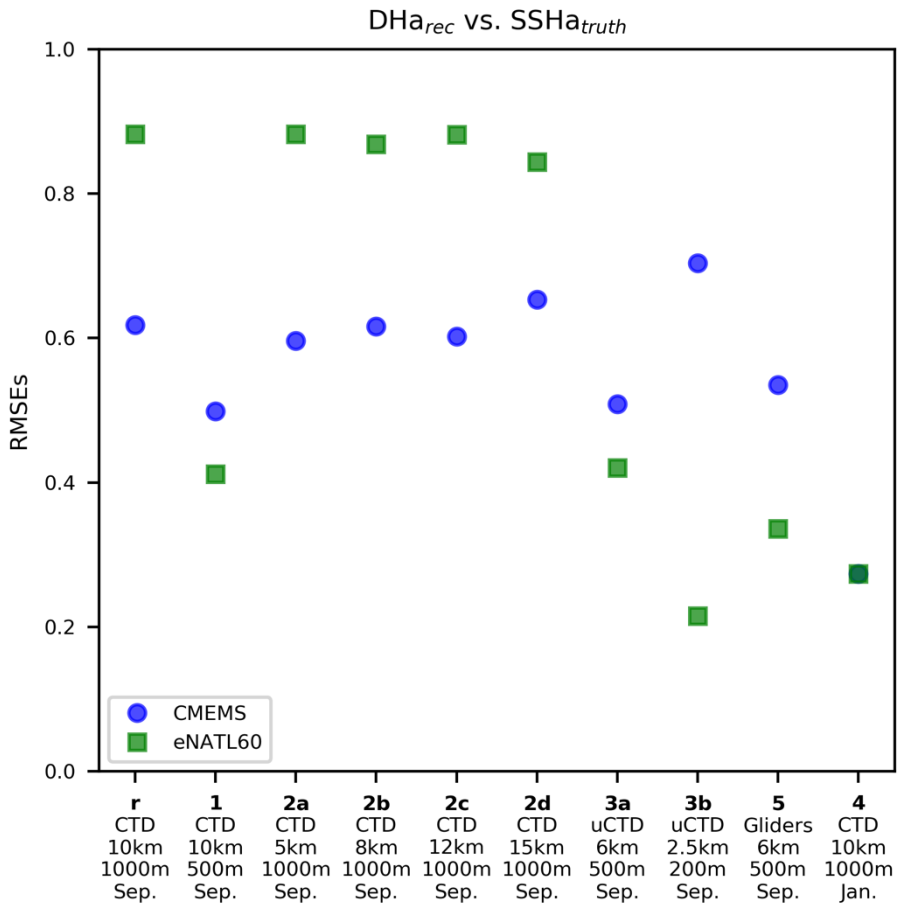

Figure 67: RMSE-based score (RMSEs) of the reconstructed DH anomaly vs. the ocean truth SSH anomaly for each configuration (x-axis) and model (different markers) for the Atlantic.

For the sampling strategies simulated from the CMEMS reanalysis, the reconstruction with the highest score is configuration 3b (RMSEs = 0.7038): underway CTD replacing CTD rosette casts, horizontal separation between profiles of 2.5 km, vertical extension of 200 m depth, and sampling time 1.75 days. This is the configuration with the highest spatial resolution and shorter sampling time. The reconstruction with the second highest scores is for configuration 2d (0.6536), the configuration with the lower spatial resolution (15 km) and higher sampling time (5.19 days). The important dissimilarities between both sampling strategies and the smooth fields of reconstructed DH (Figure 61) difficult the interpretation of this result and make necessary the analysis of the reconstructed geostrophic velocity magnitude.

A result that is clear from the remaining configurations is that the sampling strategies consisting of CTD profiles down to 1000 m depth (r, 2b, 2c, 2a) have similar scores of ~0.6, while the strategies that sample the water column down to 500 m depth (5, 3a, 1) have lower scores. The DH reconstructed from the sampling strategies with CTD profiles down to 1000 m has a pattern similar to the ocean truth, while the reconstruction of the configurations with profiles down to 500 m do not capture this feature and the fields are characterized

by a smooth north-east south-west decrease (Figure 61). In consequence, in the Atlantic, considering the results from the CMEMS reanalysis with a spatial resolution of 1/12º, the sampling of the water column down to 1000 m is key for the reconstruction of DH at the upper layer. The difference in RMSEs between the reference configuration and the same sampling strategy but with profiles down to 500 m (configuration 1) is 0.6180 - 0.4986 = 0.1194 ~ 0.12.

Concerning seasonality, configuration 4 has a RMSEs of 0.2735, much lower than the reference configuration (same configuration but in summer). This suggests that the sampling strategy that provides good reconstructions in summer, does not capture the structures present in the region of study in winter (Figure 61).

Table 8. Leaderboard of all configurations evaluated in the Atlantic (simulated from 2 different models), disregarding configuration 4 that is used to analyse seasonality. Leaderboard based on the RMSE-based score of the reconstructed DH anomaly vs. the ocean truth SSH anomaly.

Leaderboard for DH reconstruction		
Rank	**RMSEs**	**Configuration**
01	0.8825	2a (CTD 5km 1000m Sep.) eNATL60
02	0.8821	r (CTD 10km 1000m Sep.) eNATL60
03	0.8817	2c (CTD 12km 1000m Sep.) eNATL60
04	0.8681	2b (CTD 8km 1000m Sep.) eNATL60
05	0.8436	2d (CTD 15km 1000m Sep.) eNATL60
06	0.7038	3b (uCTD 2.5km 200m Sep.) CMEMS
07	0.6536	2d (CTD 15km 1000m Sep.) CMEMS
08	0.6180	r (CTD 10km 1000m Sep.) CMEMS
09	0.6160	2b (CTD 8km 1000m Sep.) CMEMS
10	0.6020	2c (CTD 12km 1000m Sep.) CMEMS
11	0.5962	2a (CTD 5km 1000m Sep.) CMEMS
12	0.5349	5 (Gliders 6km 500m Sep.) CMEMS
13	0.5084	3a (uCTD 6km 500m Sep.) CMEMS
14	0.4986	1 (CTD 10km 500m Sep.) CMEMS
15	0.4207	3a (uCTD 6km 500m Sep.) eNATL60
16	0.4116	1 (CTD 10km 500m Sep.) eNATL60
17	0.3363	5 (Gliders 6km 500m Sep.) eNATL60
18	0.2152	3b (uCTD 2.5km 200m Sep.) eNATL60

With eNATL60 the difference between the reconstruction of configurations considering profiles down to 1000 m depth versus only sampling the upper 500 m is more evident. The first set of sampling strategies (r, 2a-d) have scores higher than 0.84, while the second set (3a, 1, 5) have scores below 0.42. Configuration 3b, only considering profiles down to 200 m depth, has the lowest score (0.2152). The dissimilarities between reconstructions can be clearly observed in the DH maps (Figure 63): for the reference configuration and configurations 2a-d the reconstructed DH has a magnitude and pattern similar to the ocean truth, while for the other configurations the magnitude is underestimated. This reinforces the conclusion obtained from the CMEMS simulated configurations. In the Atlantic study region, CTD profiles that sample the water column down to 1000 m depth can capture the SSH features observed in the ocean truth. This conclusion is supported

by simulating the same set of configurations with two models with distinct horizontal resolutions and, hence, resolving different dynamics.

Configuration 4 simulated from eNATL60 reconstructs the DH with a low RMSEs of 0.2738, similar to the result obtained for the other model. The difference in RMSEs between the reconstructed DH in summer vs. in winter with the same sampling strategy is 0.8821 - 0.2738 = 0.6083 ~ 0.61; with the CMEMS reanalysis this difference is 0.6180 - 0.2735 = 0.3445 ~ 0.34. One explanation for these dissimilarities detected from two models with different spatial and temporal resolutions may be that in winter the structures evolve faster than in summer and the lack of synopticity in the pseudo-observations introduces significant errors in the reconstruction.

Comparison based on the geostrophic velocity reconstruction

The RMSEs computed for the reconstructed geostrophic velocity magnitude supports the results derived from the analysis of DH. The sampling strategies consisting of CTD profiles down to 1000 m depth (r, 2a-d) have the highest scores for both models (Figure 68 and Table 9). Considering the configurations simulated from CMEMS with CTD profiles down to 500 m depth, configuration 5 has a score of 0.5847, configuration 1 has a score of 0.5022 and configuration 3a has the lowest score, 0.4571. Strikingly, for this model configuration 3b has a RMSEs relatively high (0.6143). Maps of geostrophic velocity magnitude (Figure 62) show that for this model the reference configuration and configurations 2a-d have higher magnitude than for the other configurations, and this magnitude is similar to the ocean truth horizontal velocity, with an overall slight underestimation. The reconstructions with the highest scores have slight dissimilarities in the magnitude of geostrophic velocity that are translated in distinct RMSEs: configuration 2d has the highest scores because the reconstructed magnitude is higher and, hence, more approximate to the ocean truth. The configurations with profiles down to 500 m depth have a comparable magnitude between them and this is ~50% smaller than the ocean truth. The pattern of geostrophic velocity magnitude for the configuration with gliders is closer to the ocean truth within the region of study, this results in a higher score. Configuration 3b, with profiles down to 200 m depth, has higher magnitude than the configurations with profiles down to 500 m depth. The reason for this discrepancy may be that the spatial resolution of 2.5 km captures small-scale variability with higher horizontal velocity. However, the CMEMS global reanalysis has daily and 1/12º horizontal resolution that prevent the pseudo-observations to capture small-scales.

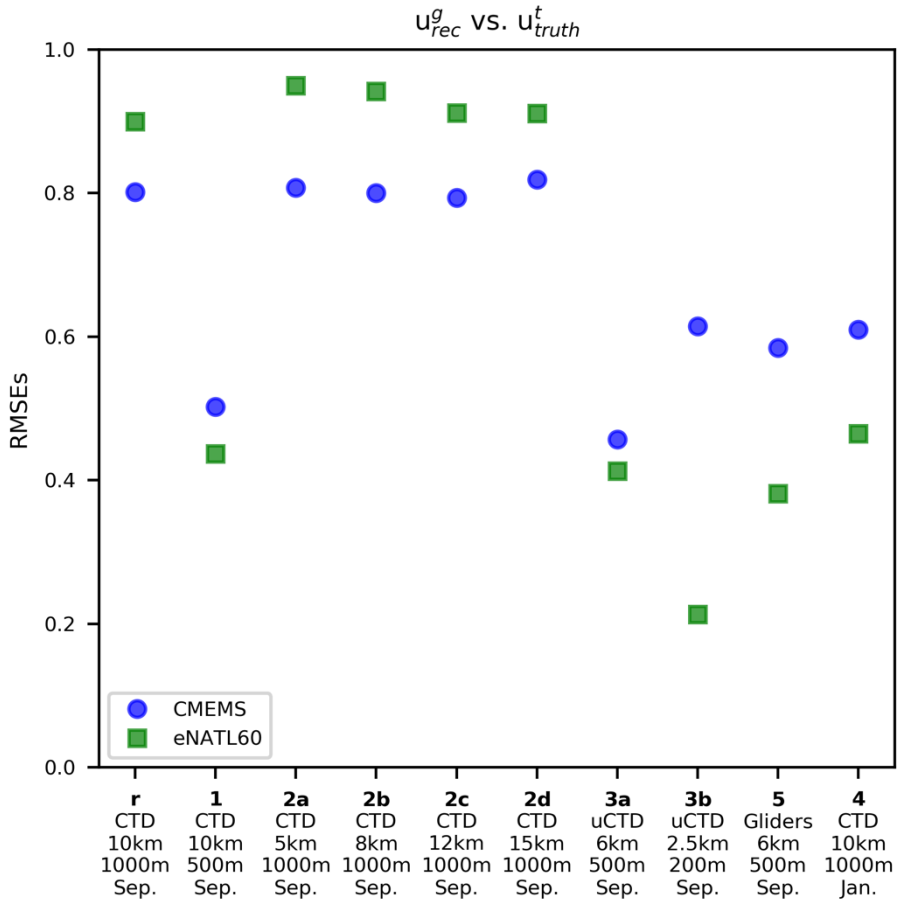

Figure 68: RMSE-based score (RMSEs) of the reconstructed geostrophic velocity magnitude vs. the ocean truth horizontal velocity magnitude for each configuration (x-axis) and model (different markers) for the Atlantic.

For the configurations simulated from eNATL60, the sampling strategies with profiles down to 1000 m have a magnitude and pattern closer to the ocean truth (Figure 64). The magnitude of geostrophic velocity for the configurations with profiles down to 500 m depth is ~50% lower than the ocean truth, and for configuration 3b this underestimation is 60% lower than the ocean truth.

Table 9. Leaderboard of all configurations evaluated in the Atlantic (simulated from 2 different models), disregarding configuration 4 that is used to analyse seasonality. Leaderboard based on the RMSE-based score of the reconstructed geostrophic velocity magnitude vs. the ocean truth horizontal velocity magnitude.

Leaderboard for geostrophic velocity reconstruction		
Rank	**RMSEs**	**Configuration**
01	0.9494	2a (CTD 5km 1000m Sep.) eNATL60
02	0.9417	2b (CTD 8km 1000m Sep.) eNATL60
03	0.9116	2c (CTD 12km 1000m Sep.) eNATL60
04	0.9109	2d (CTD 15km 1000m Sep.) eNATL60
05	0.8999	r (CTD 10km 1000m Sep.) eNATL60
06	0.8189	2d (CTD 15km 1000m Sep.) CMEMS
07	0.8075	2a (CTD 5km 1000m Sep.) CMEMS
08	0.8015	r (CTD 10km 1000m Sep.) CMEMS
09	0.8002	2b (CTD 8km 1000m Sep.) CMEMS
10	0.7934	2c (CTD 12km 1000m Sep.) CMEMS
11	0.6143	3b (uCTD 2.5km 200m Sep.) CMEMS
12	0.5847	5 (Gliders 6km 500m Sep.) CMEMS
13	0.5022	1 (CTD 10km 500m Sep.) CMEMS
14	0.4571	3a (uCTD 6km 500m Sep.) CMEMS
15	0.4369	1 (CTD 10km 500m Sep.) eNATL60
16	0.4130	3a (uCTD 6km 500m Sep.) eNATL60
17	0.3814	5 (Gliders 6km 500m Sep.) eNATL60
18	0.2132	3b (uCTD 2.5km 200m Sep.) eNATL60

Concerning seasonality, configuration 4 has a RMSEs lower than for the reference configuration for both models: 0.4651 for eNATL60 (vs. 0.8999) and 0.6097 for CMEMS (vs. 0.8015). With eNATL60 the reconstructed field is smoother than the ocean truth but the overall pattern shows some similarity (Figure 64). For CMEMS, the reconstructed and ocean truth fields within the region of comparison (domain of configuration 2a) have some resemblance, but for the whole domain (Figure 62) the cells of maximum and minimum velocity are not properly represented by the reconstruction.

9.4. Conclusions

Mediterranean

Best sampling strategies

To evaluate the best sampling strategies in the Mediterranean, we focus on the results obtained for each model considering the two variables analysed: DH and geostrophic velocity magnitude.

The configuration simulated from the CMEMS Mediterranean reanalysis with the leading RMSEs for the DH reconstruction is the sampling strategy with gliders, followed by the configurations considering CTD casts down to 1000 m and separated by 8, 10, 12 and 15 km, and configuration 3a (uCTD, 6 km of horizontal spacing and a vertical extension of 500 m). The best score for the geostrophic velocity reconstruction is for the reference configuration. The other configurations capture a similar pattern of geostrophic velocity, while the magnitude for all configurations is lower than the ocean truth horizontal velocity.

With eNATL60 seven configurations (reference, 1, 2a-d, 3a) have high scores for the reconstruction of DH (RMSEs>0.93) and geostrophic velocity magnitude (RMSEs>0.81). In all cases the reconstructed velocity has

inferior magnitude than the ocean truth horizontal velocity. However, the ocean truth has distinct magnitude for each configuration and this dissimilarity may introduce the small differences in the RMSEs between configurations. This suggests that distinct strategies provide reconstructions similar to the ocean truth and, hence, they are good options. The reconstructed geostrophic velocity for the sampling strategy with gliders has also lower magnitude than the ocean truth and the RMSEs for this configuration is inferior than for the other configurations. The smaller magnitude of the reconstructed geostrophic velocity for all configurations may indicate that the ocean truth has ageostrophic motions not resolved by our reconstruction (Barceló-Llull et al., 2021).

For the sampling strategies simulated from WMOP, the configurations that consider CTD casts down to 1000 m and separated by different horizontal resolutions (reference, 2a-d) have the leading scores for the DH reconstruction. Configurations that sample the water column down to 500 m depth have inferior scores but they are still high. For the same strategy consisting of CTD casts separated by 10 km, the RMSEs improvement when sampling the water column down to 1000 m instead of 500 m is 0.07 in the DH reconstruction, even if this configuration is slower (4.3 days vs. 3.1 days).

Regarding the velocity field, the sampling strategies that provide reconstructions more similar to the ocean truth consists of CTD casts down to 1000 m depth and separated by 5, 8 and 10 km. Configurations separated by 12 and 15 km or down to 500 m depth reproduce the shape of the horizontal velocity magnitude but with inferior values. A good compromise considering the advantages of each sampling strategy is the reference configuration: CTD casts separated by 10 km and down to 1000 m depth. To sample the domain faster (3.1 days vs. 4.3 days), a valid strategy is configuration 1 (CTD profiles down to 500 m depth) from which the reconstructed geostrophic velocity field has a smaller magnitude that is responsible for a decrease of 0.07 in the RMSEs, while the pattern is maintained similar to the ocean truth. An even faster valid sampling (1.8 days) consists of replacing rosette CTD casts for an underway CTD with a horizontal spacing between profiles of 6 km and a vertical extension of 500 m; the RMSEs reduction in this case is 0.05, which makes this configuration a better option than configuration 1. Note that the variability and scales resolved by WMOP have been validated by an extensive set of real observations in the western Mediterranean (Mourre et al., 2018). This implies that the results obtained from WMOP may be more approximate to what we would have in the real ocean. In addition, the conclusions from WMOP are consistent with the results obtained from the other models.

Sampling strategy not appropriate for our objective

A result that is clear from the analysis in the Mediterranean is that the sampling strategy in which CTD rosette casts are replaced by an underway CTD sampling one profile every 2.5 km and with a vertical extension of 200 m is the configuration with the lowest scores for eNATL60 and CMEMS, and the second with the lowest scores for WMOP for the two variables analysed. Maps of reconstructed geostrophic velocity show that for this configuration the reconstructed field has lower magnitude than for the ocean truth and the other reconstructions, with the exception of configuration 5 for WMOP. This suggests that profiles deeper than 200 m depth are needed to reconstruct the DH and geostrophic velocities at the ocean upper layer, while the decrease of the horizontal separation between profiles does not introduce improvements with respect to the other configurations.

Impact of season

Configuration 4, that consists of the same sampling strategy as the reference but in winter instead of in summer, has high scores for the DH reconstruction with the three models. These values are larger than for

the reference configuration for WMOP and CMEMS, and lower for eNATL60. This indicates that in both seasons the reference configuration, consisting of CTD casts separated by 10 km and down to 1000 m, provides reconstructions of DH with high scores.

Note that different dynamics characterize the region of study in each season. In summer the upper layer is stratified due to solar warming, while in winter there is a mixed layer that decreases the first Rossby radius of deformation and, in consequence, the structures are smaller. The sampling resolution of 10 km and the spatial correlation scale of 20 km applied to the optimal interpolation prevent the representation of spatial scales smaller than ~20 km. This results in smoother reconstructed fields of geostrophic velocity magnitude in comparison to the ocean truth in winter. Besides this, with eNATL60 the RMSEs in winter is still elevated (0.8019) and comparable to the score obtained in summer (0.8130). For WMOP the outcome is similar and the RMSEs in winter is 0.7749 in front of 0.7792 in summer. The ocean truth from CMEMS also shows higher small-scale variability than in summer and than in the reconstruction; in this case the RMSEs is 0.6871 vs. 0.7760 in summer. In conclusion, even with distinct dynamics, the reference configuration is a sampling strategy that provides reconstructions similar to the ocean truth in both seasons.

Atlantic

Best sampling strategies

The main conclusion derived from the analysis in the Atlantic is that sampling strategies consisting of CTD profiles down to 1000 m depth (reference, 2a-d) provide reconstructions with higher scores than the strategies that sample the water column down to 500 m depth (1, 3a, 5). This is observed with configurations simulated from both models and for the reconstructed DH and geostrophic velocity magnitude. The geostrophic velocity reconstructed from the strategies that sample only the upper 500 m depth has a magnitude ~50% smaller than the ocean truth total horizontal velocity, while the strategies that sample the water column down to 1000 m reconstruct a magnitude closer to the ocean truth. In consequence, in the Atlantic study region the sampling of the water column down to 1000 m is key for the reconstruction of DH and geostrophic velocity magnitude at the upper layer. This conclusion is supported by simulating the same set of configurations with two models with distinct spatial and temporal resolutions and, hence, resolving different dynamics.

Sampling strategies consisting of CTD profiles down to 1000 m depth and with a horizontal separation of 5, 8, 10, 12 and 15 km are good options to reconstruct fine-scale currents (~20 km) at the ocean upper layer in the region of study in the period analysed. The differences in the horizontal spacing of these strategies imply that distinct sizes of the domain can be sampled for a fixed sampling period. The reference configuration, which considers a distance between casts of 10 km, is a good compromise between horizontal resolution, spatial coverage and sampling duration.

Sampling strategy not appropriate for our objective

From eNATL60, configuration 3b, in which rosette CTD casts are replaced by an underway CTD sampling one profile every 2.5 km and with a vertical extension of 200 m, reconstructs the geostrophic velocity field with an underestimation of 60% in magnitude with respect to the ocean truth. This result is not consistent with the outcome from the CMEMS reanalysis. However, the eNATL60 horizontal resolution is more suited for the simulation of this sampling strategy and, hence, we disregard this sampling strategy as a good option for our purpose.

Impact of season

The analysis of seasonality suggests that the reference configuration, that provides good reconstructions in summer, does not capture the structures present in the region of study in winter. One explanation may be that in winter the structures evolve faster than in summer and the lack of synopticity in the pseudo-observations introduces significant errors in the reconstruction.

9.5. Perspectives

The next step is to evaluate an additional strategy for SWOT validation consisting of station-keeping gliders, i.e., gliders working as moorings (called virtual moorings) following the recommendations by Wang et al. (2018).

The real multi-platform experiment (FaSt-SWOT[12]) will be conducted in the western Mediterranean Sea during the SWOT fast-sampling phase in 2023. For the design of FaSt-SWOT, we will follow the recommendations extracted from this study. In addition, codes developed in this task are available in GitHub, and they can be used by the SWOT Science Team to evaluate sampling strategies in other regions selected for the SWOT validation phase. These codes will remain open and free and will serve for future design of in situ multi-platform experiments.

10. Evaluation of a reconstruction method based on machine-learning techniques

10.1. Approach

The CTD pseudo-observational set-up used here is the reference configuration, in which CTD casts are separated by 10 km. The eNATL60 degraded daily outputs are used to obtain three data sets needed as inputs to the reconstruction model (Figure 69):

- First, it is necessary to generate pseudo-observations of temperature and salinity at the ocean surface every 5 days during the period of available model outputs. These pseudo-observations are obtained by linearly interpolating the model outputs on specific dates to the reference configuration grid. These dates are defined as the central date in a time window of 5 days (the reference configuration sampling duration is 4.3 days) for the period between 1 July 2009 and 30 September 2010. With this approximation, the pseudo-observations represent a stationary state of the ocean, i.e., they do not include the temporal variability of real in situ observations.
- Secondly, the spatial Optimal Interpolation (OI) algorithm is applied to the pseudo-observations obtaining the “Lower Quality Field”. Such a field receives this name as the Neural Network model tries to improve it. The interpolation grid has a horizontal resolution of 2 km and we assume a spatial correlation scale of 25 km.
- Lastly, a “Ground Truth” field is defined by linearly interpolating the model outputs to the OI grid. This will enable the definition of the reconstruction error and will be useful for making the algorithm learn.

[12] https://www.swot-adac.org/campaigns/fast-swot/

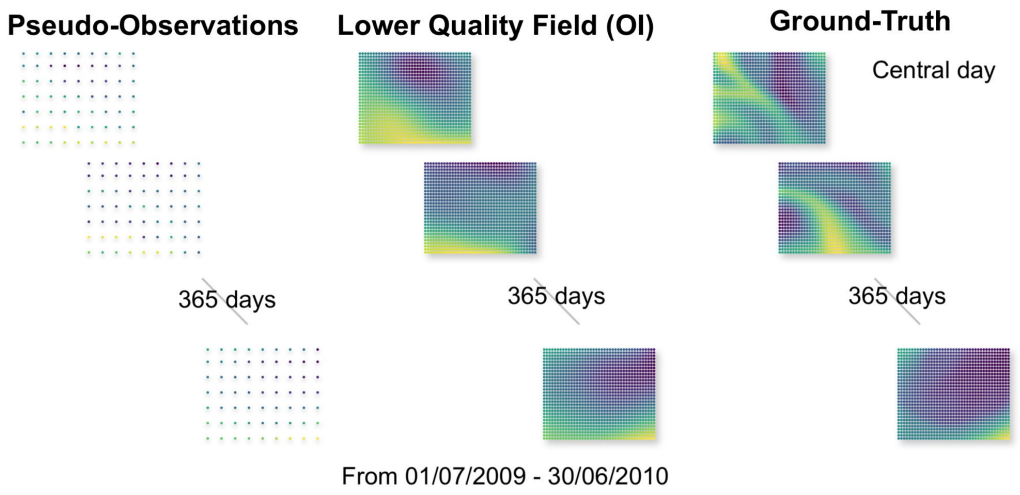

Figure 69: Representation of the three different data sets for the whole year needed for the training/validation/testing of the 4D-VarNet.

These three data sets are introduced into the Neural Network model, which from now on will be referred to simply as the model. They are split into three different groups depending on the period (Figure 70):

- The training set is used to adjust the model's parameters. These parameters are modified by the algorithm through iterative processes, they are the equivalent of the weights in the linear regression. One important aspect is that the number of parameters should never be greater than the quantity of data.
- The validation set is used to adjust the model's hyperparameters. Hyperparameters are tuned manually, for example at which rate does the Neural Network learn, i.e. the learning rate.
- The test set is then used to find the reconstruction and it has been kept unseen for the model during the whole process. This permits retrieving the true performance of the model and must coincide with the dates of reconstruction (1-5 September 2009).

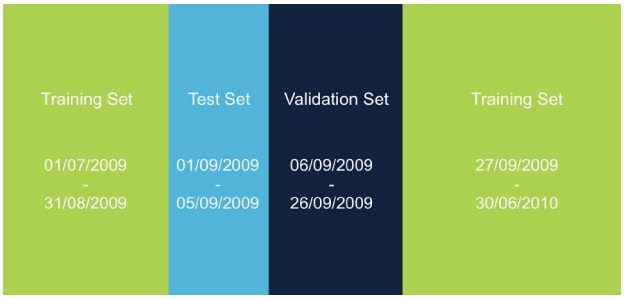

Figure 70: Temporal splitting of the datasets.

10.2. Analysis of the results

For the reconstructed sea surface temperature (SST) field we observe that globally the structure is not improved with 4D-VarNet (Figure 71), however the SST magnitude is increased and more similar to the Ground Truth. This results in a reduction of the root-mean-square error (RMSE) compared to the reconstruction with the spatial optimal interpolation (Table 10).

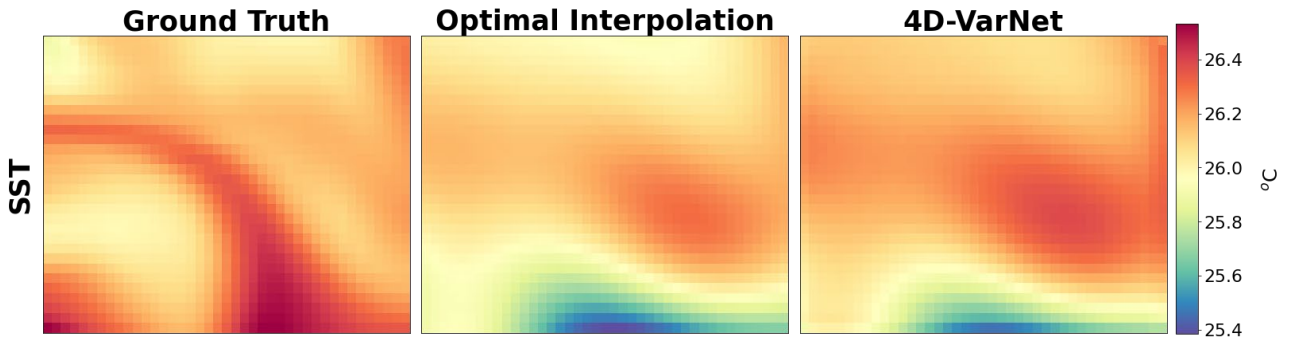

Figure 71: Sea Surface Temperature (SST) from the Ground Truth on 3 September 2009 and the reconstructed fields after applying the spatial optimal interpolation vs. the 4D-VarNet.

The reconstruction of sea surface salinity (SSS) through the 4D-VarNet allows the representation of two fronts not detected in the optimally interpolated field (Figure 72). In this case the RMSE is also reduced in comparison to the SSS reconstructed through the spatial optimal interpolation (Table 10). However, the improvement in SSS is lower than for the SST reconstruction.

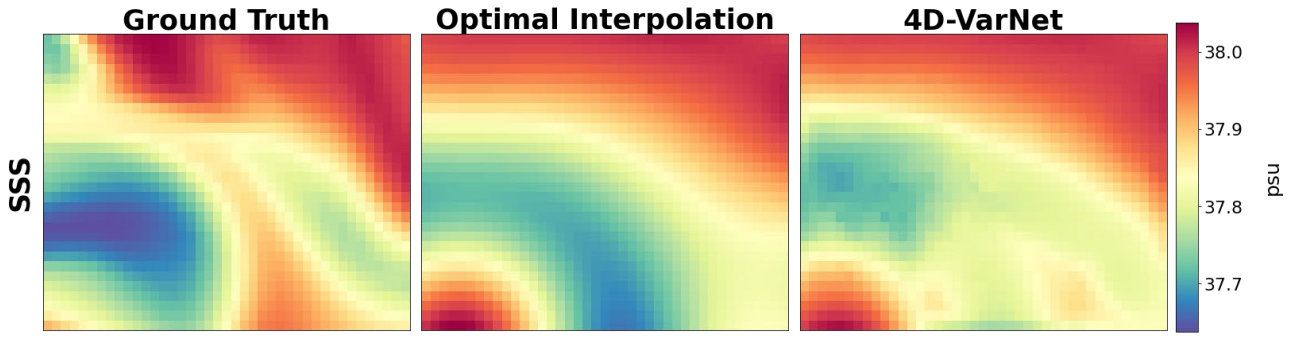

Figure 72: Sea Surface Salinity (SSS) from the Ground Truth on 3 September 2009 and the reconstructed fields after applying the spatial optimal interpolation vs. the 4D-VarNet.

Our results suggest that the 4D-VarNet may improve the reconstructions done through the spatial optimal interpolation. As shown in Table 10, the RMSE computed between reconstructed fields and the corresponding ocean truth on the central date of the time window is reduced after applying the 4D-VarNet. However, the reconstruction highly depends on the date considered, as well as on the quality of the optimally interpolated field. Hence, it is not assured that improvement can always be found.

Table 10: RMSE (ºC for SST) computed between reconstructed fields and the corresponding ocean truth on 3 September 2009, applying the spatial optimal interpolation vs. the 4D-VarNet method.

	Optimal Interpolation	4D-VarNet	Improvement
SST	1.00	0.89	11%
SSS	0.65	0.59	8.5%

10.3. Conclusions and perspectives

In the two cases analysed, the 4D-VarNet can improve the "Lower Quality Field". For SST the reconstruction introduces an increase of the magnitude more similar to the ocean truth, while the SSS reconstructed field captures two fronts not detected by the optimal interpolation. The reason for this improvement may be that the autoencoder captures better non-linearities. However, these results depend on the quantity and quality of the input data.

Currently, more advances are being done in order to include SWOT, nadir altimetry and SST satellite observations in order to compute directly the sea surface currents. This approach would enable deeper architectures to retrieve the dynamics as a greater quantity of data is available.

11. Evaluation of a reconstruction method based on model data assimilation

11.1. Approach

For this study, we use the eNATL60 model outputs as the Nature Run (NR). The NR is considered to represent the true ocean state evolution in this approach, and thus, it should represent the motions and scales of the ocean processes as good as possible. In OSSEs, the NR is used to generate pseudo-observations, that should resemble the real ones, and generate a similar impact in the model after assimilation (Halliwell et a. 2014). This NR is also used to validate the model after data assimilation. Differences between NR and CR can be seen in Figure 73, that illustrates the SLA mean fields on 4 September 2009 from the NR and CR models with the along-track pseudo-observations.

The WMOP model covers the western Mediterranean Sea, from Gibraltar in the west to Corsica and Sardinia in the East. Its capacity to ingest both large-scale observations all over the domain and high-resolution dense observations in a reduced region has been demonstrated in several studies (Hernández-Lasheras and Mourre, 2018, Hernández-Lasheras et al., 2021). Furthermore, for the forecast to perform optimally, high-resolution observations in a reduced area must be combined with large-scale observations in the whole domain to constrain the circulation.

We use simulated observations from different observing platforms (Section 6): sea level anomaly (SLA) from nadir altimetry, remote sensing sea surface temperature (SST), Argo temperature and salinity profiles and CTD observations in the reference configuration (Figures 74 and 75).

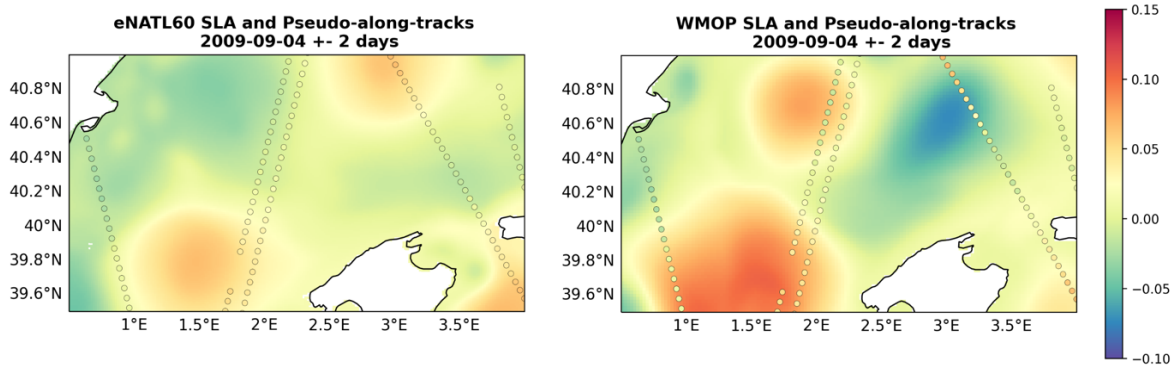

Figure 73. SLA mean fields on 4 September 2009 from the Nature Run (left) and Control Run (right) models with along-track pseudo-observations within a +- 2 days time window overplotted.

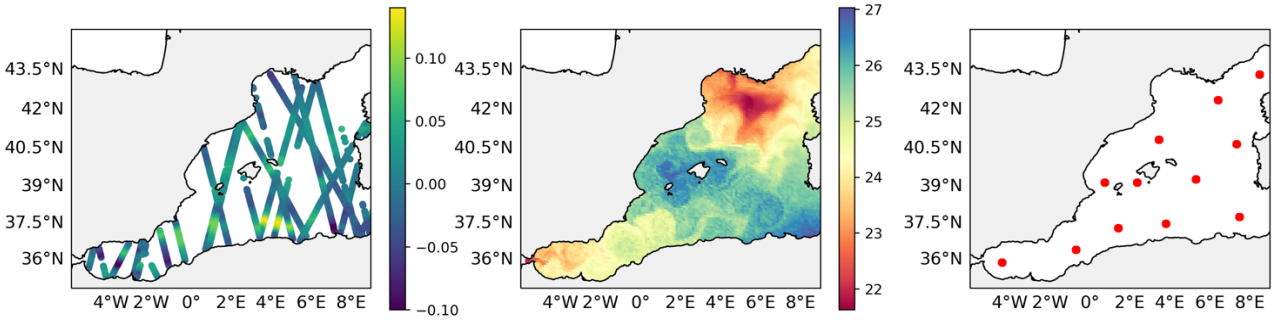

Figure 74. SLA in m (left), SST in ºC (center) and Argo position (right) of the pseud-observations assimilated on 4 September 2009.

Four experiments assimilating different datasets are conducted to evaluate the capability of the model to reconstruct the dynamic height and the surface circulation using CTD observations from the reference configuration:

- Experiment 1: control run (CR, no assimilation);
- Experiment 2: assimilation of SLA, SST and Argo (generic dataset used operationally);
- Experiment 3: assimilation of SLA, SST, Argo and CTDs;
- Experiment 4: assimilation of CTDs only.

For the two experiments assimilating SLA, SST and Argo (experiments 2 and 3), we start the simulation with a 3-day spin-up, starting on 2 September 2009 from the output of an analysis including assimilation of SLA, SST and Argo. Then, a second analysis is performed on 5 September (central day for the CTD sampling). All the CTD observations are considered as synoptic in the analysis.

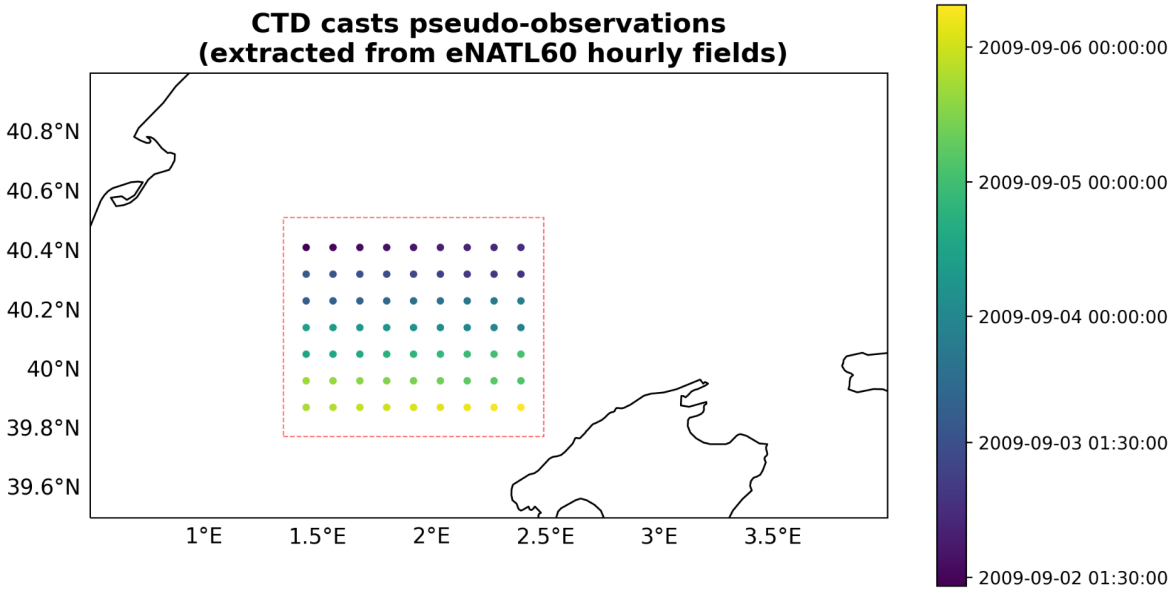

Figure 75. Area of the experiments and CTD cast position (color represent the time of the CTD cast).

11.2. Analysis of the results

The different WMOP data assimilation experiments are compared against the NR fields on 5 September 2009. We first evaluate the capability of the assimilation to reconstruct temperature and salinity 3D fields, by comparing the model forecast against the NR. The comparison is performed over a 3kmx3km grid including the CTD sampling region (red box in Figure 75), and down to 800 m depth. Figure 76 shows the normalized RMSD (nRMSD = $RMSD_{assim}$ / $RMSD_{CR}$). Values below 1 indicate an improvement due to the data assimilation. Figure 76 shows that the assimilation of SLA, SST and Argo (experiment 2) already leads to an improvement in comparison to the control run fields. A significant improvement is achieved when introducing only CTD observations into the system (experiment 4). The normalized RMSD is reduced around 40% both for temperature and salinity fields, and also for density. When assimilating SLA, SST and Argo in the bigger region and local high-resolution CTD pseudo-observations (experiment 3), the normalized RMSD is very similar to the values obtained for experiment 4, with a slight improvement for salinity. Note that all the simulations assimilating data (experiments 2, 3 and 4) reduce the RMSD with the NR fields compared to the control run simulation (experiment 1, no data assimilation). However, the bias (defined as the mean difference between WMOP and NR fields over each depth layer) is higher in deeper layers when including data assimilation (not shown). The difference between WMOP reconstructed temperature and salinity fields and the NR has a spatial structure also observed in the difference between the reconstructed dynamic height at the upper layer and the NR. Figure 77 shows the vertically averaged difference between the reconstructed temperature from experiments 1, 4 and 2 and the corresponding NR field, revealing a pattern similar to the difference in dynamic height at the upper layer (calculated from 3D density fields) between the WMOP experiments and the NR.

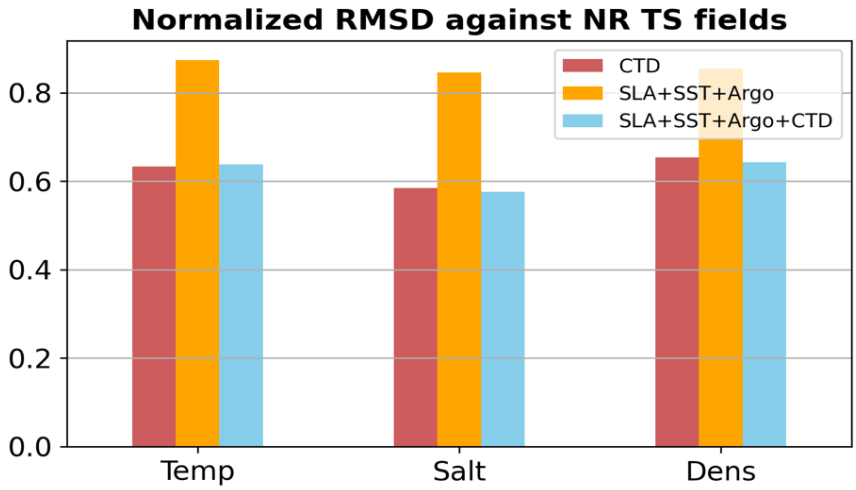

Figure 76. Root-mean-square difference (RMSD) between the reconstructed fields using WMOP data assimilation and the NR on the 5 of September, normalized by the RMSD of the CR with respect to the NR; for temperature, salinity and density fields in the CTD sampling region. Values below 1 indicate an improvement due to data assimilation.

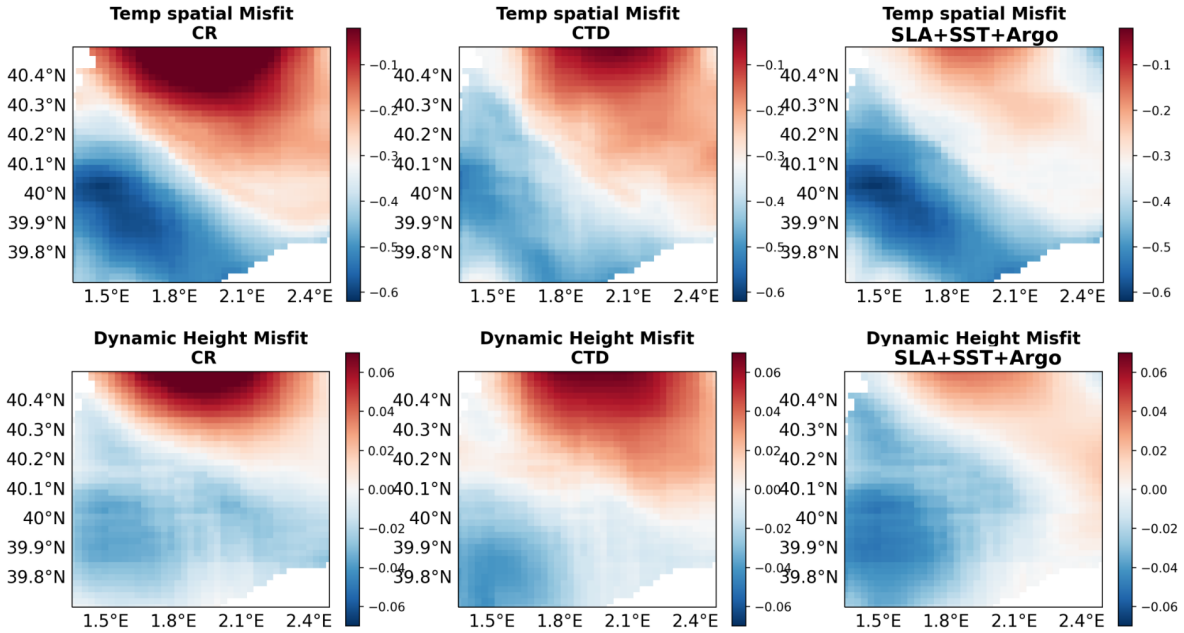

Figure 77. Top row: Spatial distribution of the vertically averaged difference between reconstructed temperature from experiments 1, 4 and 2, and the corresponding NR field. Bottom row: Difference between reconstructed and NR dynamic height at the upper layer (calculated from 3D density fields).

We then compare the reconstructed SLA and SST fields from each experiment to the NR, in the whole domain and in the CTD sampling region to evaluate the impact in each area. For both variables and in each region we interpolate the NR fields onto the WMOP grid. The comparison for SLA fields in the CTD sampling region is done through the bias (defined as the mean difference), RMSD, centred RMSD (cRMSD) and correlation coefficient (Table 11). The first three metrics are related by the following expression: $RMSD^2 = Bias^2 +$

cRMSD². The bias is significant in all experiments and increases with respect to the CR when we assimilate CTD pseudo-observations, while it decreases when only assimilating generic observations. The correlation increases for all data assimilative simulations. When only assimilating generic observations (SLA, SST, Argo) the correlation increases to 0.95, while using only CTD pseudo-observations slightly outperform the CR. The use of CTD together with generic pseudo-observations improves the reconstruction with respect to the CR, but gives a lower correlation than the generic experiment (0.87). The RMSD for all the experiments has a correspondence with the bias. The RMSD can be decomposed into bias and centred RMSD, which does not take into account this mean deviation. For the cRMSD the results reveal similar conclusions as for the correlation: the assimilation of CTD pseudo-observations (experiment 4) improves the reconstruction of the CR, which is further outperformed when including generic observations (experiment 3), while the best results are obtained when only assimilating SLA, SST and Argo (experiment 2). This can be summarized by Figure 78, where the normalized cRMSD over the whole domain and in the specific CTD sampling region has the lowest values for experiment 2.

Table 11. Bias, RMSD, cRMSD and correlation coefficient of the SLA fields in the CTD sampling region between the different simulation experiments and the NR. The first three metrics are related by the following expression: $RMSD^2 = Bias^2 + cRMSD^2$.

	Bias (m)	RMSD (m)	CRMSD (m)	Correlation
CR	-0.055	0.059	0.022	0.73
CTD	-0.063	0.065	0.018	0.75
SLA+SST+Argo	-0.044	0.045	0.011	0.95
SLA+SST+Argo+CTD	-0.057	0.058	0.013	0.87

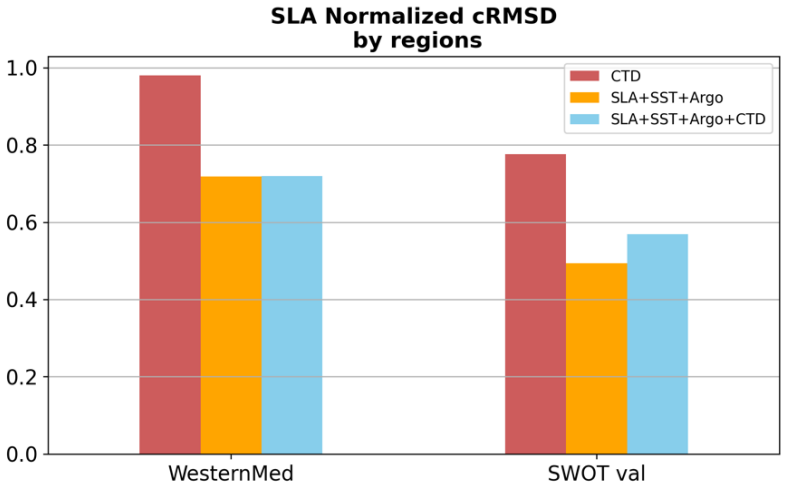

Figure 78. Centred RMSD between the reconstructed fields using WMOP data assimilation and the NR on the 5 of September, normalized by the centred RMSD of the CR with respect to the NR, for SLA in the whole domain and in the CTD sampling region.

In the case of SST the bias does not have a significant contribution to the RMSD (not shown) and we use the normalized RMSD metric for the comparison (Figure 79). In the whole modelling domain, the impact of

assimilating CTD pseudo-observations is very slight and the reduction of the RMSD with respect to the CR is mainly obtained with the assimilation of SST. Focusing on the CTD sampling region, assimilation of only CTD pseudo-observations leads to an improvement on the reconstruction, outperforming experiment 2 (assimilation of SLA, SST and Argo). When all the pseudo-observations are assimilated (experiment 4), the normalized RMSD is reduced with respect to the other two experiments.

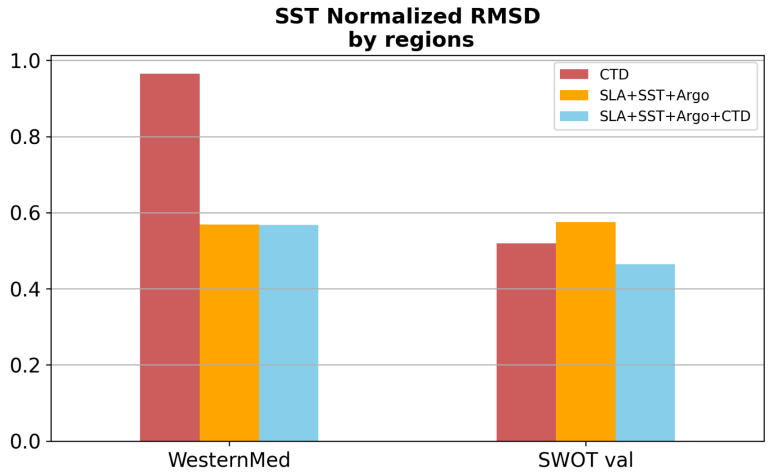

Figure 79. RMSD between the reconstructed fields using WMOP data assimilation and the NR on the 5 of September, normalized by the RMSD of the CR with respect to the NR; for SST in the whole domain and in the CTD sampling region.

We finally analyse the reconstructed SSH and mean currents in a wider region than the CTD sampling area (Figure 80). In this qualitative comparison we can observe the differences between CR and NR circulation patterns, not only in the sampling region but also in a wider area. A strong cyclonic eddy is detected west of Mallorca in both simulations, while an anticyclone is observed in the northern part but displaced from one simulation to the other. Assimilating pseudo-observations, the reconstructed fields still represent the two eddies. While in these cases the anticyclone in the northern part (40.8ºN, 2ºE) is not as intense as in the CR, it still generates an anticyclonic circulation in the northern part of the CTD sampling region that does not correspond with the eddy observed in the NR.

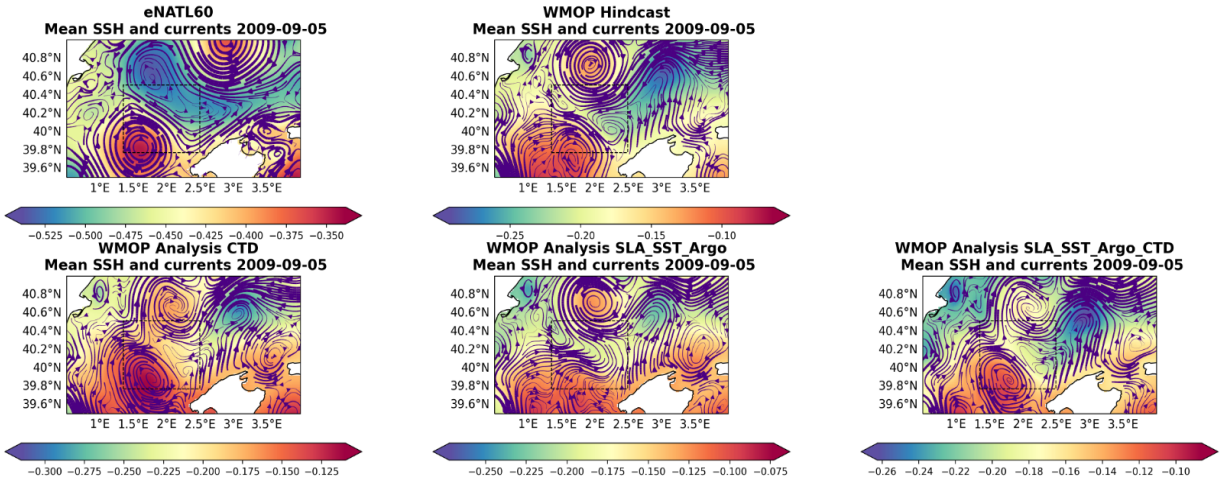

Figure 80. SSH and mean currents for the NR (top left), CR (top centre) and the three experiments assimilating different sets of pseudo-observations (bottom).

11.3. Conclusions and perspectives

The WMOP data assimilation system corrects the reconstructed fields of the control run, providing forecasts that are closer to the NR simulation. While the assimilation of only CTD pseudo-observations reduces the error for temperature, salinity and density 3D fields, the SLA reconstructed field has a higher error and a lower correlation than when using only generic observations (SLA, SST and Argo). The SSH from the assimilation analysis is coherent with the dynamic height computed from density fields obtained from temperature and salinity reconstructions. The discrepancy between the performance of the different experiments on the reconstruction of temperature and salinity fields vs. SLA may be related to the fact that the vertically averaged difference between reconstructed and NR T and S fields has a spatial structure (i.e., it is uneven along the domain) that impacts the reconstruction of dynamic height. These discrepancies still need to be further explored to be fully understood.

12. Mapping nadir altimetry using drifters through the MIOST tool

12.1. Approach

For this study, different experiments are performed (Table 12). In experiment 1 we use only nadir altimetry pseudo-observations. In experiment 2 altimetry pseudo-observations are merged with total horizontal currents derived from drifters. In this case we use 10% of the simulated drifters (extracted randomly), which is a number of drifters similar to the real density in the Mediterranean at present. In experiment 3 we merge nadir altimetry with 3 times the number of drifters used in experiment 2. For experiments 2 and 3 we use both the geostrophic and ageostrophic modes of the MIOST tool. We take as input the total horizontal currents derived from the simulated drifter trajectories. The algorithm separates the geostrophic and ageostrophic components of the drifter pseudo-observations.

Table 12: Summary table of the different experiments conducted to evaluate the MIOST technique. For the ageostrophic components, the temporal decorrelation scale is 2 days (T) and the spatial decorrelation scale is 500 km (L).

Experiments	Nadir altimetry	Drifters	Geostrophic component	Ageostrophic components (div + rot)
Experiment 1	All satellites	0	Yes	No
Experiment 2	All satellites	10% (~actual number of driters) u_tot, v_tot	Yes	Yes (L=500km, T=2days)
Experiment 3	All satellites	30% (~3x actual number of driters) u_tot, v_tot	Yes	Yes (L=500km, T=2days)

12.2. Analysis of the results

Comparison in SSH

First, MIOST reconstructions of SSH are analysed against the degraded native run (eNATL60). As in the collaborative project of the ocean data challenge[13], the RMSE-based score (RMSEs) is calculated for the whole domain and over the whole period (1 year), and is defined as:

$$RMSEs(t) = 1 - \frac{RMSE(t)}{RMS(SSH_{true})}$$

where RMS is the root mean square function and with:

$$RMSE(t) = \sqrt{\frac{1}{N}\sum_{i=1}^{N}(SSH_{reconstruction}(t,i) - SSH_{true}(t,i))^2}$$

where N is the number of grid points included in the study domain.

Table 13 shows the temporal average and temporal standard deviation of the RMSEs(t) calculated between SSH reconstructions and the native run (or ocean truth). The temporal standard deviation gives an insight on the temporal stability of the reconstruction. The addition of velocity data from drifters (experiments 2 and 3) slightly improves the mean RMSEs and its temporal stability with respect to experiment 1. Figure 81 shows the temporal evolution of the RMSE (non-normalized) for the three experiments. The three time series are similar, however the RMSE for the experiments with drifters (especially for experiment 3) is lower in some periods. For example, in the period between 1 July 2009 and 15 August 2009, in the months of November and December 2009, and at the end of the time series.

[13] https://github.com/ocean-data-challenges/2020a_SSH_mapping_NATL60

Table 13: Temporal average and temporal standard deviation of the RMSEs (μ(RMSEs) and σ(RMSEs), respectively) calculated between MIOST reconstructions of SSH and the native run for the three experiments.

Experiments	μ(RMSEs)	σ(RMSEs)
Experiment 1	0.940	0.027
Experiment 2	0.941	0.026
Experiment 3	0.942	0.025

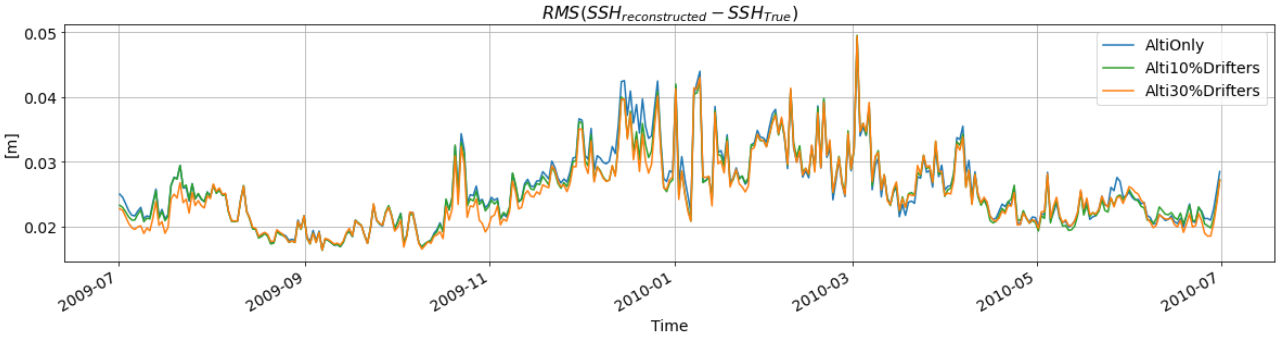

Figure 81: RMS of the differences between the reconstructed and native run SSH for each reconstructed day. The three lines represent the different experiments: in blue experiment 1, in green experiment 2 and in orange experiment 3.

The RMS of the differences is also calculated at each grid point of the domain taking into account all the time series:

$$RMSE(x,y) = \sqrt{\frac{1}{N_t}\sum_{t=1}^{N_t}(SSH_{reconstruction}(t,x,y) - SSH_{true}(t,x,y))^2}$$

where Nt is the number of time steps included in the time series. Figure 82 presents a spatial view of this RMSE(x, y) for the three experiments. The Alboran Sea and the Algerian coast are much more energetic areas than the northern part of the western Mediterranean basin; it is in these areas where the RMSE is higher for the three experiments, while it is relatively low for the rest of the domain. The contribution of drifters allows to better represent the eddy structure along the Algerian coast. At 37°N and 2°E in experiment 1 (Figure 82a) there is a structure with high RMSE, while for experiments 2 and 3 the RMSE is lower in this area (Figures 82b and c).

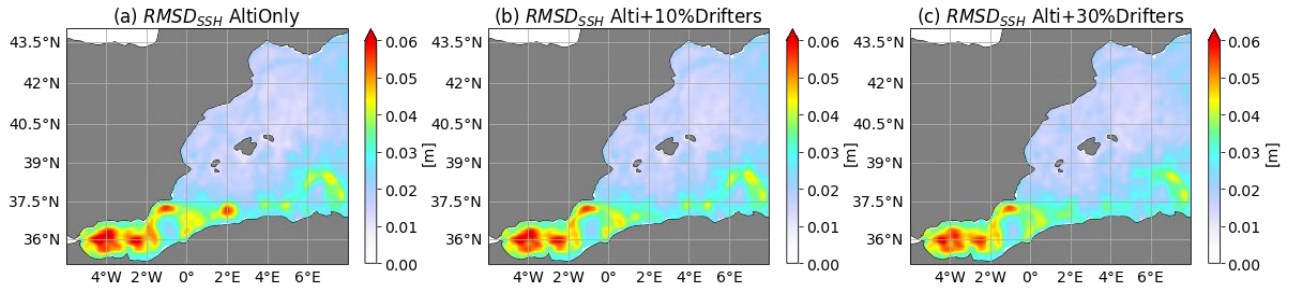

Figure 82: RMS of the differences between reconstructed and native run SSH fields at each grid point calculated over the time period for (a) experiment 1, (b) experiment 2 and (c) experiment 3.

Comparison in surface currents

The native run circulation on 4 February 2010 (Figures 83e and f) shows the energetic Algerian current along the coast and a meander around 2.5°E. The three MIOST experiments reconstruct the current along the coast and the meander (Figures 83a-c), however the intensity of this current west of 2.5°E is better reconstructed for the two experiments with drifters. On the other hand, the thickness of the current reconstructed by MIOST is larger compared to the thickness of the current in the ocean truth.

In the rest of the area, the circulation reconstructed from experiment 1 shows small-scale current structures with amplitudes up to 0.3-0.4 m/s. The eddy centred at 4°E, 38.5°N is reconstructed using only altimetry pseudo-observations, but it is slightly more intense (and closer to the ocean truth) in the experiments including drifters. The two small eddy structures centred at ~2.75°E, 38.5°N and ~2.25°E, 39°N in the ocean truth are slightly reconstructed by experiments 1 and 2, and more clearly visible in the reconstruction from experiment 3, even with lower magnitude than in the ocean truth.

The circulation on 9 February 2010, a few days after the circulation shown in Figure 83, presents the Algerian current and the meander, that has almost detached from the main current (Figure 84). Similar to the other date analysed, the MIOST experiments reconstruct an Algerian current that is wider and smoother than the native run. The intensity of the meander is better represented by the reconstructions including drifter data. Concerning the small-scale structures in the rest of the domain, the experiment with 10% of drifters (experiment 2) seems closer to the ocean truth than the two other experiments.

Qualitatively the drifter data seem to improve the surface current reconstruction, however the magnitude remains smoother. In this example of the Algerian current the velocity magnitude is better represented in the reconstructions including drifters, however, as the reconstructed Algerian current is wider than in the ocean truth, a point-by-point error will certainly be worse for these two experiments than for experiment 1 (using only altimetric pseudo-observations) which represents a less intense coastal current.

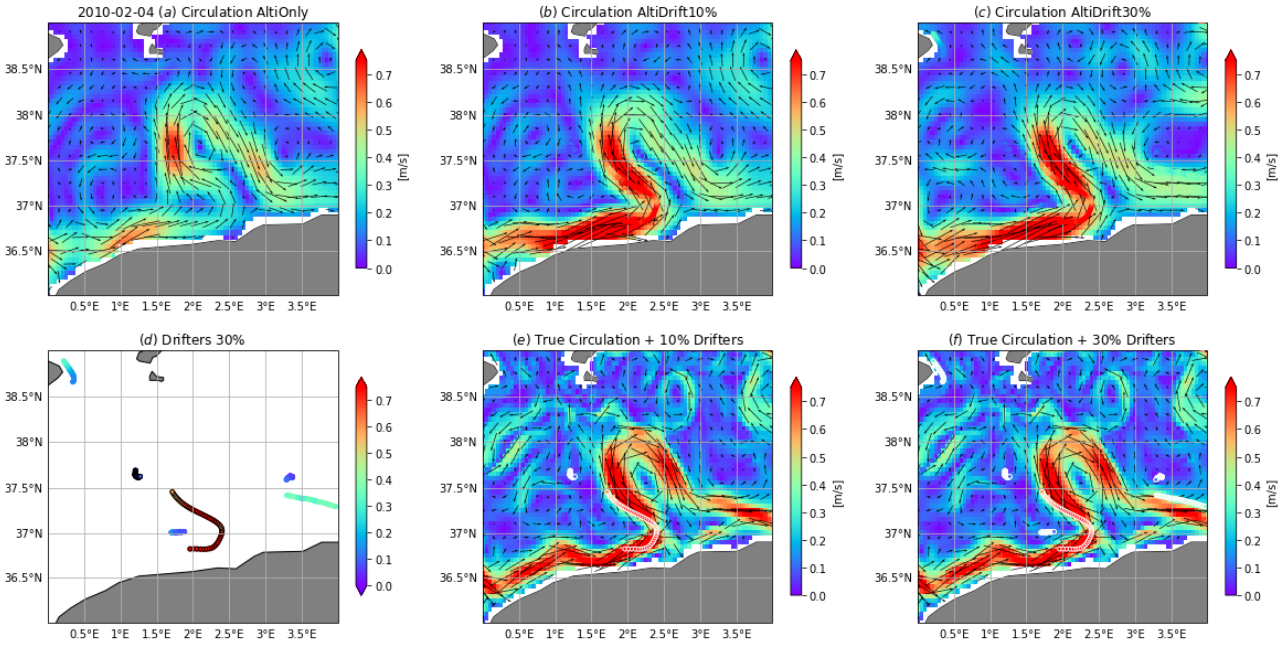

Figure 83: Circulation (black arrows represent the direction and color the magnitude of the surface currents) on 4 February 2010 reconstructed from (a) experiment 1, (b) experiment 2 and (c) experiment 3. Pannel (d) shows the 30% of drifters on the reconstruction date: the drifters whose points are circled in black are the common drifters between experiments 2 and 3. The last panels show the native run circulation (vectors and magnitude) on the reconstruction date and the drifters circled in white used for (e) experiment 2 and (f) experiment 3.

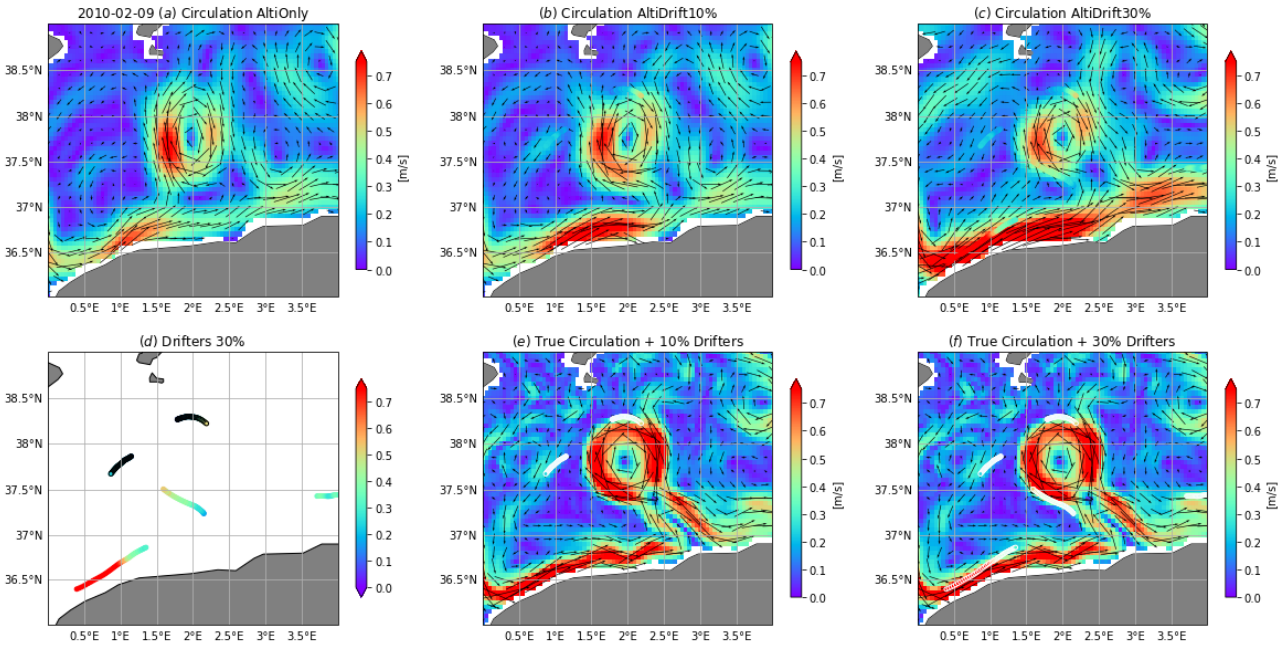

Figure 84: Circulation (black arrows represent the direction and color the magnitude of the surface currents) on 9 February 2010 reconstructed from (a) experiment 1, (b) experiment 2 and (c) experiment 3. Pannel (d) shows the 30% of drifters on the reconstruction date: the drifters whose points are circled in black are the common drifters between experiments 2 and 3. The last panels show the native run circulation (vectors and magnitude) on the reconstruction date and the drifters circled in white used for (e) experiment 2 and (f) experiment 3.

To continue the circulation analysis, we computed the rotary spectra from the reconstructed currents and the corresponding ocean truth. Rotary spectra decompose vector time series (e.g., current data) into clockwise and counter-clockwise components. This allows the detachment from the cartesian coordinate reference. These spectra were computed over the different areas highlighted in Figure 85. The selected regions represent areas with different oceanic variability: very intense for the three areas in the south and less intense for the area in the northeast. The EuroSea zoom zone (region including the CTD sampling of subtask 2.3.1) is smaller and with intermediate variability.

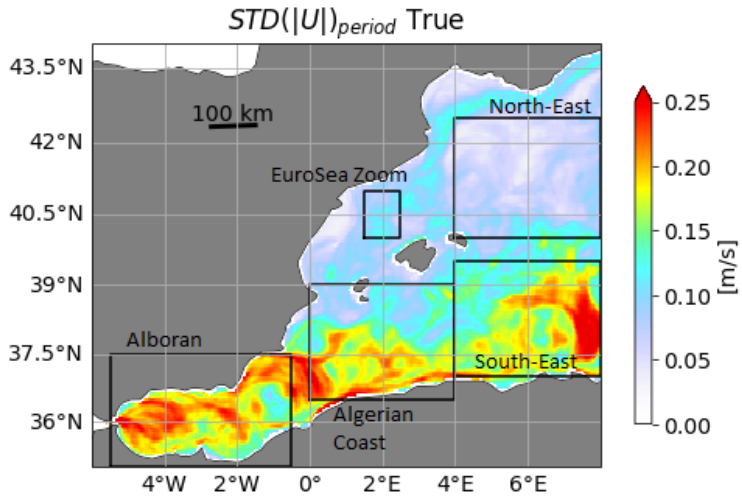

Figure 85: Standard deviation of the current magnitude computed over the whole period from the ocean truth. The black boxes are the areas in which energy spectra have been calculated.

Figure 86 shows the clockwise and counter-clockwise rotary spectrums calculated over each area (Figure 85). In all regions the clockwise and counter-clockwise energy for the three reconstructions is close to that of the "ocean truth" for scales larger than 15 days. Below 12 days the clockwise and counter-clockwise energy decreases abruptly for experiment 1, which is explained by construction because in MIOST the decorrelation time scale is about 10 days and finer scales are not reconstructed. The ageostrophic mode of MIOST used in the reconstructions with drifters can represent signals with temporal scales down to 2 days. We observe that there is more energy at scales smaller than 10 days for experiment 2, and even more energy for experiment 3 (almost with the same intensity as the ocean truth and even slightly higher at the Alboran Sea). This suggests that the more drifters are added, the higher is the energy at high temporal frequencies. MIOST, and in particular the ageostrophic mode, allows to reconstruct structures with faster time scales than altimetry alone. But it is likely that the MIOST reconstruction at time scales below 10 days adds noise and/or misplaces structures.

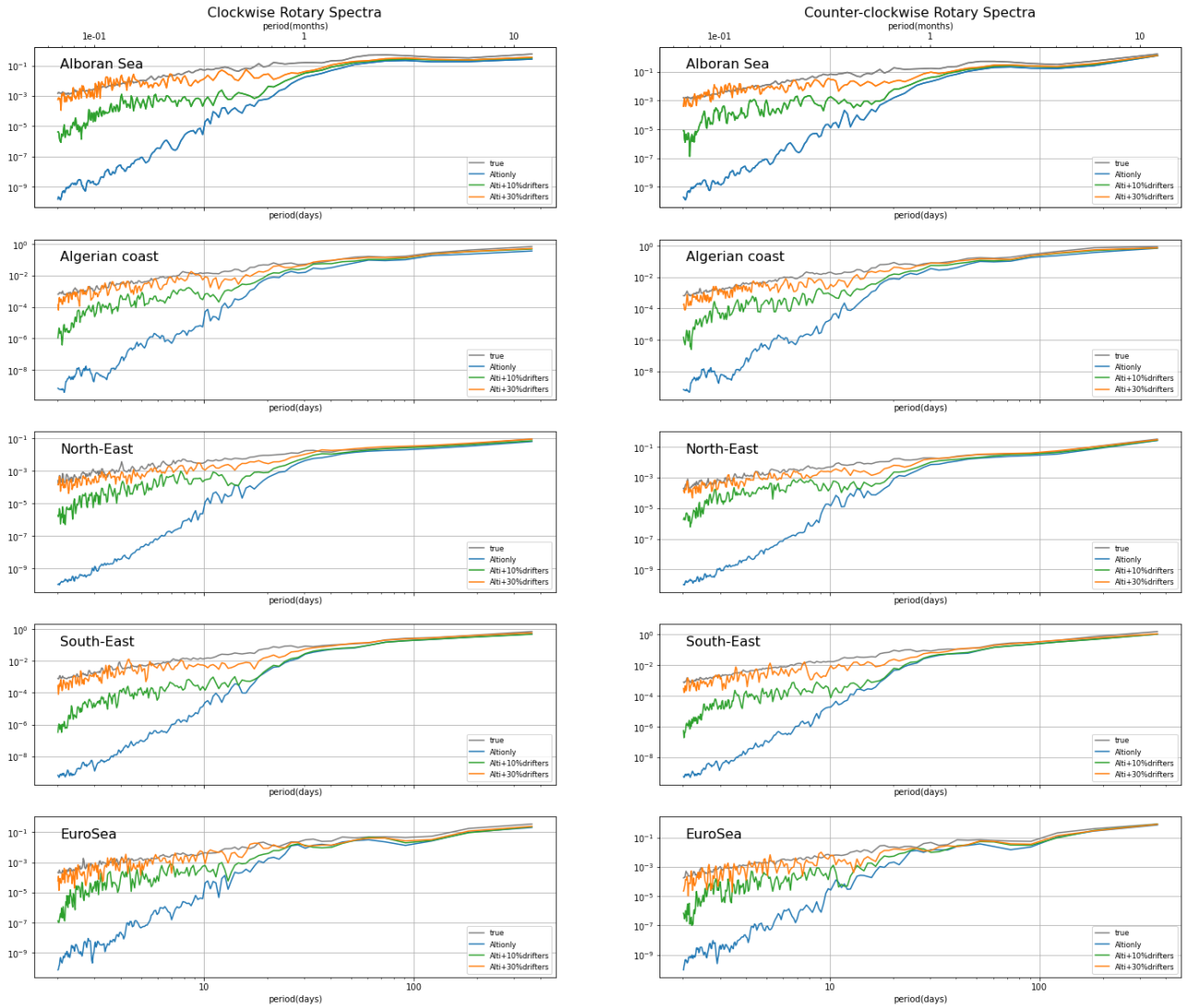

Figure 86: (left) Clockwise and (right) counter-clockwise rotary spectrum of the total surface currents from the MIOST experiments and ocean truth calculated over the areas shown in Figure 85. From top to bottom: the Alboran Sea, the Algerian coast, the North-East area, the South-East area and the EuroSea zoom area. In each pannel the spectrum of the ocean truth is shown in grey, the spectrum of experiment 1 is shown in blue, the spectrum of experiment 2 in green and the spectrum of experiment 3 in orange.

Finally, the RMS of the differences is also calculated for the magnitude of total surface currents at each grid point of the domain taking into account data over the temporal period:

$$RMSE(x,y) = \sqrt{\frac{1}{N_t}\sum_{t=1}^{N_t}(|U_{reconstruction}(t,x,y)| - |U_{true}(t,x,y)|)^2}$$

where Nt is the number of temporal steps in the considered period. In maps of RMSE(x, y) (Figure 87) we observe higher values in areas of higher variability (see Figure 85), while the three experiments represent similar patterns and the differences between them are small.

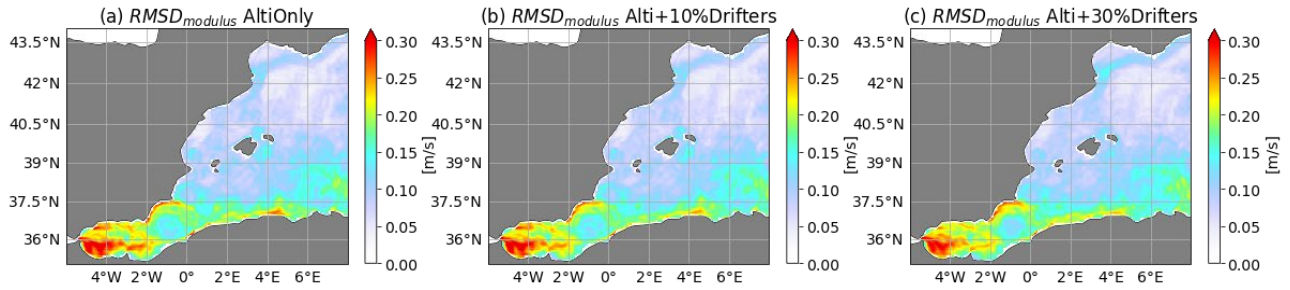

Figure 87: RMS of the differences between the reconstructed surface current magntiude and the ocean truth for (a) experiment 1, (b) experiment 2 and (c) experiment 3.

To analyse the contribution of drifters on the RMSE(x, y), we compute the %RMSE(x, y) defined as:

%RMSE(x, y) = 100*[RMSEexp_drifters(x, y) - RMSEexp1(x, y)] / RMSEexp1(x, y),

where RMSEexp_drifters(x, y) is the RMSE(x, y) calculated for the experiments with drifters (experiment 2 or 3). When this percentage is negative the contribution of drifters improves the RMSE(x, y), while when it is positive the contribution of drifters degrades the RMSE(x, y) compared to the experiment using only altimetry data (experiment 1).

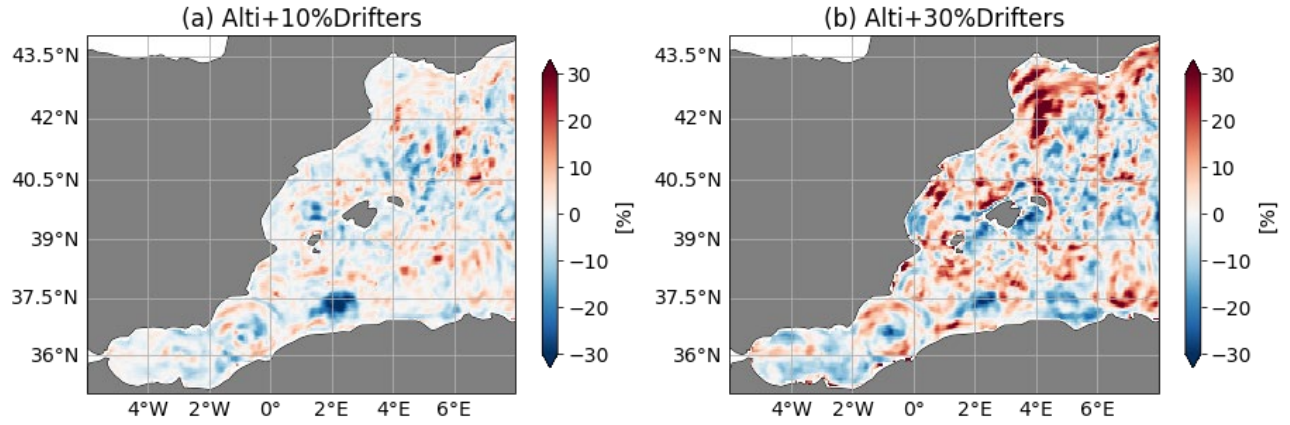

Figure 88: %RMSE(x, y) calculated for the surface current magnitude reconstructed in (a) experiment 2 and (b) experiment 3.

Figure 88a shows more areas of improvement than deterioration. In particular, the eddy structure around 2°E, 37.5°N is better represented in current magnitude for the reconstruction of experiment 2, while the area of lower variability at the northeast of the basin (Figure 85) appears more deteriorated. For the reconstruction of experiment 3 (Figure 88b), the deterioration areas are more intense and widespread, especially in the Gulf of Lyon. However, the improved areas are also slightly more intense, for example in the Alboran Sea. This point-by-point comparison shows that the reconstruction with 30% of drifters (experiment 3) creates total currents that are not in agreement with the ocean truth. This is probably due to the fact that there is too much signal projected on the ageostrophic modes with this reconstruction, which is not the case of the reconstruction with 10% of drifters (experiment 2).

12.3. Conclusions and perspectives

The addition of drifter data to the MIOST reconstruction slightly improves the SSH field on average over the whole area. In particular, the improvement occurs in specific regions. For example, the contribution of drifters improves the SSH signal of the eddy detected north of the Algerian coast (not observed by altimetry). However, the SSH signal is slightly degraded in areas with less intense activity.

Concerning the reconstruction of total currents, the improvement due to the contribution of drifters is more difficult to quantify. Qualitatively, structures such as the Algerian current and the detached eddy are clearly improved by the addition of drifters in the examples in February 2010. In addition, in these examples, smaller, less intense eddy structures have a similar size and position than in the ocean truth, while the intensity is consistent but smoother. However, although the Algerian current intensity has been improved, this current is larger in the MIOST reconstruction with drifters than in the native run, which increases the RMS of the errors. And in fact, the overall point-by-point RMSE shows more degraded areas in comparison to the geostrophic currents reconstructed only with SLA data, which are less intense than the total currents reconstructed merging altimetric SLA with drifters. The point-by-point differences seem a severe quantification for the total currents and not fully appropriate for their evaluation. It would be interesting to work on new structure-based diagnostics for currents. For example, quantify the intensity of the Algerian current and its positioning, as well as the meanders that form and detach, to better account for the contribution of drifters.

Besides, the study of the temporal rotary spectra at different areas shows that the energy at time scales smaller than 10 days is added by drifters and the experiment with 30% of drifters reaches the level of energy of the ocean truth. Thus, consistent with the qualitative better reconstruction of the Algerian current and associated eddies, the use of drifters adds accurate signal in the spectra. However, in less energetic areas the use of 30% of drifters may add some noise. It means that when increasing the number of drifters used for the mapping (3 times the actual number of drifters in this case), we should also adapt the parameters of our reconstruction.

Note also that the comparison of currents with the native run was done with a spatially degraded version averaged over one day. The variability of currents over a day is not negligible and therefore the difference between the reconstructed currents and the degraded ocean truth contains the differences between the instantaneous field at 12:00 (reconstruction time) and the ocean truth averaged field. In future work we should make all the comparisons with the original high-resolution native run.

To conclude, the use of drifters will contribute to the reconstruction of SSH and currents and will be thus useful for SWOT validation. To reach this objective we should define new metrics rather than point-by-point RMSE to validate small-scale structures such as eddies or coastal currents. For instance, we could compare front or eddy characteristics (radius, intensity…). We should also continue working on MIOST parameterizations.

Conclusions

Deliverable 2.3 presents the study conducted in Task 2.3 of the EuroSea project. First, we have analysed different sampling strategies aimed to reconstruct fine-scale currents (~20 km), such as those that will be conducted to validate SWOT satellite observations. From this evaluation we can provide recommendations for the design of in situ experiments that share the same objective. In the Mediterranean study region, distinct strategies provide reconstructions similar to the ocean truth and, hence, they are good options. A good compromise considering the advantages of each sampling strategy is the reference configuration, consisting of CTD casts separated by 10 km and down to 1000 m, sampling the domain in 4.3 days. A faster valid alternative is to release the rosette CTD casts down to 500 m depth (3.1 days). An even faster valid strategy consists of changing the rosette CTD casts for an underway CTD with a horizontal spacing between profiles of 6 km and a vertical extension of 500 m (1.8 days); the scores in this case are higher than for the configuration with rosette CTD casts down to 500 m depth. A sampling strategy not appropriate for our objective is the configuration consisting of an underway CTD sampling one profile every 2.5 km and down to 200 m. Regarding seasonality, the reference configuration is a sampling strategy that provides reconstructions similar to the ocean truth in summer and in winter.

In the Atlantic study region, sampling strategies consisting of CTD profiles down to 1000 m depth provide reconstructions with higher scores than the strategies that only sample the water column down to 500 m depth. The geostrophic velocities reconstructed from the strategies that sample the upper 1000 m depth have a magnitude similar to the ocean truth, while the strategies that only sample the upper 500 m depth reconstruct a magnitude ~50% smaller. Different horizontal spacings between CTD profiles provide fine-scale current reconstructions with high scores. The reference configuration, which considers a distance between casts of 10 km, is a good compromise between horizontal resolution, spatial coverage and sampling duration. The configuration consisting of an underway CTD sampling one profile every 2.5 km and down to 200 m reconstructs the geostrophic velocity field with an underestimation of 60% in magnitude with respect to the ocean truth; this is the strategy with the lowest scores also for the Atlantic region. The analysis of seasonality suggests that the reference configuration, which provides good reconstructions in summer, does not capture the structures present in the region of study in winter.

The evaluation of different sampling strategies was done applying an advanced version of the spatial optimal interpolation used in field experiments, which also includes the temporal variability of the observations. An extensive analysis to find the optimal temporal correlation scale has been conducted, finding that a scale of 10 days gives similar reconstructions than using a scale of 2 days. In the same context, we have tested two additional reconstruction methods. A machine-learning technique has been evaluated to reconstruct surface salinity and temperature fields. A slight improvement has been detected with respect to the spatial optimal interpolation which motivates further development of this approach. The second reconstruction method is based on model data assimilation. Four experiments have been simulated: (1) no data assimilation, (2) assimilation of SLA, SST and Argo, (3) assimilation of SLA, SST, Argo and CTD, and (4) assimilation of only CTD. The assimilation of data improves the reconstruction of 3D temperature and salinity fields with respect to the simulation with no data assimilation. The experiments that provide more similar reconstructions to the ocean truth are those including CTD pseudo-observations. Regarding SLA, the centred RMSE metric shows that the best reconstruction is obtained for the experiment only assimilating SLA, SST and Argo. For SST we detect differences in the two regions analysed. In the whole modelling domain, the decrease of the normalized RMSD is obtained when assimilating SST. In the CTD sampling region, the two experiments

including CTD pseudo-observations provide better reconstructions of SST. The simulation assimilating all data (SLA, SST, Argo and CTD) reconstructs the SST field more similar to the ocean truth.

Finally, we have evaluated the MIOST reconstruction technique to map nadir altimetry using drifters. The inclusion of simulated drifters introduces slight improvements in the reconstruction of SSH over the whole area. In particular, the improvement is observed in specific structures such as the Algerian current and the eddies detected near the current. In less energetic areas the SSH signal is slightly degraded when using drifters. Regarding the reconstructed circulation, we observe a qualitative improvement in the structures mentioned before. However, differences in the size/position of these features increase the point-by-point RMSE. In the whole region this metric shows more degraded areas when including drifters in comparison to the geostrophic currents reconstructed only from SLA data, while these currents are less energetic than the total currents reconstructed when including drifters. The RMSE metric is not appropriate for this evaluation and in future work we will explore structure-based diagnostics. Indeed, promising results are obtained from the spectral analysis: the energy at time scales smaller than 10 days is added by drifters, and the experiment tripling the actual number of drifters reaches a level of energy similar to the ocean truth. Note that when increasing the actual number of drifters the parameters of the reconstruction need to be adapted to account for additional noise. In conclusion, the merging of nadir altimetry with drifters can improve the reconstruction of SSH and surface currents and will be thus useful for SWOT validation. New metrics based on the analysis of structures are more appropriate than the point-by-point RMSE to validate features such as eddies or coastal currents. We should also continue working on MIOST parameterizations.

Availability of data and codes

- The codes developed in subtask 2.3.1 to evaluate different sampling strategies are published in GitHub: https://github.com/bbarcelollull/EuroSea_subTask_2.3.1
- The dataset generated in subtask 2.3.1 of the EuroSea project is published at Zenodo: https://doi.org/10.5281/zenodo.6798018
- The codes to simulate observations of SWOT, nadir altimetry and drifters are available at: https://github.com/ocean-next/EUROSEA.git
- Simulated observations of SWOT: https://github.com/ocean-next/EUROSEA/blob/main/swot_pseudoobs.md
- Simulated observations of nadir altimetry: https://github.com/ocean-next/EUROSEA/blob/main/nadir_alongtrack.md
- Simulated observations of drifters: https://github.com/ocean-next/EUROSEA/blob/main/lagrangian_traj.md

References

Aguiar, E., Mourre, B., Juza, M., Reyes, E., Hernández-Lasheras, J., Cutolo, E., Mason, E., Tintoré, J., 2019. Multi-platform model assessment in the Western Mediterranean Sea: impact of downscaling on the surface circulation and mesoscale activity. Ocean Dynamics doi:https://doi.org/10.1007/s10236-019-01317-8 Multi-platform.

Ardhuin, F., Brandt, P., Gaultier, L., Donlon, C., Battaglia, A., Boy, F., Casal, T., et al., 2019. « SKIM, a Candidate Satellite Mission Exploring Global Ocean Currents and Waves ». Frontiers in Marine Science 6: 209. https://doi.org/10.3389/fmars.2019.00209.

Barceló-Llull, B., Sangrà, P., Pallàs-Sanz, E., Barton, E. D., Estrada-Allis, S. N., Martínez-Marrero, A., Aguiar-González, B., Grisolía, D., Gordo, C., Rodríguez- Santana, A., Marrero-Díaz, A. & Arístegui, J., 2017. Anatomy of a subtropical intrathermocline eddy. Deep-Sea Res., 124, 126-139, DOI: http://dx.doi.org/ 10.1016/j.dsr.2017.03.012

Barceló-Llull, B., Pascual, A., et al., 2018. PRE-SWOT Cruise Report. Mesoscale and sub-mesoscale vertical exchanges from multi-platform experiments and supporting modeling simulations: anticipating SWOT launch (CTM2016-78607-P). 138 pp. http://dx.doi.org/10.20350/digitalCSIC/8584

Barceló-Llull, B., Pascual, A., Sánchez-Román, A., Cutolo, E., d'Ovidio, F., Fifani, G., Ser-Giacomi, E., Ruiz, S., Mason, E., Cyr, F., Doglioli, A., Mourre, B., Allen, J.T., Alou-Font, E., Casas, B., Díaz-Barroso, L., Dumas, F., Gómez-Navarro, L., Muñoz, C., 2021. Fine-Scale Ocean Currents Derived From in situ Observations in Anticipation of the Upcoming SWOT Altimetric Mission. Front. Mar. Sci. 8:679844. doi: 10.3389/fmars.2021.679844

Beauchamp, M., Fablet, R., Ubelmann, C., Ballarotta, M., Chapron, B., 2020. Intercomparison of Data-Driven and Learning-Based Interpolations of Along-Track Nadir and Wide-Swath SWOT Altimetry Observations. Remote Sens. 12(22), 3806; https://doi.org/10.3390/rs12223806

Bouffard, J., Pascual, A., Ruiz, S., Faugère, Y., Tintoré, J., 2010. Coastal and mesoscale dynamics characterization using altimetry and gliders: A case study in the Balearic Sea, J. Geophys. Res., 115, C10029, doi:10.1029/2009JC006087.

Bretherton, F.P., Davis, R.E., Fandry, C.B., 1976. A technique for objective analysis and design of oceanographic experi- ments applied to MODE-73. Deep-Sea Res. Oceanogr. Abstr., 23, 559–582, doi:10.1016/0011-7471(76)90001-2.

Brodeau, L., Le Sommer, J., Albert, A., 2020. ocean-next/eNATL60: Material describing the set-up and the assessment of NEMO-eNATL60 simulations (Version v1). Zenodo. http://doi.org/10.5281/zenodo.4032732

Carrassi, A., Bocquet, M., Bertino, L., Evensen, G., 2018. Data assimilation in the geosciences: An overview of methods, issues, and perspectives. WIREs Clim Change. 9:e535. https://doi.org/10.1002/wcc.535

Carrere, L., Lyard, F., Cancet, M., Guillot, A., Picot, N., 2016. « FES 2014, a new tidal model—Validation results and perspectives for improvements ». In Proceedings of the ESA living planet symposium, 9-13.

Ciani, D., Charles, E., Buongiorno Nardelli, B., Rio, M.-H., Santoleri, R., 2021. « Ocean Currents Reconstruction from a Combination of Altimeter and Ocean Colour Data: A Feasibility Study ». Remote Sensing 13 (12): 2389. https://doi.org/10.3390/rs13122389.

Davis, R.E., Objective mapping by least square fitting, J. Geophys. Res., 90(C3), 4773-4777, 1985.

d'Ovidio, F., Pascual, A., Wang, J., Doglioli, A.M., Jing, Z., Moreau, S., Grégori, G., Swart, S., Speich, S., Cyr, F., Legresy, B., Chao, Y., Fu, L., Morrow, R.A., 2019. Frontiers in Fine-Scale in situ Studies: Opportunities During the SWOT Fast Sampling Phase. Front. Mar. Sci. 6:168. doi: 10.3389/fmars.2019.00168

Escudier, R., Bouffard, J., Pascual, A., Poulain, P.-M., Pujol, M.-I., 2013. Improvement of coastal and mesoscale observation from space: Application to the northwestern Mediterranean Sea, Geophys. Res. Lett., 40, doi:10.1002/grl.50324.

Escudier, R., Clementi, E., Omar, M., Cipollone, A., Pistoia, J., Aydogdu, A., Drudi, M., Grandi, A., Lyubartsev, V., Lecci, R., Cretí, S., Masina, S., Coppini, G., & Pinardi, N., 2020. Mediterranean Sea Physical Reanalysis (CMEMS MED-Currents) (Version 1) set. Copernicus Monitoring Environment Marine Service (CMEMS). https://doi.org/10.25423/CMCC/MEDSEA_MULTIYEAR_PHY_006_004_E3R1

Fablet, R., Le Sommer, J., Molines, J.M., Drumetz, L., Rousseau, F., Chapron, B., 2019. Learning Differential Transport Operators for the Joint Super-Resolution of Sea Surface Tracers and Prediction of Subgrid-Scale Features, IGARSS 2019 - 2019 IEEE International Geoscience and Remote Sensing Symposium, Yokohama, Japan, pp. 7916-7919, doi: 10.1109/IGARSS.2019.8900571.

Fablet, R., Chapron, B., Drumetz, L., Mémin, E., Pannekoucke, O., et al., 2021. Learning Variational Data Assimilation Models and Solvers. Journal of Advances in Modeling Earth Systems American Geophysical Union, 13, pp.article n° e2021MS002572. doi:10.1029/2021MS002572ff.hal-02906798f

Fu, L.-L., and Ferrari, R., 2008. Observing oceanic submesoscale processes from space. EOS Trans. AGU 89:488. doi: 10.1029/2008EO480003

Fu, L.-L., and Ubelmann, C., 2014. On the transition from profile altimeter to swath altimeter for observing global ocean surface topography. J. Atmos. Ocean. Technol. 31, 560–568. doi: 10.1175/JTECH-D-13-00109.1

Gasparin, F., Guinehut, S., Mao, C., Mirouze, I., Rémy, E., King, R.R., Hamon, M., Reid, R., Storto, A., Le Traon, P.-Y., Martin, M.J., Masina, S., 2019. Requirements for an Integrated in situ Atlantic Ocean Observing System From Coordinated Observing System Simulation Experiments. Front. Mar. Sci. 6:83. doi: 10.3389/fmars.2019.00083

Gomis, D., Ruiz, S., Pedder, M., 2001. Diagnostic analysis of the 3D a geostrophic circulation from a multivariate spatial interpolation of CTD and ADCP data. Deep- Sea Res. 48, 269–295.

Hernández-Lasheras, J., Mourre, B., 2018. Dense ctd survey versus glider fleet sampling: comparing data assimilation performance in a regional ocean model west of sardinia. Ocean Science 14. doi:10.5194//os-14-1069- 2018.

Hernandez-Lasheras, J., Mourre, B., Orfila, A., Santana, A., Reyes, E., & Tintoré, J., 2021. Evaluating high-frequency radar data assimilation impact in coastal ocean operational modelling. Ocean Science, 17(4), 1157-1175.

Juza, M., Mourre, B., Renault, L., Gómara, S., Sebastián, K., Lora, S., Beltran, J.P., Frontera, B., Garau, B., Troupin, C., Torner, M., Heslop, E., Casas, B., Escudier, R., Vizoso, G., Tintoré, J., 2016. SOCIB operational ocean forecasting system and multi-platform validation in the western Mediterranean Sea, J. Oper. Oceanogr., 9 :sup1, s155-s166, doi: 10.1080/1755876X.2015.1117764

Le Guillou, F., Metref, S., Cosme, E., Ubelmann, C., Ballarotta, M., Le Sommer, J., & Verron, J., 2021. Mapping Altimetry in the Forthcoming SWOT Era by Back-and-Forth Nudging a One-Layer Quasigeostrophic Model, Journal of Atmospheric and Oceanic Technology, 38(4), 697-710. Retrieved May 25, 2022, from https://journals.ametsoc.org/view/journals/atot/38/4/JTECH-D-20-0104.1.xml

Le Traon, P.-Y., 1990. A method for optimal analysis of fields with spatially-variable mean. J. Geophys. Res., 95, 13 543–13 547, doi:10.1029/JC095iC08p13543.

Lopez-Radcenco, M., Pascual, A., Gomez-Navarro, L., Aissa-El-Bey, A., Fablet, R. Analog Data Assimilation for Along-Track Nadir and Swot Altimetry Data in the Western Mediterranean Sea, IGARSS 2018 - 2018 IEEE International Geoscience and Remote Sensing Symposium, Valencia, 2018, pp. 7684-7687, doi: 10.1109/IGARSS.2018.8519089.

Lusch, B., Kutz, J.N., Brunton, S.L., 2018: Deep learning for universal linear embeddings of nonlinear dynamics, Nat Commun 9, 4950 https://doi.org/10.1038/s41467-018-07210-0

Manucharyan, G.E., Siegelman, L., Klein, P., 2021. A deep learning approach to spatiotemporal sea surface height interpolation and estimation of deep currents in geostrophic ocean turbulence. Journal of Advances in Modeling Earth Systems, 13, e2019MS001965. https://doi.org/10.1029/2019MS001965

Mason, E., and Pascual, A., 2013. Multiscale variability in the Balearic Sea: An altimetric perspective, J. Geophys. Res. Oceans, 118, 3007– 3025, doi:10.1002/jgrc.20234.

Melnichenko, O., Hacker, P., Maximenko, N., Lagerloef, G., Potemra, J., 2014. Spatial Optimal Interpolation of Aquarius Sea Surface Salinity: Algorithms and Implementation in the North Atlantic. J. Atmos. Oceanic Technol., 31, 1583–1600, https://doi.org/10.1175/JTECH-D-13-00241.1.

Morrow, R., Fu, L.-L., Ardhuin, F., Benkiran, M., Chapron, B., Cosme, E., d'Ovidio, F., Farrar, J.T., Gille, S.T., Lapeyre, G., Le Traon, P.-Y., Pascual, A., Ponte, A., Qiu, B., Rascle, N., Ubelmann, C., Wang, J., Zaron, E.D., 2019. Global Observations of Fine-Scale Ocean Surface Topography With the Surface Water and Ocean Topography (SWOT) Mission. Front. Mar. Sci. 6:232. doi: 10.3389/fmars.2019.00232

Mourre, B., Aguiar, E., Juza, M., Hernandez-Lasheras, J., Reyes, E., Heslop, E., Escudier, R., Cutolo, E., Ruiz, S., Mason, E., Pascual, A., Tintoré, J., 2018. Assessment of High-Resolution Regional Ocean Prediction Systems Using Multi-Platform Observations: Illustrations in the Western Mediterranean Sea. New Frontiers in Operational Oceanography, 663– 694, doi:10.17125/gov2018.ch24.

Pascual, A., Buongiorno-Nardelli, B., Larnicol, G., Emelianov, M., Gomis, D., 2002. A case of an intense anticyclonic eddy in the Balearic Sea (western Mediterranean). J. Geophys. Res. 107 (C11), 3183. doi:10.1029/2001JC000913.

Pascual, A., Gomis, D., Haney, R. L., and Ruiz, S., 2004. A quasigeostrophic analysis of a meander in the palamós canyon: vertical velocity, geopotential tendency, and a relocation technique. J. Phys. Oceanogr. 34, 2274–2287. doi: 10.1175/1520-0485(2004)034<2274:AQAOAM>2.0.CO;2

Pascual, A., Ruiz, S., Olita, A., Troupin, C., Claret, M., Casas, B., Mourre, B., Poulain, P.-M., Tovar-Sanchez, A., Capet, A., Mason, E., Allen, J.T., Mahadevan, A., Tintoré, J., 2017. A Multiplatform Experiment to Unravel Meso- and Submesoscale Processes in an Intense Front (AlborEx). Front. Mar. Sci. 4:39. doi: 10.3389/fmars.2017.00039

Rudnick, D. L., 1996. Intensive surveys of the Azores Front: 2. Inferring the geostrophic and vertical velocity fields. J. Geophys. Res. Oceans 101, 16291–16303. doi: 10.1029/96JC01144

Rudnick, D.L., Zaba, K.D., Todd, R.E., Davis, R.E., 2017. A climatology of the California Current System from a network of underwater gliders. Progress in Oceanography, Volume 154, Pages 64-106. doi: https://doi.org/10.1016/j.pocean.2017.03.002

Ruiz, S., Pascual, A., Garau, B., Faugère, Y., Alvarez, A., Tintoré, J., 2009. Mesoscale dynamics of the Balearic Front, integrating glider, ship and satellite data, J. Mar. Syst., 78(suppl.), S3–S16, doi:10.1016/ j.jmarsys.2009.01.007.

Ruiz, S., Claret, M., Pascual, A., Olita, A., Troupin, C., Capet, A. et al., 2019. Effects of oceanic mesoscale and submesoscale frontal processes on the vertical transport of phytoplankton. Journal of Geophysical Research: Oceans, 124, 5999–6014. https://doi.org/10.1029/2019JC015034

Simoncelli, S., Fratianni, C., Pinardi, N., Grandi, A., Drudi, M., Oddo, P., Dobricic, S., 2014. Mediterranean Sea physical reanalysis (MEDREA 1987-2015) (version 1) [dataset]. Copernicus Monitoring Environment Marine Service (CMEMS). doi:10.25423/medsea_reanalysis_phys_006_004.

Sinha, A., Abernathey, R., 2021. Estimating Ocean Surface Currents With Machine Learning. Front. Mar. Sci. 8:672477. doi: 10.3389/fmars.2021.672477

Ubelmann, C., Dibarboure, G., Gaultier, L., Ponte, A., Ardhuin, F., Ballarotta, M., Faugère, Y., 2021. « Reconstructing Ocean Surface Current Combining Altimetry and Future Spaceborne Doppler Data ». Journal of Geophysical Research: Oceans 126 (3): e2020JC016560.

Wang, J., Fu, L., Qiu, B., Menemenlis, D., Farrar, J.T., Chao, Y., Thompson, A.F., & Flexas, M.M., 2018. An Observing System Simulation Experiment for the Calibration and Validation of the Surface Water Ocean Topography Sea Surface Height Measurement Using In Situ Platforms, Journal of Atmospheric and Oceanic Technology, 35(2), 281-297.

Wang, J., Fu, L.-L., Torres, H. S., Chen, S., Qiu, B., and Menemenlis, D., 2019. On the spatial scales to be resolved by the surface water and ocean topography Ka-Band radar interferometer. J. Atmos. Ocean. Technol. 36, 87–99. doi: 10.1175/JTECH-D-18-0119.1